11-30-2023

Microscale to Mesoscale Modeling of the Ocean Under Tropical Cyclones: Effects of Sea Spray and Surfactants on Tropical Cyclone Intensity and Air-Sea Gas Exchange

Breanna Lynn Cain Vanderplow
Nova Southeastern University

Dissertation of
Breanna Lynn Cain Vanderplow

Submitted in Partial Fulfillment of the Requirements for the Degree of

Doctor of Philosophy
Oceanography/Marine Biology

Nova Southeastern University
Halmos College of Arts and Sciences

November 2023

Approved:
Dissertation Committee

Committee Chair: Alexander Soloviev, Ph.D.

Committee Member: Brian Haus, Ph.D.

Committee Member: Isaac Ginis, Ph.D.

Committee Member: Richard Dodge, Ph.D.

NOVA SOUTHEASTERN UNIVERSITY

HALMOS COLLEGE OF ARTS AND SCIENCES

Microscale to Mesoscale Modeling of the Ocean Under Tropical Cyclones: Effects of Sea Spray and Surfactants on Tropical Cyclone Intensity and Air-Sea Gas Exchange

By

Breanna Lynn Cain Vanderplow

Submitted to the Faculty of
Halmos College of Arts and Sciences
in partial fulfillment of the requirements for
the degree of Doctor of Philosophy with a specialty in:

Oceanography and Marine Biology

Nova Southeastern University

January 2024

Abstract

Tropical cyclone intensity prediction remains a challenge despite computational and observational developments because successful intensity forecasting requires implementing a multitude of atmospheric and oceanic processes. Hurricane Maria 2017 and Hurricane Dorian 2019 serve as prime examples of rapidly intensifying storms that devastated communities in the Caribbean. A lack of understanding and parameterization of crucial physics involved in tropical cyclone intensity in existing forecast models may have led to these and other forecasting errors.

Microscale physical processes at the air-sea interface are a major factor in intensification of tropical cyclones that are often unaccounted for in forecasting models since they are difficult to study in the field and laboratory and are therefore not well understood. An ongoing uncertainty in tropical cyclone dynamics is the sea spray generation function (SSGF). While multiple estimates of the SSGF have been produced, a lack of experimental data in high wind conditions makes it difficult to establish a confident SSGF for tropical cyclones. Surface active agents impact spray generation, causing variation in spray diameter and an increase in generation that may influence heat, momentum, and gas exchanges during tropical cyclones. To better understand these processes, a computational fluid dynamics model was developed that simulates spray generation under all five tropical cyclone category conditions and resolves spray with radii starting from 100-μm. The numerical results were validated with Category 1 data from a laboratory experiment at the University of Miami. SSGFs calculated from the model revealed an increase in the spray generation under all categories of tropical cyclone conditions except Category 4 and Category 5 conditions, where little to no impact of surfactants on spray generation was found. This phenomenon might be explained by a change in regime under major tropical cyclones.

Additionally, small to mesoscale ocean circulation and characteristics, particularly in environments such as a western boundary current, lead to complex interaction between ocean circulation and tropical cyclones. Not only are ocean dynamics in the open ocean affected by tropical cyclones, but the impacts can extend to coasts outside of the predicted storm impact area, leading to unprepared coastal communities due to these poorly understood interactions. This can improve parameterizations of variables such as mixing and fluxes in tropical cyclone forecasting models. An additional computational fluid dynamics model has been developed that predicts and characterizes small to mesoscale ocean circulation and dynamics in a western boundary current.

This body of work aims to further understand ocean circulation in the surface layer in western boundary currents and complex microphysics at the air-sea interface during tropical cyclones including spray and spume generation, evaporation, and related fluxes, air-sea gas exchange, and the effects of factors such as surfactants. The multitude of ocean dynamics and air-sea interaction processes to be studied in this work converge to strive for a more complete understanding of the ocean water column and the air-sea interface under tropical cyclones that could ideally be implemented into tropical cyclone prediction models to improve intensity forecasting.

Keywords: sea spray, tropical cyclone, hurricane, air-sea interaction, spume, computational fluid dynamics, air-sea fluxes, rapid intensification, CFD, ANSYS Fluent, surfactants, surface-active materials, air-sea gas exchange, SSGF, sea spray generation function, numerical modeling, ocean circulation, western boundary currents, Gulf Stream, laboratory experiments, field observations

Dedication

I could not have survived graduate school and completing my dissertation without two people who supported me, always believed in me, pushed me towards my goals, and allowed me to find and grow into the person I am today. Unfortunately, this past year the world lost them both too soon.

Teveris: my best friend, my strength, my everything.

My dad: the strongest person I've ever known and who inspired my love of the ocean.

Table of Contents

Table of Figures

1. Introduction

1.1. Tropical Cyclone Intensification and Prediction

Predicting intensities of tropical cyclones, especially their rapid intensification, remains a daunting challenge despite advances in model forecasting through increased computer power and improved observational data systems. While cyclone track prediction over all time scales has generally improved by over 60% in the past 30 years (Fig. 1a), there has been less improvement in the accuracy of forecasting the intensification of tropical cyclones, particularly since the 1990's (Rappaport et al., 2009; DeMaria et al., 2014; Emanuel & Zhang, 2016; Masters, 2020). Forecasting intensity improvement has plateaued since 2013 for 24-48 hours (Fig. 1b). Intensity error forecasting increased dramatically in 2018 for 96- and 120-hour timescales, as shown in Figure 1b, likely due to the poor prediction of Hurricane Dorian's rapid intensification (Masters, 2020). While track error decreased since 2019 for both 24- and 48-hour timescales, intensity error increased (Fig. 1a, b). Intensity error from the best available model decreased by only 1-2% per year between 1989 and 2012 (DeMaria et al., 2014). Tropical cyclones Charley 2004, Wilma 2005, Humberto 2007, Maria, 2017, and Dorian, 2019 all intensified prior to landfall, devastating unprepared communities due to rapid intensification that was missed by tropical cyclone forecast models. Effective tropical cyclone forecasting is highly complex and must account for many processes in both the atmosphere and ocean (Gopalakrishnan et al., 2012). Recent model improvements include focusing on the inner core structural changes of the storm (Chen et al., 2011), implementing cloud-resolving models (Yau et al., 2004) and increasing model resolution to below 1 km (Davis et al., 2011). In addition to improvements to the atmospheric component, concepts of ocean heat content (Shay et al., 2000; Lin et al., 2013), barrier layer (Lukas and Lindstrom, 1991), and air-sea interface (Soloviev et al., 2017) have recently been introduced into the consideration of tropical cyclone physics. Intensity forecasting remains a challenge in part due to an incomplete understanding of key physics that contribute to intensification of tropical cyclones. This includes cloud microphysics. The distribution, concentration, and diameters of spray affect the aerosols that serve as cloud condensation nuclei (Law et al. 2017, Poschl & Shiraiwa 2015). It has been predicted that aerosols serving as cloud condensation nuclei intensify the tropical cyclone if they penetrate the central clouds of the storm but weaken it if they penetrate the clouds at the storm periphery (Shpund et al., 2019).

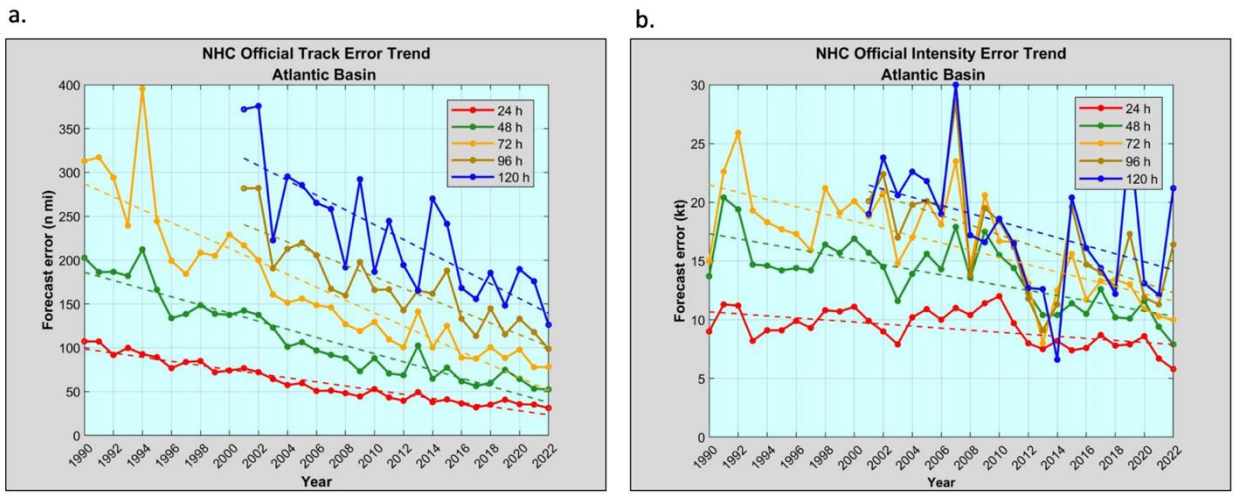

Figure 1. The National Hurricane Center's error in (a) track forecasting and (b) intensity forecasting up until 2022 (Cangialosi, 2023).

Storms that undergo rapid intensification, defined by NOAA as "an increase in the maximum sustained winds of a tropical cyclone of at least 34 mph in a 24-h period," can increase from a Category 1 storm (74-95 mph) to a Category 5 storm (>157 mph) in less than a day. Tropical cyclones that rapidly intensify not only have an 80% chance of becoming a major storm (above Category 3) but are also the least accurately forecasted (Bhatia et al., 2019). There are two periods of intensification: a slow intensification period and a subsequent rapid intensification period (Sitkowski and Barnes, 2009). Tropical cyclones need specific environmental conditions to develop and intensify, which include a sea surface temperature above 26.5^{o} C, high ocean heat content, high relative humidity, low vertical wind shear, deep convection, and an initial vortex of the right rotation ~5^{o} latitude from the equator (Merrill, 1988; Tory et al., 2006; Kaplan et al., 2010; Jiang & Ramirez, 2013; Fudeyasu et al., 2018). Presence of the salt-stratified barrier layer (Lukas & Lindstrom, 1991) is a novel, but critical, factor in tropical cyclone prediction (see, e.g., Grodsky et al., 2012; Kao & Lagerloef, 2020). Heating in the storm's core and the radius of maximum wind are other factors that contribute to intensification. Storms that have a large intensity shift within 12 hours or that have a disparity between their current intensity and maximum potential intensity (MPI) are also likely to intensify (Fudeyasu et al., 2018).

Internal processes including spiral rainband dynamics, asymmetric deep convection, eye/eyewall mixing, and eyewall replacement cycles of tropical cyclones have also proven important to rapid intensification (Hendricks et al., 2010; Hendricks, 2012). Inner-core processes

such as convection and precipitation are directly related to the release of latent heat, which fundamentally motivates tropical cyclone development through positive feedback between diabatic heating and moisture convergence from radial circulation (Jiang and Ramirez, 2013). There remains a debate on whether symmetric or asymmetric convection and circulation is more important to storm intensification (Ooyama, 1969; Smith, 1981; Shapiro & Willoughby, 1982; Smith & Montgomery, 2011). Jiang and Ramirez (2013) found that rapidly intensifying tropical cyclones do not always have more inner-core convection than storms which do not rapidly intensify. Their results did find that rapidly intensifying storms required a minimum threshold of the precipitation area, volume of precipitation, and convective intensity in the inner core, meaning the storm must be organized to intensify and/or rapidly intensify.

Researchers estimate the limits on tropical cyclone intensity through the approximation of MPI. Miller (1958) first estimated MPI using maximum air temperature in the eyewall caused by sinking air. Malkus and Riehl (1960) calculated parcel trajectories of available energy to counteract momentum loss. Emanuel (1986; 1995) estimated MPI using the storms energy cycle to approximate the maximum surface wind speed. More recently, Shay and Brewster (2010) and Lin et al. (2013) included ocean heat content to MPI estimations. Calculations of MPI combine dynamics and thermodynamics (Holland, 1997). These include momentum, or the amount of motion measured as a product of mass and velocity, hydrostatic balance, where the horizontal pressure gradient is at equilibrium with the Coriolis and centripetal accelerations (Marks, 2003), temperature, or heat intensity, and pressure, or the physical force exerted on an object. Enthalpy, the total heat content of a system, is also crucial to tropical cyclones and air-sea interaction processes. Latent (heat required to convert a liquid to vapor) and sensible (heat that changes temperature) heat fluxes contribute to enthalpy, along with pressure and volume.

MPI helps to estimate the upper limit of tropical cyclone intensity as follows:

$$V^2 = (k^* - k)\frac{(\bar{T} - T_0)}{T_0}\frac{C_k}{C_d} \quad (1)$$

where V is wind speed, C_k the enthalpy coefficient, C_d the drag coefficient, k^* the saturation enthalpy at the sea surface, k the enthalpy, $\bar{T}$ the pre-cyclone depth-averaged temperature, and T_0 the outflow temperature at the top of the tropical cyclone. MPI is proportional to the ratio C_k/C_d, which results in it controlling the maximum tropical cyclone intensity for other variables. Air-sea

exchanges play an important role in tropical cyclone intensity because it depends on momentum and enthalpy transfers at the air-sea interface (Emanuel, 1986; Ooyama, 1969). C_k may not strongly depend on wind speed for winds U_{10} > 10 m s^{-1} at 10 m height (Jeong et al., 2012). The laboratory result from Jeong et al. (2012) was limited to the maximum equivalent neutral stratification wind speed of $U_{10} = 40$ m s^{-1}, which was in part corroborated by aircraft-based flux measurements (Drennan et al., 2007) and extended by Richter and Stern (2014) and Bell et al. (2012) to $U_{10} = 70 - 75$ m s^{-1} using dropsonde data or by utilizing the conservation of azimuthally averaged absolute angular momentum, respectively. Drennan et al. (2007) took direct measurements of the latent heat flux under tropical cyclone conditions, finding that the humidity flux coefficient did not depend on wind speed up to 30 m s^{-1}. Zhang et al. (2008) observed sensible heat fluxes under tropical cyclones up to 30 m s^{-1} and determined that C_k was independent of wind speed. Haus et al. (2010) found that C_k decreases with wind speed under light winds, but once wave generation begins the decrease slowed until 29 m s^{-1}, where it essentially remained the same. Komori et al. (2018) also measured sensible C_h, and latent, C_e, heat exchange coefficients in the Kyoto wave tank, revealing that both C_h and C_e are almost equal to the enthalpy coefficient under high winds. They also found that C_h, C_e, and C_k are constant until ~35 m s^{-1} winds, when significant spray generation begins. Troitskaya et al. (2020) found that drag increased with wind speed and wave fetch, but the heat exchange coefficient remained constant with increasing wind speed.

The drag coefficient (C_d) is a determining factor in tropical cyclone intensity and is crucial to the estimation of MPI. It can be calculated by:

$$C_{10} = \frac{\tau}{\rho_a U_{10}^2} \qquad (2)$$

where U_{10} is the wind speed at 10 m height, τ is the wind stress, and ρ_a is the air density (Stewart, 2002). Recent studies show that C_d, which increases with wind speed until ~30 m s^{-1}, is a determining factor in tropical cyclone intensity (Bell et al., 2012; Jarosz et al., 2007; Kossin et al., 2013; Donelan et al., 2004; Donelan, 2018). NOAA and the Office of Naval Research conducted the Coupled Boundary Layer Air-Sea Transfer (CBLAST) experiment from 2000 to 2005 to study air-sea interaction under tropical cyclones to improve forecasting models. Data collection included in situ measurements from radar, dropsondes, and buoys in winds above 22 m s^{-1} (Black et al., 2007). From this data it was concluded that the C_d increased with wind speed

until 25 m s^{-1} (French et al., 2007) to 32 m s^{-1} (Jarosz et al., 2007) and then decreased. Lab experiments by Haus et al. (2010) at the University of Miami tank found that C_k/C_d from 2 to 18 m s^{-1} was much higher than field experiments caused by a lower C_d in the tank related to the small fetch of waves within a wave tank compared to in the field. Between 30 and 60 m s^{-1} C_d decreases, which is favorable for tropical storm intensification, because the KH instability at the air-sea interface leads to an absence of short surface waves (the instability grows more quickly due to large shear for short waves), and the two-phase near surface layer thickens. Around 60 m s^{-1}, where C_d stops decreasing is considered the aerodynamic drag well (Soloviev et al., 2017). Richter et al. (2021) analyzed dropsonde profiles in high winds, confirming the drag well around 60 m s^{-1}. The aerodynamic drag well (Fig. 2) also demonstrates why many storms do not progress to Category 5, because the slope (against wind speed) of C_d is positive above 60 m s^{-1}, which does not provide favorable conditions for further intensification since the sea surface momentum loss increases dramatically. Instead of intensifying, the aerodynamic drag well likely (depending on MPI) leads to a storm remaining at Category 3 intensity (at the bottom of the drag well), which explains bi-modal distribution of maximum intensity found by Kossin et al. (2013), as shown in Figure 2.

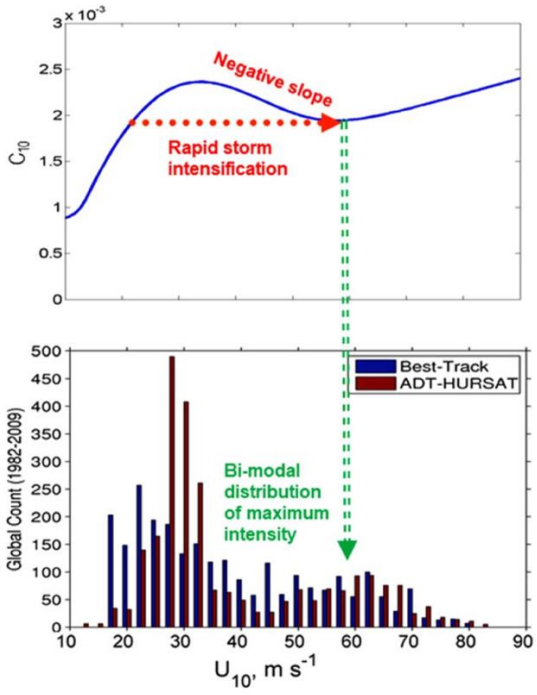

Figure 2. (top) The drag coefficient displaying the aerodynamic drag well at ~60 m s^{-1}. (bottom) Bimodal distribution of lifetime maximum intensity for tropical cyclones (Kossin et al., 2013). Figure from Soloviev et al. (2017).

Above 60 m s^{-1}, the increase of C_d could be caused by the entrainment of large amounts of sea spray (Andreas & Emanuel, 2001), which was implemented into the concept of rapid intensification and the aerodynamic drag well (Soloviev et al., 2017). It is uncertain how C_d behaves above 120 m s^{-1} wind speeds. Soloviev et al. (2014) found that it increased, while Takagaki et al. (2012) found that it approached a constant value. If sea spray is a significant factor in the increase of C_d above 60 m s^{-1}, the continued increase of spray generation as winds intensify above 120 m s^{-1} may also lead to further increase of C_d. Takagaki et al. (2012) acknowledged that there are differences between field and laboratory measurements of spray (which may or may not influence drag at high wind speeds) and a better understanding of spray is necessary. Tropical cyclone intensity forecasting is sensitive to these surface fluxes, namely because key quantities such as the maximum azimuthal wind speed and radius of maximum winds are directly related to the C_k/C_d ratio (Emanuel, 1986; 1995). Further understanding, based on measurements and observations, of enthalpy and momentum flux physics will therefore aid in improved tropical cyclone intensity forecasting.

1.3. Microscale Processes at the Air-Sea Interface Under Tropical Cyclones

Microscale processes at the air-sea interface are among the processes that still need to be more adequately parameterized in existing models. Sea spray is one of the key microscale processes that researchers struggle to be parameterize due to its complex physics and lack of measurements under strong winds. Riehl (1954) was the first to report that spray evaporation under high winds offers part of the heat required for intensification of tropical cyclones. Fairall et al. (1994) was the first to implement spray-based parameterization to a model of the tropical cyclone boundary layer and found that evaporation may be important to maintaining this boundary layer. The spray parameterization used by Fairall et al. (1994) was that spray sensible heat flux contributed 6% of the direct sensible heat flux, while the spray latent heat flux contributed 60% of the direct latent heat flux. The negative sensible heat flux caused by spray taking energy to evaporate from the boundary layer was found to be much larger than the spray sensible heat flux. Using a continuation of Fairall's work, Kepert et al. (1999) found that spray evaporation influenced the tropical cyclone boundary layer stratification and therefore could affect intensity of the storm. Lighthill et al. (1994) found the opposite, that spray reduced intensity of tropical cyclones because of evaporative cooling. Wang et al. (1999) and Uang et al.

(1999) found that spray had little to no effect tropical cyclone intensity, but they did not account for 're-entrant' spray in their models. Bao et al. (2000), using the parameterization of Fairall et al. (1994), found that if spray evaporates, it has little to no influence on tropical cyclone intensity, but if spray re-enters the ocean, intensity is affected. Andreas and Emanuel (2001) also found that spray is important to enthalpy and momentum fluxes between the ocean and atmosphere under high winds, and that 're-entrant' spray contributes most to the enthalpy flux. They also concluded that including wave drag and spray enthalpy and momentum exchange resulted in a cancellation of one another, explaining why models that are too simple to account for complex microphysics at the air-sea interface do not accurately predict intensity.

Perrie et al. (2005) included spray in the Canadian mesoscale model and found that it increased storm intensity, as well as cooled near the sea surface and warmed upper parts of the boundary layer. In contract to this, Barnes (2006) and Gall et al. (2008) found that spray may warm near the sea surface of the boundary layer. Gall et al. (2008) also found that spray sensible and latent heat fluxes are enhanced as spray generation increases, which increased intensity of the storm, but spray drag slightly weakened the storm. Shpund et al. (2012) deemed the lowest 400-m of the atmosphere, which directly interacts with spray, the hurricane atmospheric mixed layer. The microphysical structure of this layer is directly impacted by the upward transport of spray by large eddies. The results from Shpund et al. (2012) also found that spray's effect depends on the initial humidity and temperature: if the humidity is low, spray evaporation cools the hurricane atmospheric mixed layer, while if the humidity is low, spray evaporation has less impact.

An effort to include bulk parameterization of the air-sea momentum flux, which was found to be of key importance to sea surface wind speeds, enhanced the parameterization of the wind-pressure relationship of major tropical cyclones in predictions models (Moon et al., 2007). Richter and Stern (2014) proposed that spray is the dominant enthalpy flux at the air-sea interface during tropical cyclones. Bao et al. (2017) found, by implementing air-sea sensible and latent heat fluxes into their model, that spray decreases the drag coefficient, and therefore accelerates the flow near the sea surface in the boundary layer. This in turn led to increased tropical cyclone intensity in stronger storms, but variable intensity in weaker storms. Lee et al. (2019) more carefully considered the wind dependent drag coefficient in their model, which led to an improvement in prediction of rapid intensification within 24 hours by 16%.

Despite advances, uncertainty remains due to various challenges in modeling microscale processes involved in tropical cyclone dynamics. One major issue is a lack of observations and measurements under tropical cyclone conditions (Fairall et al., 2014). Most parameterizations of air-sea fluxes have focused on winds below 25 m s^{-1} because observations of spray above 20 m s^{-1} are lacking (Gall et al., 2008; Zhang et al., 2008; Fairall et al., 2014). This makes extrapolating these parameterizations to high wind conditions difficult. One key factor that exists at winds above 25 m s^{-1} is the abundance of sea spray. Zhang et al. (2008) and Fairall et al. 2014 suggested that at high wind speeds, spray becomes abundant, which complicates enthalpy transport and may change heat and momentum coefficients.

Accurate parameterization of the thermodynamic influence of spray is still a challenge (Fairall et al., 1990; 1994; Kepert et al., 1999; Bianco et al., 2011; Richter & Sullivan, 2014). Fairall et al. (2014) explained that the sea spray effect is parameterized using the size dependent source function (the number of droplets of a certain size produced at the sea surface, per unit surface area, per unit time, as a function of surface forcing). The issue with this is that the source function cannot be measured directly and is therefore estimated. Spray sizes used in models also requires better parameterization. Implementing the entire range of spray sizes in models also remains a challenge. Many studies have focused on spray diameters between 0.5 and 10 mm (Sphund et al., 2012), but spray droplets often have radii below 0.5 mm, and even as small as 1 μm (Andreas, 1992; Veron et al., 2012). Measurements in the ocean also have lacked those on large spray droplets (r>20 μm), which are likely the most important to air-sea enthalpy and momentum fluxes. Gall et al. (2008) argued that a better understanding of the spray generation function is needed to fully understand how much spray is generated in the boundary layer. Shpund et al. (2012) recognized that their work still needed to account for wind speed changes, as this increases spray generation and the amount of spray transported to upper layers of the atmosphere.

Another limitation of previous models is that they are often one dimensional, because most microscale processes occur in only tens of meters above the air-sea interface (Shpund et al., 2012). One-dimensional models may oversimplify the complexity of air-sea interaction processes. Bao et al. (2017) specified that including wave-induced drag effects on spray drag could be important to modeling efforts. Overlooking key physics in models often leads to inaccurate hurricane intensity predictions, further leading to erroneous warnings and evacuations

that may cost lives. Therefore, it is essential to implement more accurate fluxes at the air-sea interface and their effect on tropical cyclone intensity into future prediction models to increase forecasting accuracy.

1.3. A Two-Phase Environment at the Air-sea Interface Under Tropical Cyclones

Within tropical cyclones, the atmosphere and ocean are strongly coupled. The air-sea interface controls and is controlled by momentum, heat, mass, and energy exchanges between the ocean and atmosphere. Tropical cyclones gain heat and moisture from, as well as transfer momentum and kinetic energy to the ocean, through the air-sea interface. In the high wind conditions of tropical cyclones, a two-phase environment is created near the sea surface. In this environment, spray droplets are generated by white caps on breaking waves and in waves that have not broken, in a process that resembles the Kelvin-Helmholtz (KH) instability (Koga, 1981; Soloviev & Lukas, 2010; Soloviev et al., 2017).

Most spray is formed at wave crests, either with or without a whitecap, but spray drops are also formed elsewhere in this environment. The two-phase environment produces a white sheet, or 'white out', which consists of air-bubbles in the water, spray droplets in the air, and foam on the sea surface (Soloviev et al., 2017). Spray and bubbles increase the effective surface area at the air-sea interface, which affects heat and momentum fluxes. According to Holthuijsen et al. (2012), in tropical cyclones wave-breaking whitecaps, which are a mixture of bubbles and spray, only cover ~4%, while the 'white out' associated with foam and spray streaks covers ~96% of the sea surface. Whitecapping with spray and bubble formation occurs once wind speeds exceed 7-9 m s^{-1}, but the formation of a continuous two-phase environment is only observed when wind speeds are above ~30 m s^{-1}. The replacement of whitecaps with 'white out' on the sea surface alters momentum exchange between the ocean and atmosphere. The development of the two-phase environment also produces additional drag near the sea surface. It previously was thought that C_d monotonically increases with wind speed, but since has been found to peak at wind speeds of ~35 m s^{-1} and decline until ~60 m s^{-1} (Soloviev et al., 2014; 2017). This behavior of the drag coefficient corresponds to the change from whitecap to 'white out' conditions under high wind speeds, as shown in Figure 3 (Holthuijsen et al., 2012).

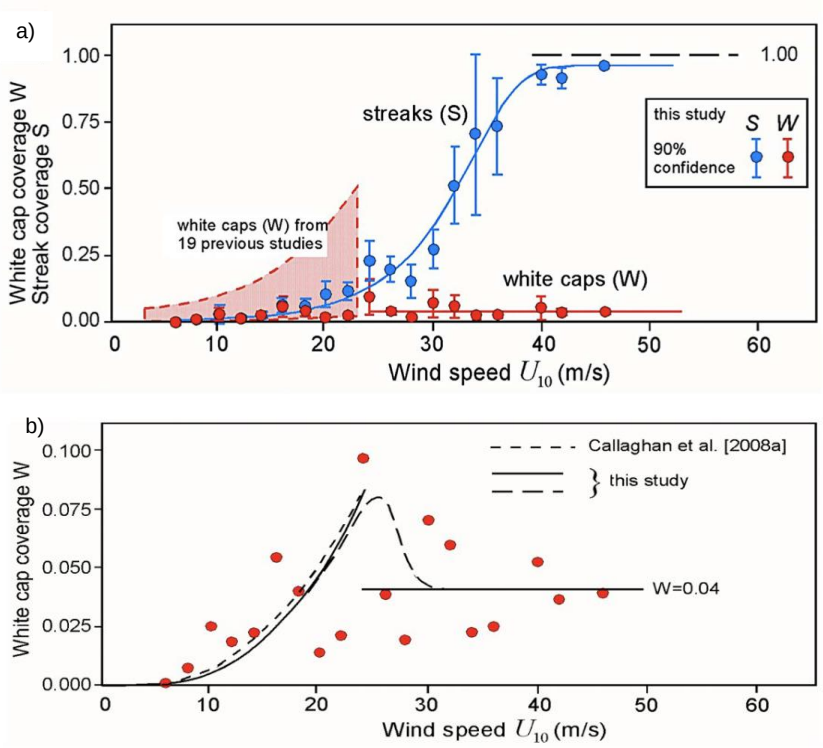

Figure 3. Experiment by Holthuijsen et al. (2012). (a) Whitecap coverage observed to increase to a maximum at about U_{10}=24 m s^{-1}, then decrease and remain limited. Meanwhile, streaks ('white out') are shown to increase to almost 100% coverage. (b) Another schematic showing the whitecap coverage increasing to a maximum at U_{10}=24 m s^{-1}. The whitecapping then decreases to a limited value.

1.4. Sea Spray and Spume Generation

Under light winds, the KH instability of the air-water interface contributes to surface wave generation in the gravity-capillary range (Fig. 4a) (Miles, 1959). Under wind speeds above 4-5 m s^{-1} short wavelets steepen and break internally, causing 'microscale wave breaking', which does not disrupt the air-sea interface enough to eject spray (Siddiqui and Loewen, 2007; Banner and Phillips, 1974; Jessup et al., 1997; Siddiqui et al., 2001). Under tropical cyclone force winds, the gravity and surface tension forces are overcome by pressure fluctuations due to KH instability in the air flow, which disrupt the air-sea interface leading to sheets, fingers, and intense sea spray generation (Fig. 4b) (Soloviev & Lukas, 2010; Hoepffner et al., 2011).

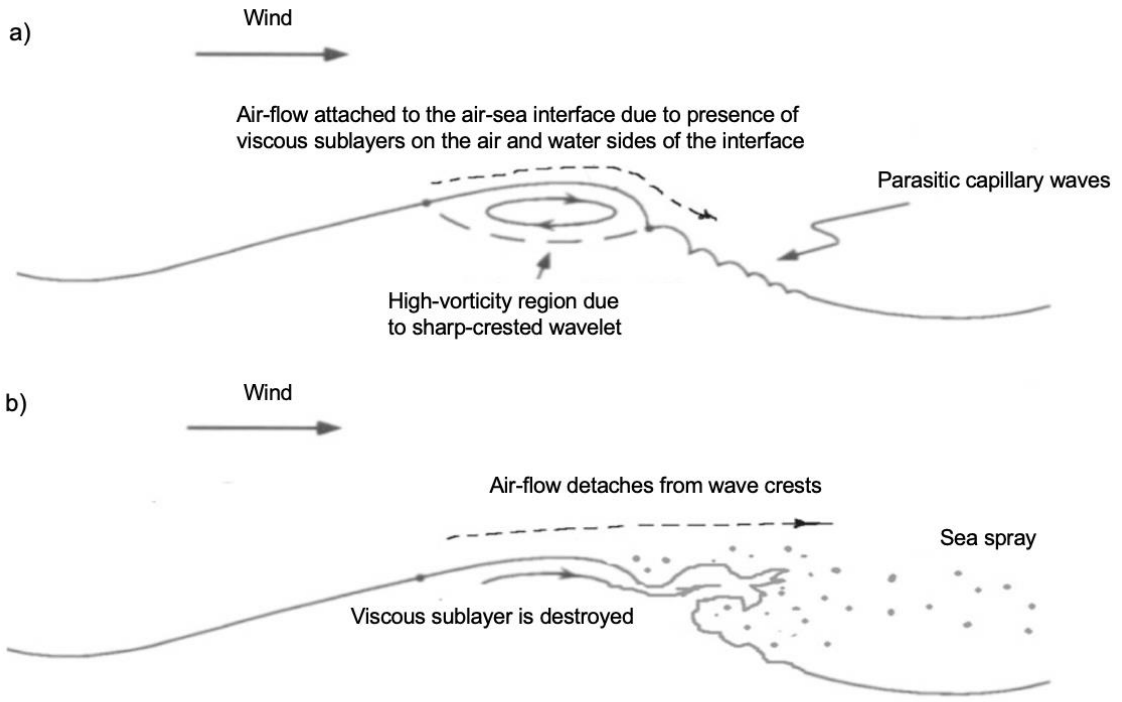

Figure 4. (a) Under moderate winds – wave surface with capillary waves. (b) Under high winds – waves break, which disrupts the air-sea interface and produces spray (Soloviev and Lukas, 2010).

In laboratory experiments, radii of sea spray have been observed in the range of less than 1 μm to up to 6 mm (Andreas, 1992; Veron et al., 2012). Small sea spray particles, which are typically sub-micrometer to tens of micrometers in diameter, are mostly generated by bursting air-bubbles (Spiel, 1997; 1998), which produce film and jet spray droplets. Film droplets typically range from 0.5 to 5 μm. Jet spray droplets are produced by the water jet breakup formed by the bubble (Blanchard, 1963; Wu, 1981) and range from 3 to 20 μm in diameter (Gall et al., 2008).

Another mechanism of spray generation is 'bag-breakup' fragmentation (Troitskaya et al., 2017) in which bag like pieces of water inflate and then quickly burst into spray droplets. Larger spray droplets, above 20 μm (spume), are produced by breaking waves (Gall et al., 2008). Under moderate winds (~7-11 m s^{-1}), 'tearing of water' from wave crests (Monahan et al. 1983) form spume droplets. When waves curl over and break, another type of spume droplet is formed -- splash droplets (Kepert et al., 1999). Koga (1981) and Veron et al. (2012) found that near the wave crest, where the wind stress is usually the highest, small, convoluted projections of

the water surface develop and break up to form spume droplets. The projections resume the KH instability at an interface with a very large density difference, which is characterized by strong asymmetry (Hoepffner et al., 2011). Much of the disturbance to the air-sea interface occurs on the air side; in fact, the KH instability generates spray and spume in the air but very few bubbles are produced in the water. At the same time, air-bubbles are mainly associated with whitecaps produced by longer breaking waves interacting with shorter, steeper gravity waves driven by local wind fluctuations (Thorpe, 1986).

Spray droplets are either entrained in the turbulent air flow or return to the sea surface (Andreas, 1992; Soloviev et al., 2014). Small spray droplets are typically suspended in the turbulent air flow, and eventually evaporate (Fig. 5). Spray must first cool from the sea surface temperature to its evaporation temperature, which usually occurs in less than one second because cooling only requires evaporation of less than 1% of the droplet's mass (Kepert, 1996; Andreas & Emanuel, 2001). The temperature each droplet reaches depends on size, salinity, temperature, humidity, and residence time in the air (Andreas & Emanuel 2001). The droplet must then evaporate, which takes over two orders of magnitude longer to accomplish (Kepert, 1996). Evaporation of spray, while it does not influence the ocean, does influence the atmosphere by changing air temperature and adding vapor to the air (Andreas & Emanuel, 2001). Understanding how spray affects the enthalpy flux between the ocean and atmosphere is critical because surface enthalpy flux provides most of the energy to tropical cyclones. The total enthalpy flux is calculated as:

$$H_{s,tot} + H_{l,tot} = H_l + H_s + Q_s + Q_l \quad (3)$$

where $H_{s,tot}$ is the total sensible heat flux, $H_{l,tot}$ is the total latent heat flux, H_l is the surface latent heat flux, H_s is the bulk surface sensible heat flux, Q_s is the droplet sensible heat flux, and Q_l is the spray-air latent heat flux (Gall et al., 2008).

Evaporating spray uses sensible heat from the boundary layer air. This lost heat is balanced by latent heat, which is added back to the boundary layer air through water vapor from the evaporated particles (Gall et al., 2008). Therefore, these small droplets may not contribute much to the enthalpy flux into a tropical cyclone due to the spray negative feedback phenomenon, which limits the total spray influence on total heat flux from water to air (Peng &

Richter, 2019). Sub-micrometer and micrometer aerosols produced by evaporating spray serve as cloud condensation nuclei and intensify the tropical cyclone if they penetrate the central clouds of the storm but weaken it if they penetrate the clouds at the storm periphery (Shpund et al., 2019; Soloviev et al., 2020). Spume droplets, which are ‘re-entrant’ spray, return to the sea surface before they can take enough sensible heat from the atmosphere to evaporate. Therefore, spume makes up a large part of the net spray-mediated enthalpy flux and significantly contribute to the enthalpy flux to the atmosphere under tropical cyclone winds (Andreas,1992; Kepert et al., 1999). Since tropical cyclones respond to net enthalpy fluxes, rather than the individual sensible and latent heat fluxes, it is likely that ‘re-entrant’ spray contributes to changes in tropical cyclone intensity (Andreas & Emanuel, 2001).

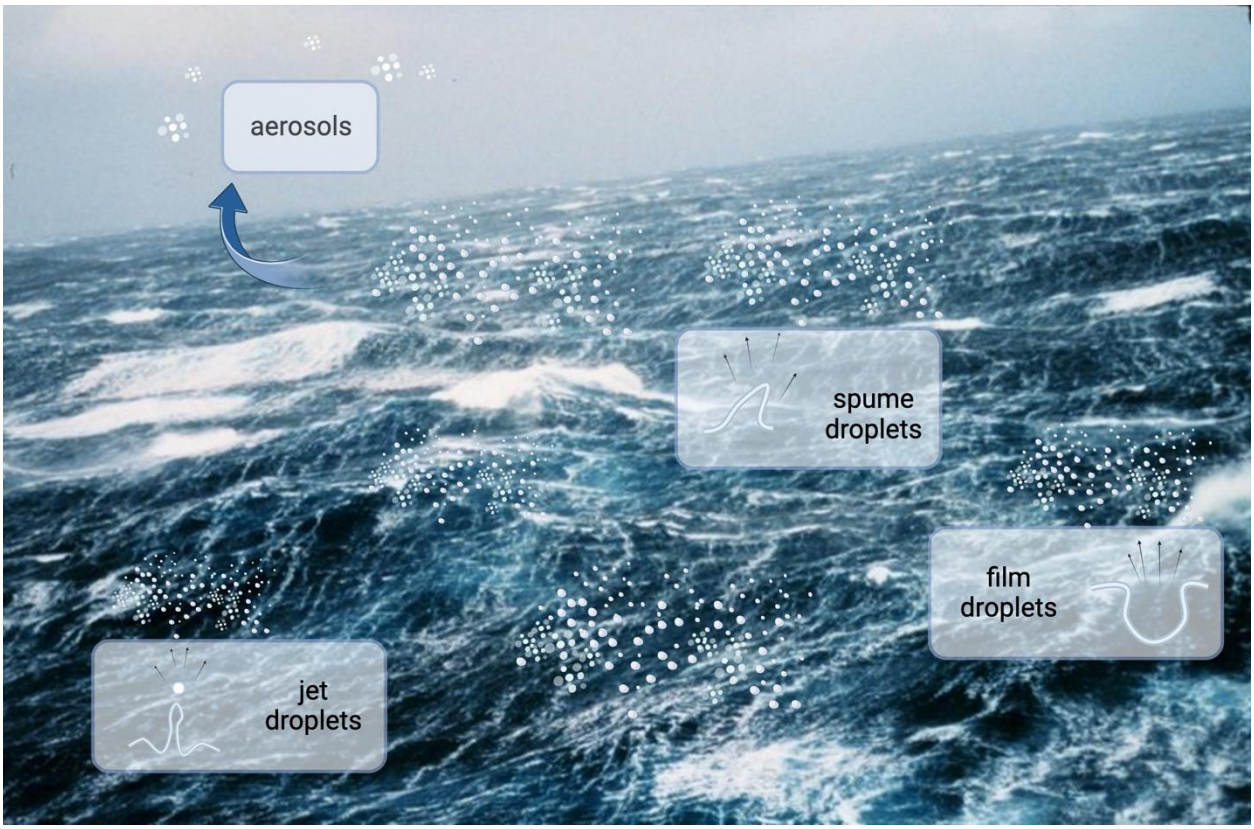

Figure 5. (a) The ocean under extreme winds (NOAA) showing spray generation including jet and film droplets (bubble-mediated) and spume droplets, some of which evaporate into aerosols. Made with BioRender.

Spray also influences drag at the air-sea interface. Momentum is taken from the atmosphere when spray is entrained in the airflow. ‘Re-entrant’ spray then gives this momentum

to the ocean when it returns to the sea surface. The influence of this drag has been debated. Wu (1973) found that is insignificant, while Fairall et al. (1994) found it is only important above winds of 50 m s^{-1}. Pielke and Lee (1994) found that the drag induced by spray reduces wind speed by 15% and therefore increases surface stress. Kudryavtsev (2006) found that spume inhibited turbulent mixing, leading to a decreased C_d above 20 m s^{-1} winds and up to 80 m s^{-1}. Bianco et al. (2011) found that spume under high winds stabilized the sea spray layer, decreasing drag and increasing both sensible and latent heat fluxes. Implementing their sea spray parameterization into the Weather Research and Forecasting (WRF) model increased tropical cyclone intensity forecasting considerably. Garg et al. (2018) also used WRF to test spray mediated flux formulations, finding that intensity was enhanced when spray and surface waves were considered. Wada et al. (2018) tested various parameterizations of sea spray, determining that the differences between existing parameterizations lead to considerably different results in tropical cyclone forecasting models.

Under tropical cyclone conditions, the modification of sensible and latent heat fluxes and momentum fluxes due to large amounts of spray leads to changes in tropical cyclone structure and intensity (Fairall et al., 1994; 2014; Edson & Fairall, 1994; Andreas & Emanuel, 2001; Gall et al., 2008; Andreas et al., 2017). Kepert et al. (1999) and Peng and Richter (2019) noted the following fundamental issues that relate to spray effects: the sea spray generation function, the feedback by which spray droplets modify the environmental conditions, and parameterization of the thermodynamic effects of sea spray for tropical cyclone models. These problems remain due to the complexity of the air-sea interaction process during tropical cyclones and difficulties in direct observations during extreme conditions. Only a few experimental or observational studies attempted to measure the heat fluxes in tropical cyclone conditions (e.g., Drennan et al., 2007; Zhang et al., 2008). Tropical cyclone analysis is generally based on indirect measurements (Bell et al., 2012; Richter & Stern, 2014) or laboratory experiments (Jeong et al., 2012; Komori et al., 2018). Barr et al. (2023) developed a model specifically focused on heat fluxes of spray under tropical cyclone conditions. Within their model, visualized in Figure 6, which is based on the spray model of Fairall et al. (2009), they predict the total sensible ($H_{S,1}$) and latent heat fluxes ($H_{L,1}$). $H_{S,drop}$, $H_{wb,drop}$, and $H_{R,drop}$ are the droplet-specific sensible heat flux, heat flux due to temperature change from air temperature to salt-adjusted wet-bulb temperature, and heat flux due to size change, respectively. The model integrates these fluxes over the sea spray generation

function to obtain $H_{S,spr}$, $H_{wb,spr}$, and $H_{R,spr}$. $H_{S,0}$ and $H_{L,0}$ are the sensible heat fluxes and latent heat fluxes at the surface including sea spray.

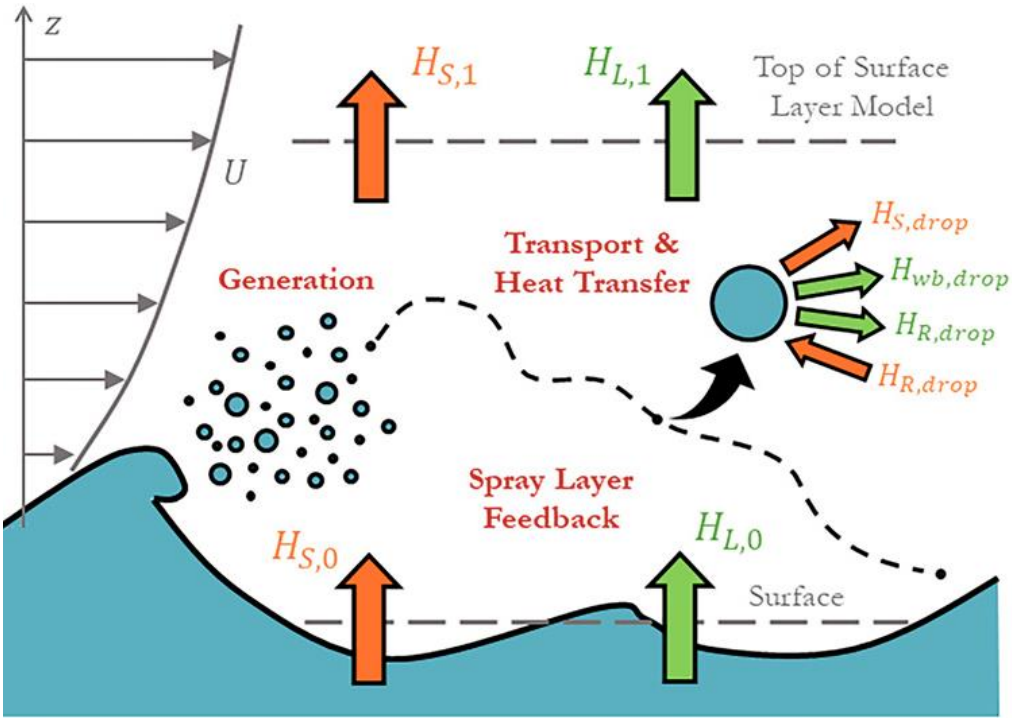

Figure 6. Fluxes and physical processes in the Barr et al. 2023 air–sea heat flux parameterization.

Their model found that spray increase the air-sea enthalpy flux by ~5-20% above 40-50 m s^{-1} winds near the radius of maximum wind. They also found that wave shoaling near the coast increases these effects dramatically, which is important for the later discussion of surfactant effects on sea spray as well.

The sea spray generation function (SSGF), *dF/dr*, is the number of drops produced per unit area, per unit time, per unit drop radius (shown here as volume flux):

$$\frac{4\pi r_0^3}{3}\frac{dF}{dr_0} \qquad (4)$$

Fairall et al. (1994) and Mueller and Veron (2009) proposed SSGFs that incorporated the impact of spray on air-sea fluxes. Mueller and Veron (2014) determined that less than 10% of the momentum flux up to wind speeds of 50 m s^{-1} was facilitated by spray, while on the other hand Andreas (2004) found that spray was involved in almost all the momentum flux at wind speeds of 60 m s^{-1}. Mueller and Veron (2014) considered a feedback mechanism in which spray

modified ambient conditions. At high wind speeds, they found less impact of spray on the sensible and latent heat fluxes using the Fairall et al. (1994) SSGF, but an increased impact using the SSGF of Mueller and Veron (2009). When estimating C_d in their study, Mueller and Veron (2014) found that drag increased dramatically with wind speed until ~30 m s^{-1}, where it increased more slowly thereafter. Andreas (2002) and Veron (2015) proposed SSGFs including spume under high wind speeds, and Troitskaya et al. (2017; 2018a, b) proposed that spume played a significant role in both the SSGF and spray mediated enthalpy and momentum fluxes under tropical cyclone conditions. Sroka and Emanuel (2021) reviewed the large variety in previous SSGF estimations and compared them in Figure 7. Recently, Ma et al. (2020) collected field measurements of the sea spray volume flux during Tropical Cyclone Olwyn using laser altimeters up to wind speeds of 22.7 m s^{-1}. The field measurements from Ma et al. (2020) were two to three orders of magnitude larger than spray volume fluxes from previous studies (Iida et al., 1992; Fairall et al., 1994; Andreas, 1998; Zhao et al., 2006; Toffoli et al., 2011; Troitskaya et al., 2018a).

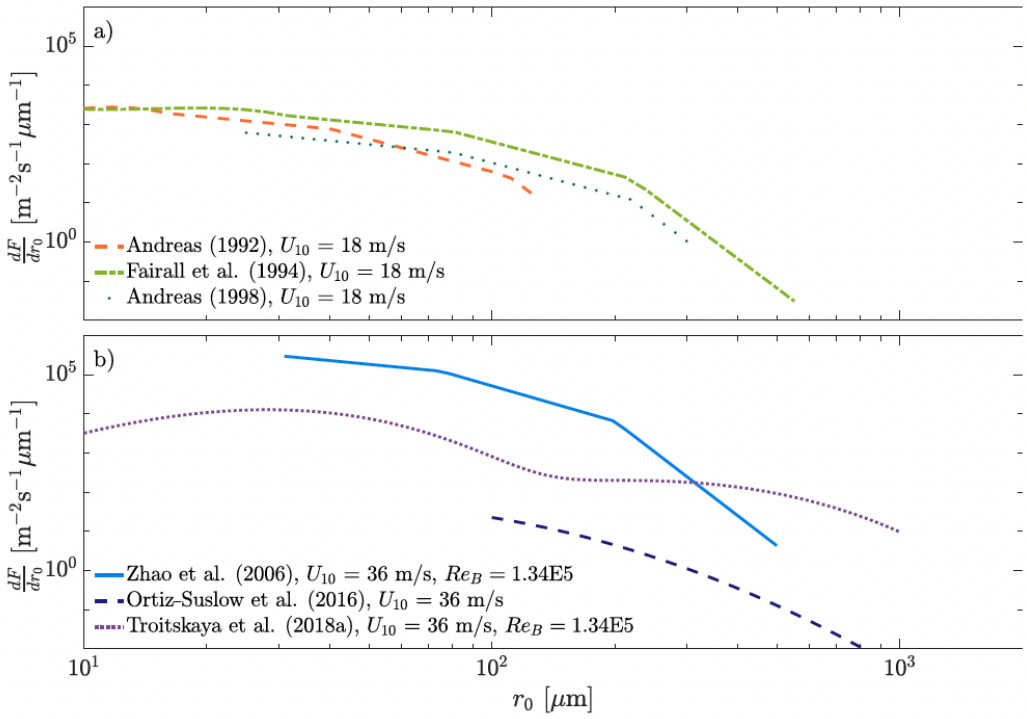

Figure 7. Sea spray generation functions as a function of initial drop radius r0 (Sroka and Emanuel, 2021).

The large differences between existing SSGFs indicates the complexity of this problem. Further work is needed to completely understand and parameterize the many factors involved in sea spray generation and its impact on air-sea interactions to develop an accurate SSGF.

1.5. Surface active agents

One factor that affects the air-sea interface are surface-active materials (surfactants) (Fig. 8). Surfactants are hydrophobic, meaning they repel water, and therefore accumulate in the sea surface microlayer (SML) if they are less dense than seawater. The SML consists of the top 1000 μm of the ocean and is defined by many molecular sublayers that have large gradients between or within them. This microlayer is greatly affected by physical, chemical, and biological properties (Wurl et al., 2011; Kurata et al., 2016). Surfactants are often produced by marine organisms such as phytoplankton, zooplankton, zooxanthellae, and bacteria. These compounds consist of substances such as lipids, proteins, saccharides, and organic acids (Alpers & Espedal, 2004). Carbohydrates, polysaccharides, and complex β-glucans are common surfactants found during phytoplankton blooms (Wurl et al., 2011). Surfactants may also appear on the sea surface during oil spills and using dispersants.

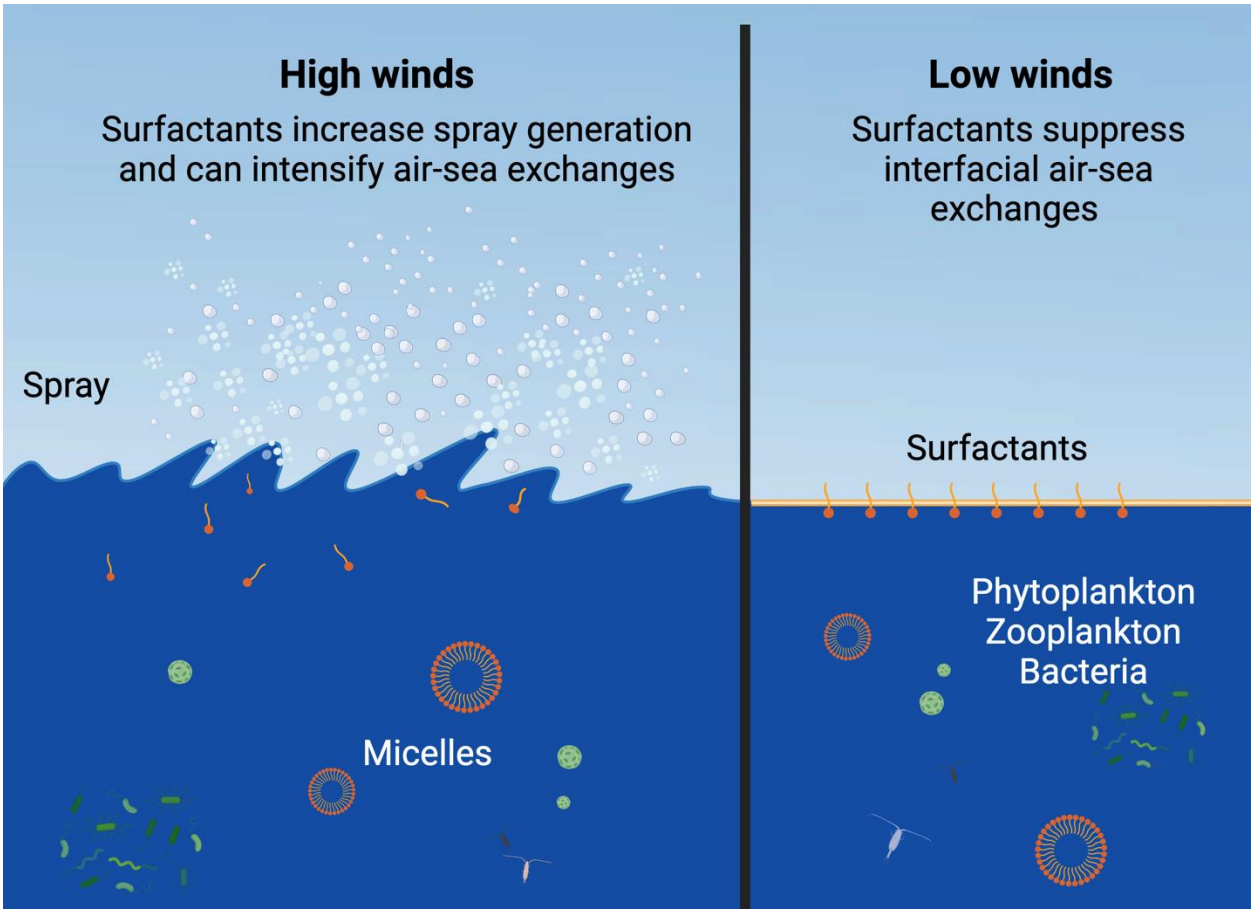

Figure 8. Illustration of surfactants under low (left) and high (right) winds at the air-sea interface (created using www.biorender.com).

Surfactants also modify the air-sea interface and the near-surface layer of the ocean, as they alter surface tension. Due to their effect on surface tension, surfactants dampen short gravity-capillary waves and air-sea gas exchange, suppress near-surface turbulence, and produce coherent structures (Wurl et al., 2011). Soloviev et al. (2011) found that C_d from the water side of the air-sea interface was reduced by 36% because of surfactants, meaning that momentum and other fluxes that depends on C_d between the air and water are reduced by surfactants. Troitskaya et al. (2019) looked at both natural foam generated by wave breaking and foam created by surfactants. They found that foam lowered surface steepness and decreased the drag coefficient. Under low winds, little foam typically exists on the sea surface, meanwhile under high winds when large amounts of foam may be present, the drag is likely be reduced.

Surfactants often produce slicks, or films, on the sea surface under low wind speed conditions (Kurata et al., 2016). Slicks are frequently formed from one molecular layer (~3

nanometer thickness), which allows for a small quantity of surfactant material to form a slick that covers a large area of the sea surface (Alpers & Espedal, 2004). These slicks may have a significant effect on the air-sea gas exchange rates of many gases, including greenhouse gases such as carbon dioxide, methane, and nitrous oxide (Wurl et al., 2011). The coverage, concentration, and composition of sea surface slicks caused by surfactants vary depending on wind, sea conditions, and with time. Under wind speeds above 7 to 10 m s^{-1}, breaking waves disrupt slick formation and overwhelm the effect of surfactants (Soloviev & Lukas, 2014). The effect of surfactants once again becomes important under tropical cyclone conditions due to their effects on sea spray. Notably, the size distribution of sea spray depends on the presence of surfactants, with spray generation increasing be 20-34% when surfactants are on the sea surface (Vanderplow, 2020). During high wind speed conditions surfactants are brought to the surface by turbulence and air-bubbles with increased mixing in the water column, enhanced by upwelling under the tropical cyclone (Price, 1981; Alpers & Espedal, 2004; Walker et al., 2005). Once brought to the surface, bubbles that burst release some surfactant material into the air as aerosols, and the remaining may form slicks on the sea surface. Foams are often produced by bubble bursting and the reforming of slicks afterwards, which can occur within seconds (Wurl et al., 2011). While studies on the impact of surfactants on tropical cyclone intensity are limited, Emanuel (1995) suggested that they may be critical to air-sea fluxes and ultimately tropical cyclone intensity. Emanuel (1995) proposed that surfactants may reduce hurricane intensity due to their effect on enthalpy and drag, which is based on observations at low wind speeds. Vanderplow et al. (2020) considered a different effect of surfactants in tropical cyclones, which is related to the change of spray size distribution and modification of enthalpy and momentum fluxes at the air-sea interface.

Surfactant presence also affects formation of cloud condensation nuclei (CCN) from sea spray aerosols (Fig. 9). The higher amount of surfactant present at the sea surface will impact spray generation through altered size distribution and concentration, which will affect the aerosols serving as CCNs. A higher surfactant concentration likely increases CCNs and therefore increases cloud formation (Elliott et al., 2014).

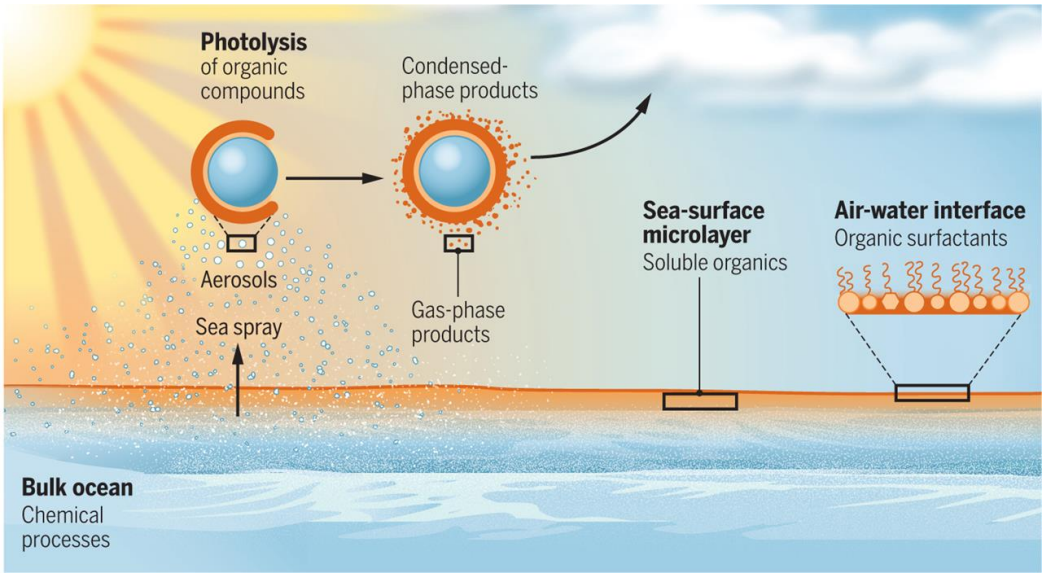

Figure 9. Surfactant accumulation in the sea surface microlayer and processes influenced by surfactants including spray, aerosols, and CCNs (Vaida 2016).

1.6. Freshwater vs. saltwater spray and aerosols

Between fresh and salt water, spray generation will differ due to the characteristics of the water itself. The most obvious difference is the salinity, where freshwater will have very low to no salinity, and seawater has a salinity of roughly 35 parts per thousand (ppt). The chemical components of salinity in seawater have the most influence on aerosol generation, as the solutes that remain after evaporation of spray droplets will be characterized by the chemical composition of the source water. Salinity also impacts other characteristics of the water including the density, heat capacity, thermal conductivity, viscosity, and surface tension. Heat capacity, density, viscosity, and surface tension are all higher in saltwater, while thermal conductivity is lower in saltwater (Qasem et al., 2021).

Bubbles, which are a source of spray through film and jet droplet formation, are also impacted by salinity differences. Saltwater subsurface bubble plumes have been shown to be characterized by smaller and a higher concentration of bubbles than freshwater ones, leading to higher whitecap coverage in seawater (Monahan & Zietlow, 1969; Monahan, 1969; Scott, 1975; Cartmill & Su, 1993; Haines & Johnson, 1995). More surface foam and related surface bubbles have also been observed with increasing salinity, which indicates that more droplets would be generated in saltier conditions as opposed to freshwater conditions (Jeong et al., 2012; Harb &

Foroutan, 2019). Slauenwhite and Johnson (1999) found that bubble break up is also impacted by salinity, causing a shift to larger diameters in freshwater, resulting in a change in the size distribution between freshwater and saltwater spray droplets, and therefore also aerosol particles, which will be discussed in more detail later. Viscosity also impacts bubble-mediated spray generation. The bubbles, particularly smaller ones, rise more slowly in more viscous waters (saltwater), decreasing the amount of spray, and again in turn aerosol particles (Ovadnevaite et al., 2014). Of course, viscosity is not only dependent on salinity, but also temperature and this also plays a significant role. Therefore, the overall bubble-mediated droplet distribution and concentration differs between freshwater and saltwater.

Spume generation is also impacted by salinity differences between freshwater and saltwater. Fairall et al. (2009) compared spume generation in freshwater and saltwater and found that there was little to no difference in spume volume. On the other hand, Mehta et al. (2019) found that spume generation was much higher in seawater than freshwater, and that the vertical distribution of saline spume was concentrated closer to the water surface. Spume droplets contribute significantly to air-sea momentum and enthalpy fluxes, as they have long enough residence times to interact with the airflow before also returning to the water surface to consequently cool the water. This phenomenon is particularly important at high winds, where the concentration of spume droplets increases dramatically (Mehta et al., 2019). Surface tension, which is higher in saltwater, will impact the generation of spume as well. In freshwater, lower surface tension will result in changes in the structure of spume generation mechanisms, leading to an increase in droplets and likely a shift to smaller diameters.

We can discuss how these differences between freshwater and saltwater will affect spray droplet processes such as momentum transfer and heat transfer both qualitatively and quantitatively. The net momentum of a droplet can be calculated as follows (Veron, 2015):

$$\Delta \mathbf{p}_{sp}(r) = \left(\frac{4}{3}\pi\right)\left[\left(r^3\rho_p \boldsymbol{v}\right)_{t=t_f} - \left(r^3\rho_p \boldsymbol{v}\right)_{t=0}\right] \quad (5)$$

where

t_f = total flight time of the droplet

The droplet density depends on whether water is fresh or saline, and additionally, as saline droplets evaporate, the density increases as salinity increases. Momentum flux is dependent on density, as seen in the equation above, and therefore as density changes the momentum flux will also change. The number of droplets also plays a role in the momentum flux, and as discussed above, more droplets are seen in saltwater conditions than in freshwater conditions. More droplets will in turn create more air-sea stress, and as the droplets change acceleration, will alter the near-surface wind and influence air-sea drag (Veron, 2015).

We can also consider the droplet residence time, by looking at terminal fall speed (Andreas, 1989):

$$u_f = \frac{2r^2 g}{9\nu_a\left[1 + 0.158\left(2r\frac{u_f}{\nu_a}\right)^{\frac{2}{3}}\right]}\left(\frac{\rho_s}{\rho_a} - 1\right) \tag{6}$$

In saltwater, which has a higher density, the residence time is going to be shorter, as represented by a higher terminal fall speed in the above equation. In freshwater, the residence time will be longer. A shorter residence time leads to less time for the droplet to interact with the ambient air in the boundary layer before re-entering the water, and therefore giving less time for evaporation and less heat and momentum flux to the atmosphere.

Spray droplets initially have the same temperature as the surface of the water that they developed from, and as they exchange heat with the air, they transfer sensible heat to the air as they cool and begin evaporation, which extracts latent heat from the air (Andreas, 1989). Quantitatively we can also see that the difference in fresh and salt water will impact heat transfer between droplets and the air following Pruppacher and Klett (1978)'s equation for change in radius of an aqueous solution droplet:

$$r\frac{dr}{dt} = \frac{D_w' M_w e_{sat}(T_a)}{\rho_s R T_a}\left\{f\frac{1}{1+\delta}exp\left[\frac{L_v M_w}{R T_a}\left(\frac{\delta}{1+\delta}\right) + \frac{2M_w\sigma_s}{R T_a(1+\delta)\rho_w r} - \frac{v\phi_s m_s\left(\frac{M_w}{M_s}\right)}{\left(\frac{4r^3\rho_s}{3}\right) - m_s}\right]\right\} \tag{7}$$

where:

r = instantaneous radius of droplet

ρ_s = density of droplet

ρ_w = density of water

m_s = mass of NaCl in droplet

D'_w = modified molecular diffusivity of water

R = universal gas constant

L_v = latent heat of vaporization of water

M_w = molecular weight of water

M_s = molecular weight of NaCl

T_a = ambient air tempertaure

f = fractionsl relative humidity

$e_{sat}(T_a)$ = saturation vapor pressure over a pure flat water surface

σ_s = surface tension of a flat surface with the same temperature and salintiy as droplet

ϕ_s = practical osmotic coefficient of the droplet

v = number of ions into which a salt molecule in the droplet dissociates

and

$$\delta = \frac{T}{T_a} - 1 = \frac{L_v \rho_s}{T_a k'_a} r \frac{dr}{dt}$$

From this equation, we can see that the differences between freshwater and saltwater will influence the change in radius of the droplets through many variables, including the molecular weight of NaCl, the surface tension, the ions into which the salt molecule dissociates, the density of the droplet, and density of water. We can see that salinity effects the droplet radius with time based on observations and the model of Andreas (1989) (Fig. 10). It takes more time (~0.5 s) for the freshwater droplet (2 ppt) to reduce in size, and when the reduction begins it occurs more rapidly than in saline droplets (29 ppt), which begin evaporation at ~0.08 s.

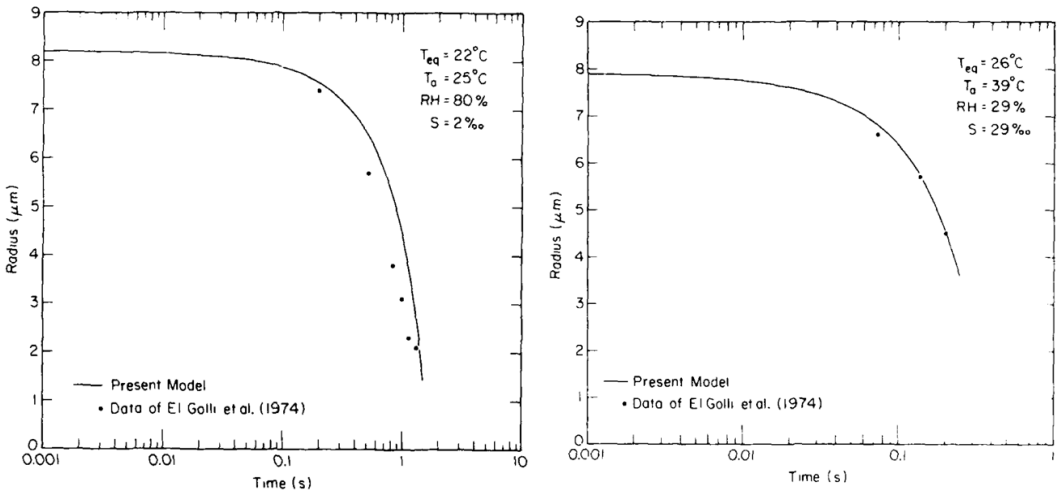

Figure 10. (left) Model and experimental results with salinity of 2 ppt. (right) Model and experimental results with salinity of 29 ppt (from Andreas, 1989).

Extremely small spray droplets (<20 μm) contribute little to the enthalpy flux, as they are carried away in the turbulent air flow quickly and likely make little contribution to enthalpy through evaporation (Andreas & Mahrt, 2016). The spray droplets that contribute most to enthalpy flux are those in the spume range (>25 μm), which have time to reach equilibrium with the air and re-enter the water. The range of these droplets will be dependent on salinity, as the density is changes as we move from fresh to salt water (Andreas & Mahrt, 2016). As density changes due to salinity, this will affect wave speed, as they have an inversely proportional relationship: as density increases, wave speed decreases, and vice versa. This is important for wave height in that as wave speed changes, so does the wave height, again with an inversely proportional relationship. While this is an indirect effect of salinity on spray generation, it does impact enthalpy exchange from spray. Larger spray droplets (spume), which are generated at the wave crest, fall back into the water after exchanging heat and momentum with the atmosphere. If waves are smaller, droplets have less distance before returning to the water, and therefore less time for atmospheric exchange (Andreas & Mahrt, 2016). The spray sensible and latent heat fluxes following Bao et al., (2011) are as follows:

$$H_s = \rho_w c_w F_M \left[T_s - \left(T_w + \delta T_w \right) \right]$$
$$H_L = \rho_w L_v F_E \left[Q_s \left(T_a + \delta T_a \right) - Q_s \left(T_d + \delta T_d \right) \right]$$

where

$\rho_w =$ is the density of seawater

$c_w =$ the heat capacity of water

$Q_s(T) =$ the gridbox mean saturation specific humidty at temperature T

$F_M =$ spray droplet mass flux

$F_E =$ spray droplet water − vapor flux

(8-9)

Here we can see that the heat capacity and density, which change with salinity, directly impact the sensible and latent heat fluxes from spray droplets. Increasing heat capacity will increase sensible heat flux, as the water can store more heat to transfer.

Lastly, we can look at how the characteristic differences between freshwater and saltwater will impact aerosol formation. When a spray droplet evaporates, it leaves behind a dried particle, or aerosol, that can be carried extremely long distances, transporting organic and inorganic compounds. Sea salt aerosols have been found to be nuclei for cloud condensation and marine fog (Cipriano et al., 1987; Woodcock, 1978), as well as influence climate through scattering of solar radiation (Murphy et al., 1998). The overall composition of the aerosol particle determines how effectively they can form cloud condensation nuclei, making the water source an important factor (Wang et al., 2017). Wang et al., 2017 found that sub-micrometer sea spray aerosols not only form from film droplets, but also jet droplets, which have a composition consisting of solutes derived from biological activity. Since both jet and film droplets are generated in freshwater, the differences in composition critical for aerosols that were found in Wang et al., 2017 will not be discussed here. What is important regarding the difference between freshwater and saltwater in this aspect is that the contents of the sea surface microlayer that is often transported and retained in aerosols will differ between freshwater and saltwater, simply because the microbial communities are different in the two environments. Also, as previously discussed, in seawater there is a higher number of droplets produced by bubble-mediated spray mechanisms, meaning that in seawater there will be a higher number of aerosols produced than in freshwater as well.

The impact of salinity on aerosol formation has not been extensively studied, but the literature overall agrees follows that of the influence of salinity on spray droplet generation. Observations show that there is increased aerosol production and a shift to larger aerosol diameters as salinity increases, as well as that there is a higher production sensitivity at lower salinities (Mårtensson et al., 2003; Tyree et al., 2007; Zábori et al., 2012). Viscosity, which increases with salinity, also will have an impact on the Reynold's number following Ovadnevaite et al. (2014), which will in turn alter spray generation and the resulting aerosol particles. Freshwater aerosols will have lower overall solute concentrations due to a lack of salt, therefore resulting in a smaller aerosol particle than those produced by saltwater (Slade et al., 2010). Zinke et al. (2022) found three regimes in aerosol production related to salinity ranges: 1) a high salinity regime in which salinity fluctuations only slightly altered particle numbers; 2) an intermediate regime where particle numbers were highest; and 3) a low salinity regime in which aerosol particles reduced dramatically and shifted to smaller diameters. May et al. (2016) characterized the differences in chemical composition between freshwater and saltwater aerosol particles, finding that freshwater contained much lower inorganic ion concentrations than saltwater, differences in inorganic ion composition than saltwater, and similar concentrations of total organic carbon and total inorganic carbon. Park et al. (2022) found that the concentration and diameter of aerosols increased proportionally with increasing salinity up until 10 ppt, where concentration and diameter stabilized. Their results emphasize that estuarine (<10 ppt) and freshwater likely produce an insignificant number of aerosol particles and that salinity may be a limiting factor in aerosol production. However, freshwater aerosols could have similar effects on climate as saltwater aerosols, as demonstrated by 'lake effect' snow that is often seen in areas such as the Great Lakes region (Scott & Huff, 1996).

Overall, there are a multitude of variables that play a role in the complex phenomenon of spray generation in both freshwater and saltwater and understanding which play the most significant part in generation, heat and momentum fluxes, and aerosol formation requires further investigation.

1.6. Effects of spray on air-sea gas exchange

Air-sea gas exchange influences biogeochemical gas budgets and pollutant transport between the ocean and atmosphere (Ho et al., 2004). Gas exchange relies heavily on the gas

transfer velocity, which is key to gas exchange, depends on a variety of factors including near-surface turbulence, wind speed, wave breaking, the presence of surfactants, bubbles, and spray and spume (Ho et al. 2004, Wanninkhof et al., 2009; Jähne, 2019). While air-sea gas exchange has been studied for over 40 years (Jähne, 2019), gas exchange under tropical cyclones has been only briefly studied due to obvious difficulties in data collection. In the field, gas transfer velocities were estimated during Hurricane Frances 2004 (McNeil & D'Asaro, 2007), while in wave tanks 1,4-difluorobenzene and hexafluorobenzene (Krall & Jähne, 2014) and carbon dioxide (Iwano et al., 2013) have been used as tracers in freshwater to study gas exchange. Based on these limited results, it is believed that gas transfer velocities increase as wind speeds do, specifically above 33 to 35 m s^{-1}. Factors that play a role in gas exchange at high winds include bubbles, wave breaking and spray generation, and near-surface turbulence. Bubbles increase surface area for gas transfer and increase near-surface turbulence when they burst, both leading to increased gas transfer velocities, but bubble mediated gas transfer still relies on solubility (Krall et al., 2019). While bubble induced gas transfer has been relatively well studied (Maiß, 1986; Patro et al., 2002; Asher et al., 1996; Mischler, 2014; Asher et al., 1995; Leifer & De Leeuw, 2002), spray mediated gas exchange remains understudied. Gas diffusion of spray begins with diffusion within the interior of the droplet, then diffusion across the droplets interface, and finally diffusion between the air boundary layer outside the droplet and the bulk atmosphere. Carbon dioxide diffusion also includes the timescales of the kinetics involved in these diffusion steps. Spray gas diffusion occurs more quickly than spray evaporation, and therefore spray temperature and radius changes during evaporation may be limiting factors in spray-mediated gas transfer (Andreas et al., 2017).

Solubility is not a factor in spray mediated gas exchange, meaning spray provides simply adds surface area for increased gas exchange (Krall et al., 2019). Details about spray mediated gas exchange remain uncertain, such as how long gas exchange occurs. The behavior of spray, whether droplets are small and fully evaporate, or they are large and re-entrant, heavily influences gas exchange. Andreas et al. (2017) found that most spray mediated gas exchange is independent of the Schmidt number. Krall et al. (2019) was the first to study air-sea gas exchange in seawater under high winds using wind-wave tanks at Kyoto University and University of Miami. Experiments were conducted using both fresh and seawater and winds ranged from 7 to 85 m s^{-1}. They found that above 33 m s^{-1} gas transfer increase dramatically across the air-sea interface, and that bubbles had little to no impact on gas exchange, although this could be due to the young waves

produced by the tanks. Their experiments also revealed that the gas transfer velocity dependence on solubility is reduced dramatically for sea spray under high winds. Andreas et al. (2017) found that spume droplets have a higher contribution to air-sea gas exchange than smaller spray droplets, as determined by calculating the sea spray generation function as a volume flux (Fig. 11). Since spume droplets are larger, they have more water and therefore contribute more to heat, momentum, and gas transfers at the air-sea interface than small droplets. Potentially, gas flux at high winds is proportional to surface area of spray since it is no longer dependent on gas solubility. Spray and spume generation are dramatically increased under increasing wind speeds, meaning that the gas flux may also increase significantly.

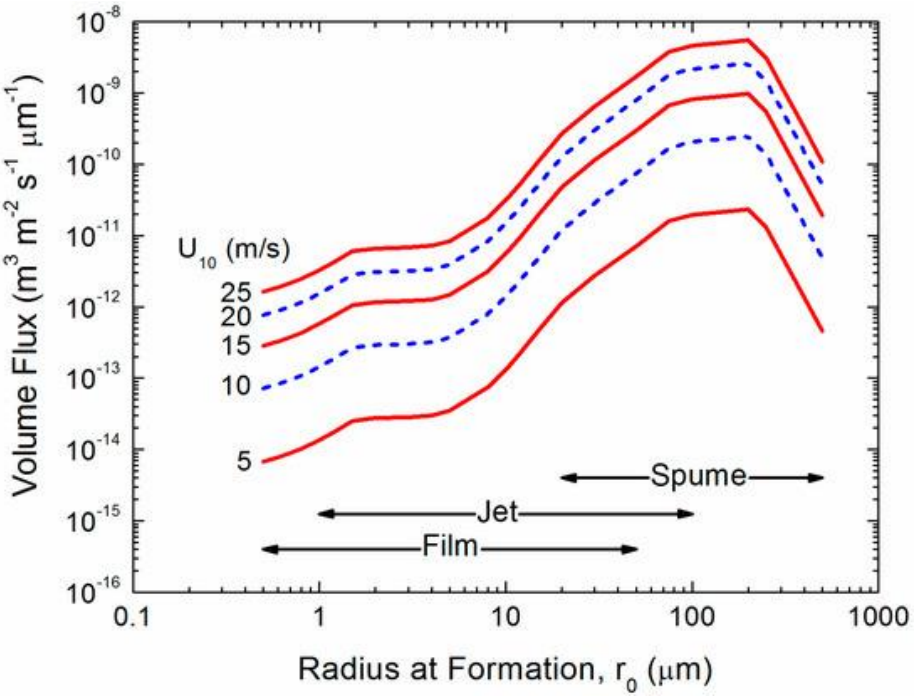

Figure 11. The spray generation function as a volume flux (Andreas et al., 2017).

The modeling work of Staniec et al. (2021) found that sea spray has a significant effect on gas flux at the air-sea interface under high winds (above 18 m s^{-1}) for gasses such as oxygen and potentially carbon dioxide. Areas of the ocean subject to high winds, including the Southern Ocean (Fig. 12) or under tropical cyclones, could be particularly important in estimating air-sea gas flux due to the contribution of sea spray.

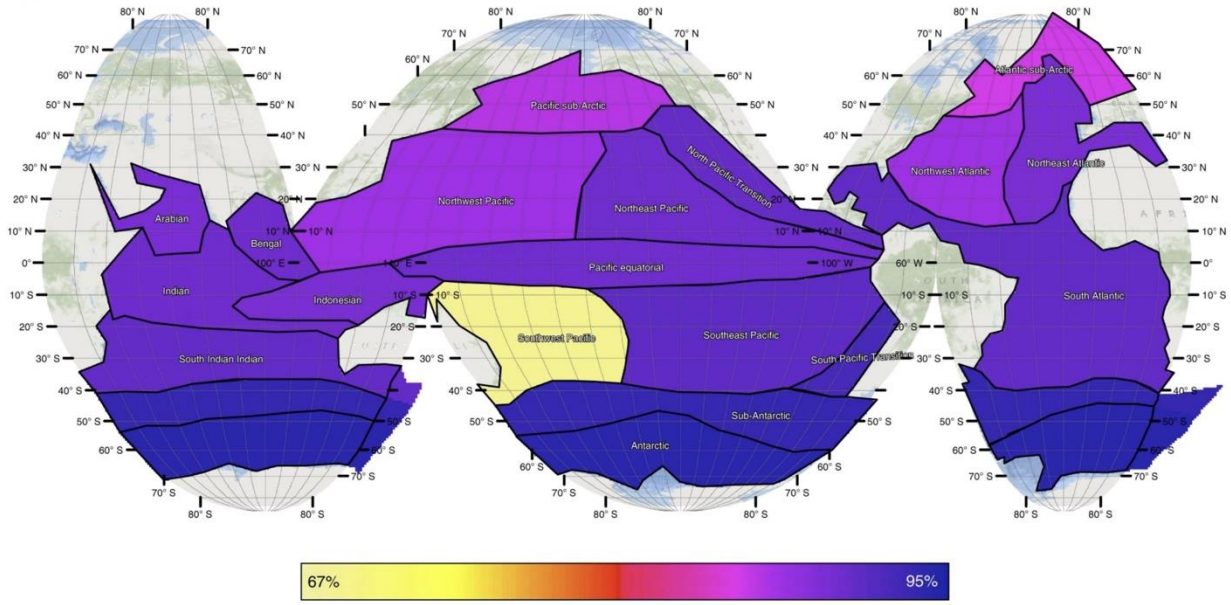

Figure 12. Percent change in gas volume for oxygen of a 100-µm-radius droplet reaching final equilibration. Higher impacts of gas exchange by spray are colored in purple and lower in yellow (Staniec et al., 2021).

Gutiérrez-Loza et al. (2022) specifically looked at carbon dioxide transfer under high and intermediate winds, finding that spray is an efficient mechanism for exchange of CO_2, with the highest transfer rates being during winter seasons, when evaporation increases due to try atmospheric conditions. Additionally, when significant wave heights were high (above 1.5 m), gas transfer was further enhanced, likely due to sea spray.

Surfactants add another aspect into understanding this phenomenon. Because surfactants dampen waves and form slicks under low winds, they alter the wave slope spectra which has been shown to reduce gas exchange (Frew, 1997; Bock et al., 1999). These slicks likely have a significant effect on the air-sea gas exchange rates of many gases, including greenhouse gases such as carbon dioxide, methane, and nitrous oxide (Wurl et al., 2011). The coverage, concentration, and composition of sea surface slicks caused by surfactants vary depending on wind, sea conditions, and with time. Jähne (2019) considered the effect of surface films under low wind speed conditions, pointing out that even a 1% reduction in surface tension by surfactants can significantly affect the Schmidt number, and consequently the gas transfer velocity. Surfactants also increase spray generation (Vanderplow et al., 2020) and therefore potentially increase the gas

flux through increased spray and spume concentration, which is a consideration of this dissertation work.

1.7. Small-scale to mesoscale oceanic features and circulation

Sub-mesoscale flows have a length of 0.1-10 km and are sometimes difficult to observe in the ocean and model because of their short timescales and small length scales (Thomas, Tandon & Mahadevan, 2008; Bachman et al., 2017; Su et al., 2018). Some ocean features such as ocean fronts and internal wave solitons require even smaller spatial resolution starting from a few meter scales. Resolving the range from small scales (below 0.1 km) to sub-mesoscales is especially a challenge in a strong current like a western boundary current. We are developing an approach to address this challenge using field and computational experimentation in the Straits of Florida as an example.

The Florida Current, with current speeds up to ~2.5 m s^{-1}, is a part of the North Atlantic Western Boundary Current. According to Stommel (1965), the Loop Current in the Gulf of Mexico becomes the Florida Current in the Straits of Florida and the Gulf Stream leaving the Straits of Florida. The Florida Current is characterized by intense mesoscale (>10 km), sub-mesoscale, and small-scale variability including a variety of features such as meanders, eddies, fronts, and internal waves that are caused by the flow over a highly variable bottom topography and air-sea interaction. There is also a seasonally modulated undercurrent/countercurrent jet attached to the continental shelf of Florida (Soloviev et al., 2017).

Current circulation on the Southeast Florida shelf is associated with the many processes occurring in the Florida Current in time and space scales, including inhomogeneities caused by bottom topography, barotropic and baroclinic tides, meteorological forcing, and stratified current structure. Variations in the Florida Current caused by seasonal and interannual variability represent ~70% of the total variance attributed to less than annual periods (Schott et al., 1988; Meinen et al., 2010). In addition, frontal mesoscale and sub-mesoscale eddies periodically develop in the Straits of Florida. The Florida Current also has prominent current oscillations on ~10-hour time scales observed on the Florida shelf. These oscillations are seasonally modulated and reach a maximum during the summer (Soloviev, Luther, & Weisberg, 2003; Soloviev et al., 2003).

The Florida Current reveals seasonal to tidal variability but is generally steady over a timescale of years. Transport is highest in the spring and summer and decreases in the fall,

associated with along-channel winds in the Straits of Florida (Lee and Williams, 1988) and wind forcing in the North Atlantic (Schott et al., 1988). Wind forcing and continental shelf waves lead to meanders and frontal eddies in the Florida current, resulting in variability at timescales of days to weeks (Davis et al., 2008). Large cyclonic, cold-core eddies that form near the Dry Tortugas move northeast on the western side of the Florida Current (Lee et al., 1995) and eventually elongate into mesoscale and sub-mesoscale eddies near the middle and upper Florida Keys (Haus et al., 2000). Sub-mesoscale frontal eddies are also generated near offshore meanders in the Florida Current, which lead to water mass exchange between the Florida Current and the shelf (Haus et al., 2004). Internal waves are generated from fronts or eddies in the Florida Current and tidal forces (Davis et al., 2008). Internal tidal velocity fluctuations of up to 0.5 m s^{-1} have been observed in the surface waters of the Straits of Florida (Pillsbury, 1891; Parr, 1937; Schimtz & Richardson, 1968). Soloviev, Luther, & Weisberg (2003) observed similar oscillations with periods of 10 hours and a seasonal modulation that peaks during the summer. The 10-hour period aligns closely with the semidiurnal tidal constituents present in the Florida Straits (M_2 12.42 hours and S_2 12 hours) (Soloviev, Luther, & Weisberg, 2003). However, no definitive explanation for the 10-hour internal wave oscillation has been established since the time of the Pillsbury (1891) discovery.

Understanding and characterizing small and mesoscale ocean dynamics and circulation is important to tropical cyclone dynamics; as is the reverse, the impact of tropical cyclones on ocean dynamics. Small and mesoscale ocean circulation and characteristics, particularly in environments such as a western boundary current, lead to complex interaction between ocean circulation and tropical cyclones (Schade & Emanuel, 1999; Ezer, 2019). Researchers have studied the impacts of tropical cyclones on the Loop Current (Oey et al., 2006), on the Gulf Stream (Kourafalou et al., 2016; Ezer et al., 2017; Ezer, 2018b; Todd et al., 2018), and on the Kuroshio Current (Wu et al., 2008; Liu & Wei, 2015). Not only are ocean dynamics in the open ocean affected by tropical cyclones, but the impacts can extend to coasts outside of the predicted storm impact area, leading to unprepared coastal communities due to these poorly understood interactions. One such example, shown by Ezer et al. (2017) and Ezer (2018a,b; 2019), is that tropical cyclones may reduce Gulf Stream transport and flow leading to increasing sea level and flooding of nearby coasts. Todd et al. (2018) also found that the flow of the Gulf Stream was reduced by tropical cyclone interaction by up to 40% during the 2017 hurricane season. Characterizing small and mesoscale dynamics in challenging environments like western boundary currents can also yield more accurate initial

conditions ahead of and behind tropical cyclones. This can improve parameterizations of variables such as mixing and fluxes in tropical cyclone forecasting models (Sanabia & Jayne, 2020).

2. Goals and Objectives

This project intends to further understand processes at the air-sea interface under tropical cyclone conditions, in particular sea spray and spume generation, the sea spray generation function (SSGF), spray evaporation and condensation, heat and momentum fluxes, air sea gas exchange, and the impacts of factors such as surfactants. Additionally, the project explores the gap between micro- and small-scale to mesoscale ocean circulation and potential uses of this for understanding and predicting tropical cyclone dynamics.

Hypotheses

- The SSGF for high winds from this work will more accurately estimate the impact of spray on tropical cyclones, which has been underestimated in tropical cyclone forecast models.
- Surfactants will alter the SSGF by increasing spray generation overall as well as shifting the peak to smaller radii.
- The addition of surfactants will lead to a higher number of nonspherical particles due to their reduction of surface tension on the perimeter of the spray droplet.
- Temperatures of largest particles (re-entrant spray) will contribute more to the enthalpy flux to tropical cyclones, since they only remain in the air for a short time and will remain at temperatures close to the sea surface water.
- Gas exchange flux at high winds may be dependent on spray and spume surface area, which is dramatically increased during tropical cyclones, particularly when surfactants are present.
- Applying a similar CFD approach for ocean circulation in a western boundary current will help characterize small to mesoscale ocean processes, which could be applied to understanding coupled upper ocean-atmosphere interactions before, during, and after tropical cyclone passage.

Objectives

- Complete the ANSYS VOF-to-DPM model runs for Category 2 and 4 tropical cyclone conditions with and without surfactants.
- Analyze laboratory experiments from University of Miami and other laboratory facilities to study the various processes included in this dissertation under tropical cyclone force winds and gather data for model verification.
- Utilize numerical and laboratory data to produce a sea spray generation function for high wind speeds and in the presence and absence of surfactants.
- Implement ANSYS Fluent Computational Fluid Dynamics (CFD) Volume of Fluid to Discrete Phase Model (VOF-to-DPM) in combination with the Evaporation-Condensation model and user-defined function, if necessary, to model sea spray generation and distribution, evaporation, and heat and momentum exchange under tropical cyclone conditions.
- Implement the DPM-to-VOF transition mechanism to model re-entrant spray.
- Explore the application of satellite oceanography to associate chlorophyll as a proxy for surfactants to tropical cyclone tracks and intensity.
- Implement a computational fluid dynamics model of small to mesoscale ocean circulation to better understand and predict ocean processes that relate to tropical cyclone dynamics and intensification. This will include implementing the same remeshing algorithm as the VOF-to-DPM model into an ocean circulation model to fill the gap between micro- and small-scale and mesoscale ocean processes.

3. ANSYS Fluent CFD Model Theory

ANSYS Fluent CFD software provides a large assortment of physical model capabilities, which include flow, turbulence, multiphase, and heat transfer. To model sea spray generation under tropical cyclone conditions, we use a combination of Fluent's Large Eddy Simulation for turbulence (LES), the Volume of Fluid (VOF) for multiphase flow, and the Discrete Phase Model (DPM) for particle/droplet tracking. Recently, Fluent implemented the Volume of Fluid to Discrete Phase Model (VOF-to-DPM), which combines the two models, effectively allowing spray/droplet generation and tracking as the model progresses.

3.1 *Large Eddy Simulation*

Large Eddy Simulation (LES) models turbulence. The LES model resolves large eddies as they incorporate momentum, mass, and energy, and are heavily influenced by the geometry and boundary conditions in the model. Large eddies in this context are those comparable to the length of the mean flow of the model (our domain length is 0.1 m). Meanwhile, small eddies are more universal when modeling turbulence. The LES governing equations are formulated from time-dependent Navier-Stokes equations, which are filtered in either Fourier (wave number) space or configuration (physical) space. Filtering removes eddies with scales that are too small for the grid spacing in Fluent. These equations do not include gravity, as gravity is independently defined in the operating conditions of Fluent and is treated as a source term. Once gravity is activated, Fluent will redefine other equations to include it. Coriolis is also absent but can be added to Fluent through a User-Defined Function, which allows the addition of parameters to any Fluent model. The following equations are those used for incompressible flows.

After filtering the Navier-Stokes equations, the following equations remain:

$$\frac{\partial \rho}{\partial t} + \frac{\partial}{\partial x_i}(\rho \bar{u}_i) = 0 \tag{10}$$

$$\frac{\partial}{\partial t}(\rho \bar{u}_i) + \frac{\partial}{\partial x_j}\left(\rho \bar{u}_i \bar{u}_j\right) = \frac{\partial}{\partial x_j}\left(\sigma_{ij}\right) - \frac{\partial \bar{p}}{\partial x_i} - \frac{\partial \tau_{ij}}{\partial x_j} \tag{11}$$

where u is the fluid velocity vector, ρ is the fluid density, p is the fluid pressure, σ_{ij} is the stress tensor caused by molecular viscosity, which is defined by:

$$\sigma_{ij} \equiv \left[\mu\left(\frac{\partial \bar{u}_i}{\partial x_i} + \frac{\partial \bar{u}_j}{\partial x_i}\right)\right] - \frac{2}{3}\mu \frac{\partial \bar{u}_l}{\partial x_l}\delta_{ij} \tag{12}$$

where μ is viscosity and δ_{ij} is the Kronecker delta.

τ_{ij} is the subgrid-scale stress, which is defined by:

$$\tau_{ij} \equiv \rho\overline{u_i u_j} - \rho\bar{u}_i\bar{u}_j \tag{13}$$

Turbulence models for subgrid-scales use the Boussinesq hypothesis, which calculates stresses from the following equation:

$$\tau_{ij} - \frac{1}{3}\tau_{kk}\delta_{ij} = -2\mu_t\bar{S}_{ij} \tag{14}$$

where μ_t is the subgrid-scale turbulent viscosity, τ_{kk} is the isotropic portion of the subgrid-scale stresses, and $\bar{S}_{ij}$ is the rate-of-strain tensor for the resolved scale. $\bar{S}_{ij}$ is defined as:

$$\bar{S}_{ij} \equiv \frac{1}{2}\left(\frac{\partial\bar{u}_i}{\partial x_j} + \frac{\partial\bar{u}_j}{\partial x_i}\right) \tag{15}$$

For compressible flows, the Navier-Stokes equation is filtered using a density-weighted filtering operator:

$$\tilde{\phi} = \frac{\overline{\rho\phi}}{\bar{\rho}} \tag{16}$$

where ϕ is the subgrid-scale turbulent flux of a scalar.

The subgrid stress tensor for compressible flow is as follows:

$$\tau_{ij} = \bar{\rho}\widetilde{u_i u_j} - \bar{\rho}\tilde{u}_i\tilde{u}_j \tag{17}$$

The tensor term can be split into isotropic and deviatoric parts:

$$\tau_{ij} = \tau_{ij} - \frac{1}{3}\tau_{kk}\delta_{ij} + \frac{1}{3}\tau_{kk}\delta_{ij} \tag{18}$$

deviatoric isotropic

The deviatoric part of the tensor uses the compressible method of the Smagorinsky model, which is as follows:

$$\tau_{ij}^{r} - \frac{1}{3}\tau_{kk}\delta_{ij} = -2v_t\bar{S}_{ij} \quad (19)$$

where v_t is the turbulent eddy viscosity and $\bar{S}_{ij}$ is the rate-of-strain tensor, which is defined as:

$$\bar{S}_{ij} = \frac{1}{2}\left(\frac{\partial \bar{u}_i}{\partial x_j} + \frac{\partial \bar{u}_j}{\partial x_i}\right) \quad (20)$$

A scalar's subgrid-scale turbulence is modeled using a subgrid-scale turbulent Prandtl number:

$$q_j = -\frac{\mu_t}{\sigma_t}\frac{\partial \phi}{\partial x_j} \quad (21)$$

where q_j is the subgrid-scale flux.

We use the Wall-Adapting Local Eddy-Viscosity (WALE) model to model eddy viscosity, which is calculated using:

$$\mu_t = \rho L_s^2 \frac{(S_{ij}^d S_{ij}^d)^{3/2}}{(\bar{S}_{ij}\bar{S}_{ij})^{5/2} + (S_{ij}^d S_{ij}^d)^{5/4}} \quad (22)$$

where L_s and S^d_{ij} are:

$$L_s = \min\left(\kappa d, C_\omega V^{1/3}\right) \quad (23)$$

and

$$S_{ij}^d = \frac{1}{2}\left(\bar{g}_{ij}^2 + \bar{g}_{ji}^2\right) - \frac{1}{3}\delta_{ij}\bar{g}_{kk}^2, \bar{g}_{ij} = \frac{\partial \bar{u}_i}{\partial x_j} \quad (24)$$

where κ is the Kármán constant (0.41) and C_ω is the WALE constant (0.325) Fluent uses a default value of 0.325 for the WALE constant because it has been tested and found to yield satisfactory results for a wide range of flows (*ANSYS Fluent Theory Guide 2022R1*, 2022). Kulyakhtin et al. (2014) used both RANS, which was previously typically used in wave

modeling, as well as LES, and reported that the results were similar. Jiang et al. (2019) also used LES to model wave interaction.

3.2. Volume of Fluid

The VOF model tracks the interface between phases in the model. To do so, a continuity equation is calculated for the volume fraction of each phase. The following equation is used for the qth phase:

$$\frac{1}{\rho_q}\left[\frac{\partial}{\partial t}\left(\alpha_q \rho_q\right) + \nabla\cdot\left(\alpha_q \rho_q \vec{v}_q\right) = S_{\alpha_q + \sum_{p=1}^{n}\left(\dot{m}_{pq} - \dot{m}_{qp}\right)}\right. \tag{25}$$

where $\dot{m}_{qp}$ is the mass transfer from the q phase to the p phase. $\dot{m}_{pq}$ is the mass transfer from the p phase to the q phase. S_{α_q} , the source term on the right side, is zero.

We use an explicit solver, in which the standard finite-difference interpolation schemes are applied to the volume fraction values from equation 16 (*ANSYS Fluent Theory Guide 2022R1*, 2022).

$$\frac{\alpha_q^{n+1}\rho_q^{n+1} - \alpha_q^n \rho_q^n}{\triangle t} V + \sum_f \left(\rho_q U_f^n \alpha_{q,f}^n\right) = \left[\sum_{p=1}^{n}\left(\dot{m}_{pq} - \dot{m}_{qp}\right) + S_{a_q}\right] V \tag{26}$$

where n+1 is the index for the current time step, n is the index for the previous time step, $\alpha_{q,f}$ is the face value of the qth volume fraction, V is the volume of the cell, and U_f is the volume flux through the face.

Energy and momentum are calculated throughout the domain by Fluent, which means the velocity fields are shared by the phases in the model. Because of this, the momentum equation depends on ρ and μ of the phase volume fraction, as shown below:

$$\frac{\partial}{\partial t}\left(\rho\, \vec{v}\right) + \nabla\cdot\left(\rho\, \vec{v}\vec{v}\right) = -\nabla p + \nabla\cdot\left[\mu\left(\nabla\vec{v} + \nabla\vec{v}^T\right)\right] + \rho\, \vec{g} + \vec{F} \tag{27}$$

where p is the static pressure, ρg and $\vec{F}$ are the gravitational body force and external body forces.

The energy equation is as follows:

$$\frac{\partial}{\partial t}(\rho E) + \nabla\cdot(\vec{v}(\rho E + p)) = \nabla\cdot(k_{eff}\nabla T) + S_h \tag{28}$$

where κ_{eff} is the effective conductivity, S_h includes defined volumetric heat sources, and energy, *E*, and temperature, *T*, are considered mass-averaged variables in Fluent. Mass averaged energy is calculated as follows:

$$E = \frac{\sum_{q=1}^{n} \alpha_q \rho_q E_q}{\sum_{q=1}^{n} \alpha_q \rho_q} \tag{29}$$

where E_q for each phase depends on the specific heat and temperature of the phases, defined by:

$$E_q = h_q - \frac{p}{\rho_q} + \frac{v^2}{2} \tag{30}$$

where h_q for each phase is based on the specific heat of that phase and the shared temperature. The continuum surface force (CSF) model by Brackbill et al. (1992) is used to model surface tension (*ANSYS Fluent Theory Guide 2022R1*, 2022).

We use Fluent's open channel flow boundary condition in the VOF model for the waves in our model. Open channel flows are controlled by gravity. inertia forces, and interfacial stresses. The Froude number, which is the ratio of inertia force and hydrostatic force, characterizes the flow:

$$Fr = \frac{V}{\sqrt{gy}} \tag{31}$$

where *V* is the velocity magnitude, *g* is gravity, and *y* is the distance from the bottom to the free surface. The wave speed is calculated as:

$$V_w = V \pm \sqrt{gy} \tag{32}$$

An incident wave profile is calculated as follows:

$$\zeta = Acos(k_x x + k_y y - \omega_e t + \epsilon) \tag{33}$$

where z is the wave height, A is the wave amplitude, ϵ is the phase difference, t is the time, and k_x and k_y are the wave numbers in the x and y directions. Therefore,

$$k_x = kcos\theta \tag{34}$$

and

$$k_y = ksin\theta \tag{35}$$

where θ is the wave heading angle, defined as the angle between the wave front and direction of wave propagation. The wave number k is calculated as:

$$k = \frac{2\pi}{\lambda} \tag{36}$$

where λ is the wavelength and the effective wave frequency ω_e is calculated as:

$$\omega_e = \omega + kU \tag{37}$$

U is the averaged velocity of the flow current, and ω is the intrinsic wave frequency, which is defined as:

$$\omega = \sqrt{gk\ tanh(kh)} \tag{38}$$

where h is the liquid height and g is the gravity magnitude (*ANSYS Fluent Theory Guide 2022R1*, 2022). The VOF model was first developed by Hirt and Nichols (1981) to overcome the problem of modeling two-phases. Following this approach, many researchers have used the VOF model in CFD modeling. Specifically, Kulyakhtin (2014), Hamza et al. (2015), Kim et al. (2016), Zhang et al. (2016), Jiang et al. (2019), and Uddin et al. (2020) used ANSYS Fluent's VOF model to study wave tank simulations.

3.3. *Discrete Phase Model*

The Euler-Lagrange approach is used in Fluent's DPM. Navier-Stokes equations are again solved for this model. The dispersed phase, in our case droplets, can exchange momentum, mass, and energy with the primary phase (water). The droplet trajectories are computed by Fluent at a specified interval (in our case 20 adaptive time steps ranging from 10^{-9} to 10^{-6} s), by using force balance in a Lagrangian reference frame. This is calculated as:

$$\frac{du_p}{dt} = F_D\left(u - u_p\right) + \frac{g_x(\rho_p - \rho)}{\rho_p} + F_x \tag{39}$$

where F_x is an additional acceleration term, $F_D(\mu - \mu_p)$ is the drag force per unit particle mass and F_D is as follows:

$$F_D = \frac{18\mu}{\rho_p d_p^2}\frac{C_D Re}{24} \tag{40}$$

where u is the fluid phase velocity, u_p is the particle velocity, μ is the molecular viscosity of the fluid, ρ is the fluid density, ρ_p is the density of the particle, and d_p is the particle diameter. Re is the Reynolds number, which is calculated as:

$$Re \equiv \frac{\rho d_p |u_p - u|}{\mu} \tag{41}$$

In Fluent, the drag coefficient, C_D, for smooth particles is calculated as:

$$C_D = a_1 + \frac{a_2}{Re} + \frac{a_3}{Re} \tag{42}$$

where a_1, a_2, and a_3 are constants that are used over several ranges of Re by Morsi & Alexander (1972) (*ANSYS Fluent Theory Guide 2022R1*, 2022). Note that this does vary from the traditional drag coefficient formula (Eq. 2).

3.4. VOF-to-DPM

In 2018, ANSYS Fluent introduced the Volume of Fluid to Discrete Phase Model (VOF-to-DPM). The VOF-to-DPM is an innovative model from Fluent that allowed us to generate sea spray down to micrometers of diameter through dynamic mesh adaption. VOF-to-DPM combines two previously existing ANSYS Fluent models, the Volume of Fluid (VOF) and Discrete Phase Model (DPM). The VOF model tracks the volume of water and air in the domain, as well as the air sea interface, while the DPM tracks discrete particles (Fig. 13). These particles are suspended in Eulerian phases, which in our model are water and air. Eulerian phases are tracked, based on the specific location of the phase in space in relation to time, which assumes the phase to be a continuous function. Thus, the volume fraction of phases within the cell must have a sum of one. These particles are calculated based on asphericity and tracked as Lagrangian particles. Lagrangian tracking follows a specific particle as it moves. This method is much easier for the computer to track than a three-dimensional micrometer mesh (*ANSYS Fluent Theory Guide 2022R1*, 2022).

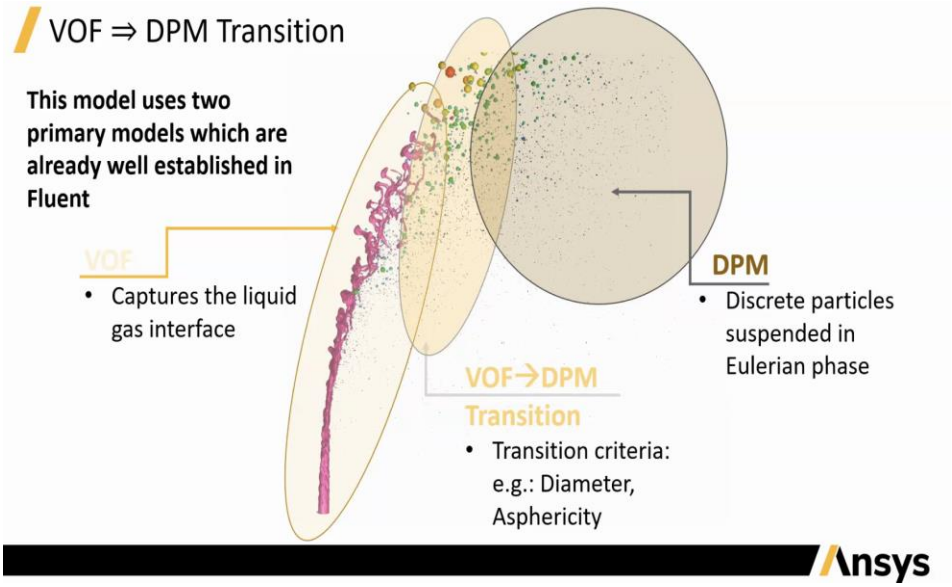

Figure 13. ANSYS Fluent VOF-to-DPM transition model mechanism.

The main aspect of this model that aids in our study is the dynamic mesh adaption, which allows the mesh to be refined and/or coarsened in areas of interest. The area of interest we focus on is the wave crests, where a high amount of sea spray and spume are generated. The mesh adaption criteria are set based on the water volume fraction within each cell of the mesh, as well as the curvature of the waves. Mesh adaption occurs every two time-steps, meaning that it is

adapting constantly as the model progresses. The mesh is set to adapt to up to ten levels of refinement, meaning that each cell can be split up to ten times, increasing our mesh resolution by up to 1000 times. This approach dramatically reduces the initial mesh size, which in turn increases the domain size. ANSYS recently introduced a new PUMA meshing algorithm (in Fluent 2022R1) which is more efficient and can refine even further than previous algorithms to resolve smaller spray (from several tens of μm radius) and more fine-scale phenomena within the model.

3.5. Magnetohydrodynamics (MHD)

ANSYS Fluent has an add-on module, the magnetohydrodynamics (MHD) model, that allows implementation of electromagnetics including magnetic potential and electric potential. A background field is set within the model as well as boundary conditions including insulating, conducting, or thin wall and the material properties involve magnetic permeability and conductivity. The Fluent MHD model describes the electromagnetic fields from Maxwell's equations (*ANSYS Fluent Theory Guide 2022R1*, 2022):

$$\nabla \bullet \vec{B} = 0 \tag{43}$$

$$\nabla \times \vec{E} = -\frac{\partial \vec{B}}{\partial t} \tag{44}$$

$$\nabla \bullet \vec{D} = \rho \tag{45}$$

$$\nabla \times \vec{H} = \vec{J} + \frac{\partial \vec{D}}{\partial t} \tag{46}$$

where $\vec{D}$ is the induction field for the electric field, and $\vec{H}$ is the induction field for the magnetic field, and ρ is the electric charge density. Induction fields for linear media are:

$$\vec{H} = \frac{1}{\mu}\vec{B} \tag{47}$$

$$\vec{D} = \varepsilon \vec{E} \tag{48}$$

where μ is magnetic permeability and $\mathcal{E}$ is electrical permittivity.

The magnetic induction method evaluates the current density, which is derived from Ohm's law and Maxwell's equations (Maxwell 1865). Ohm's law is defined as:

$$\frac{1}{\sigma}\vec{J} = \vec{E} + \vec{v} \times \vec{B} \tag{49}$$

where σ is the electrical conductivity and $\vec{v}$ is the fluid velocity.

ANSYS Fluent first calculates the initial hydrodynamic solution from, and then velocity field calculations are halted through turning off equations for energy and flow. The MHD portion is then calculated and yields the electromagnetic signature from the initial model results.

4. Effects of surfactants on sea spray generation during tropical cyclones

4.1. Methods

4.1.a. Laboratory Experiments

Various experiments related to air-sea interaction have been conducted in wave tanks around the world including the University of Miami, Kyoto University, the University of Delaware, and the Applied Physics Russian Academy of Sciences. Previous experiments used in Vanderplow (2020) were conducted at the University of Miami Rosenstiel School of Marine and Atmospheric Science (RSMAS), using the Air Sea Interaction Saltwater Tank (ASIST) the SUrge STructure Atmosphere INteraction (SUSTAIN) facility.

The ASIST tank (Fig. 14). dimensions are 15 meters, by 1 meter, by 1 meter, with a water level that can be set depending on the experiment. The sides, bottom, and top of the tank are made of acrylic glass, which is transparent and allows for equipment to be placed outside the tank, rather than within.

Figure 14. ASIST at University of Miami RSMAS SUSTAIN Facility (Soloviev et al. 2011).

The ASIST tank contains various equipment to simulate ocean conditions. The wave generator produces waves with frequencies between 0.25 Hz and 3 Hz, and amplitudes between 0 and 0.1 meters. The wind generator can produce winds up to 30 meters per second, while the current generator can produce current speeds up to 0.5 meters per second. Temperature is also controlled and can be kept anywhere between 5 and 40 degrees Celsius. The air in the tank is circulated with either an open or closed loop. Fresh air from the atmosphere is captured and expelled after passing through the tank during the open loop, which is used for gas, humidity, and heat transfer. Saltwater is usually filtered from an inlet near the facility (Ortiz-Suslow et al., 2016).

A Digital Laser Elevation Gauge (DLEG) with line-scan camera and laser beam can easily be set up on the outside of the tank, such as in previous experiments (*i.e.* Ortiz-Suslow et al., 2016). Digital Particle Image Velocimetry (DPIV) can be set to measure and visualize the flow within the tank as well as a *Hisense* camera record images (*i.e.* Soloviev et al., 2011). To capture spray droplets, a collimated light beam focused through a diffusing screen to reduce its intensity can be used. In previous experiments, images of spray droplets were focused on a single plane, located at the center of the ASIST tank. The addition of surfactants to the experiment previously used Oleic acid or oleyl alcohol, which are both insoluble in water. Both were diluted in 95% ethanol to produce various concentrations during the various experimental runs.

Veron et al. (2012) performed spray experiments at the Plexiglas high wind speed wind-wave tank in the Air-Sea Interaction Laboratory at the University of Delaware, which is 7.3 m long, 0.6 m high, 0.48 m wide and made of Plexiglas (Fig. 15). They used a water level of 40-cm and an artificial beach to dissipate wave energy. They conducted experiments under wind speeds of U_{10} = 31.3, 41.2, and 47.1 m s^{-1}. To collect data, they used a high-speed Phantom camera with zoom lens setup outside of the tank, which took 1000x1000 pixel images at a rate of 1000 Hz. A fluorescent backlight was used on the opposite side of the tank from the camera.

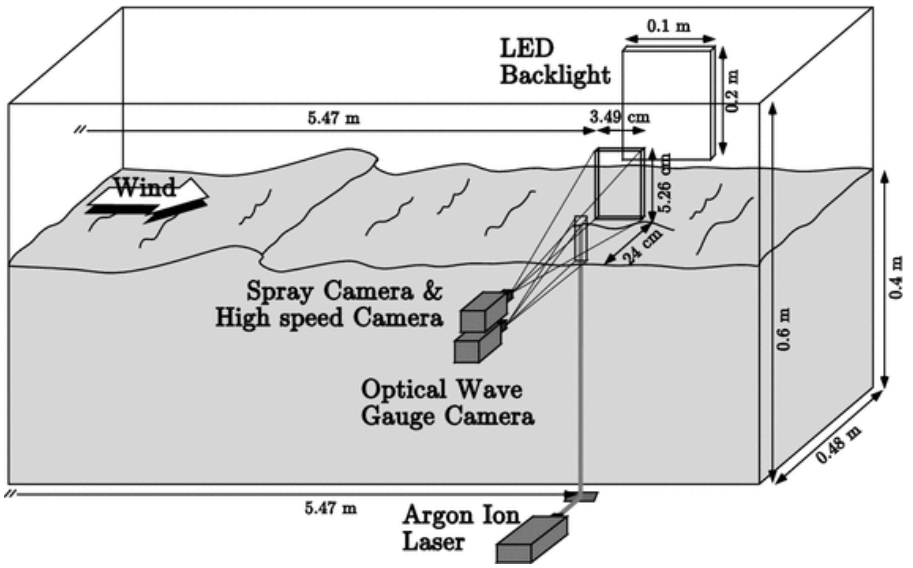

Figure 15. The experimental setup from Veron et al. (2012) at the wind-wave tank at the University of Delaware's Air-Sea Interaction Laboratory.

The Large Thermally Stratified Tank (LTST) at the Institute of Applied Physics Russian Academy of Sciences (IAP RAS) was used in Troistkaya et al. (2017; 2018 a,b; 2019; 2020). The tank is 20 meters, by 4 meters, by 2 meters depth. Temperature can be controlled as well as wind speed can be set up to U_{10} = 40 m s^{-1}, and a wave dampening beach was located at one end of the tank. A high-speed digital NAC Memrecam HX-3 was set up at both a side and top view of the tank to capture the air-water interface and spray. Backlighting was also used: a matte screen and LED lights for the horizontal and underwater illumination for the vertical.

The Kyoto high-speed wind-wave tank is an 80-cm wide linear flume shaped tank with a length of 15.7 m and 1.6 m height. A radial fan is used to generate winds up to U_{10} = 67.1 m s^{-1}. The circulation is open in the tank, with air being taken from the local room and then forced out

of the building after exiting the tank. Water is directly fed into the tank via an external water tank connected by pipes to draw the water into the upwind side and out the downwind side of the tank (Krall & Jähne, 2014).

4.1.b. Computational fluid dynamics modeling

ANSYS Fluent is CFD software, which has a broad range of physical model capabilities including flow, turbulence, multiphase, and heat transfer. In our models, we use the Large Eddy Simulation (LES) to model turbulence. The LES model resolves large eddies as they incorporate momentum, mass, and energy, and are heavily influenced by the geometry and boundary conditions in the model. Meanwhile, small eddies are more universal when modeling turbulence (*ANSYS Fluent Theory Guide 2022R1*, 2022). ANSYS FLUENT 2022R1 was used to model the effect of surfactants on the generation of sea spray under tropical cyclone conditions. For further consideration of the theory behind FLUENT models, please see the *ANSYS Fluent Theory Guide 2022R1* (2022).

The model domain, shown in Figure 16, was created in ANSYS Workbench and consisted of a 0.1 m (x) by 0.1 m (y) by 0.05 m (z) box with an initial mesh size of 0.002 m. This mesh was then adapted, as previously described, allowing for remeshing down to tens of micrometers to confidently resolve spray particles starting from a 100 μm radius. Boundary conditions were set to zero shear on lateral sides and bottom of the domain. The domain contained air and water, with the water being initialized with a wavy interface from the inlet. Wind stress was applied at the top of the domain. This was set according to the strength of tropical cyclone conditions being modeled, 4 Nm^{-2} for Category 1, 10 Nm^{-2} for Category 3, and 20 Nm^{-2} for Category 5. An assumption made here is that the wind stress is constant, and the model does not account for wind gusts that occur during tropical cyclone conditions. The model was run to allow the initialized waves to set up before setting periodic boundary conditions at the inlet and outlet, which permitted the waves to propagate through the domain.

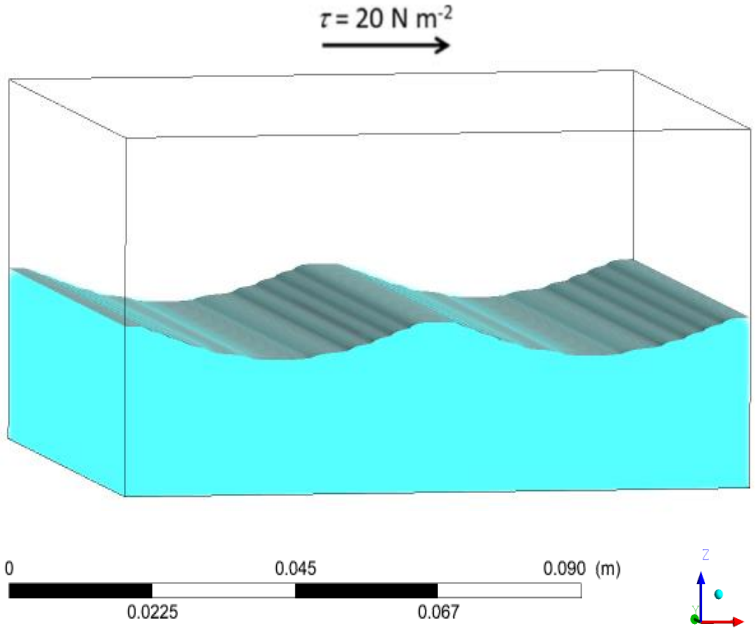

Figure 16. Initial model setup shown in ANSYS Fluent.

The model was run in parallel on 264 processors on a 564 core HPC Linux cluster with 12 compute nodes. We used a pressure-based, transient, 1st order implicit solver and a Large Eddy Simulation to model turbulence. Operating conditions were set to 293.15 K, 9.81 m s^{-1} gravity, and 1013.25 Pa atmospheric pressure. We specified the materials in our domain as water with a bulk temperature T=298 K, density ρ=1000 kg m^{-3}, viscosity μ = 0.001003 kg·m^{-1}·s^{-1}, and specific heat *cp*=4182 J kg^{-1}K^{-1}, and air with bulk temperature T=298.15 K, density ρ=1.225 kg m^{-3}, viscosity μ = 1.7894e^{-05} kg·m^{-1}·s^{-1} , and specific heat *cp*=4182 J kg^{-1}K^{-1}. Time steps within the model were set to adaptive, meaning the time step was automatically adjusted based on the global Courant number. Doing this allowed the time step to determine the stability for the speed of the solution. Each case of the model was run until the spray saturated.

The Volume of Fluid to Discrete Phase Model (VOF-to-DPM) is an innovative model from Fluent that allowed us to resolve sea spray down to 100 μm of radius through dynamic mesh adaption. We set interaction with the continuous phase, unsteady particle tracking, secondary breakup, and track with fluid flow time-step within this model. We injected particles at a very high start and stop time as a placeholder for particles created using the VOF-to-DPM transition. The particle material was set to pure liquid water. The VOF model allows for

multiphase modeling, we set two phases (air and water) with explicit formulation and sharp/dispersed interface modeling, which are recommended in Fluent when modeling multiphase environments. Explicit formulation accurately calculates curvature and is therefore crucial when modeling surface tension. Waves with a 0.005 m height and 0.05 m length were set up using the open channel flow and open channel wave feature of this model. These settings allow open channel flow with inertia and gravity currents within the domain and waves to be modeled using wave theories. For our purposes, Fifth Order Stokes wave theory was used as it fit the waves set up in the model. Fifth Order Stokes theory uses Fenton's (1985) expansion term kH/2. Zhang et al. (2016) also used the open channel flow, but with second-order Stokes waves to study their wave tank experiments. Of course, the small domain size limits wave properties and does not account for fetch as it would exist in the ocean. The phase interactions were set to a constant surface tension, depending on whether surfactants were introduced, or the water was clean. A sensitivity experiment was conducted to test various surface tension reductions in the CFD model. The spray generation increased with increasing surfactant reduction; the 50% reduction produced the highest amount of spray, with 25%, 10%, and 0% each producing less consecutively. Figure 17 shows the results from these trials plotted together taken from the model at 0.175 s.

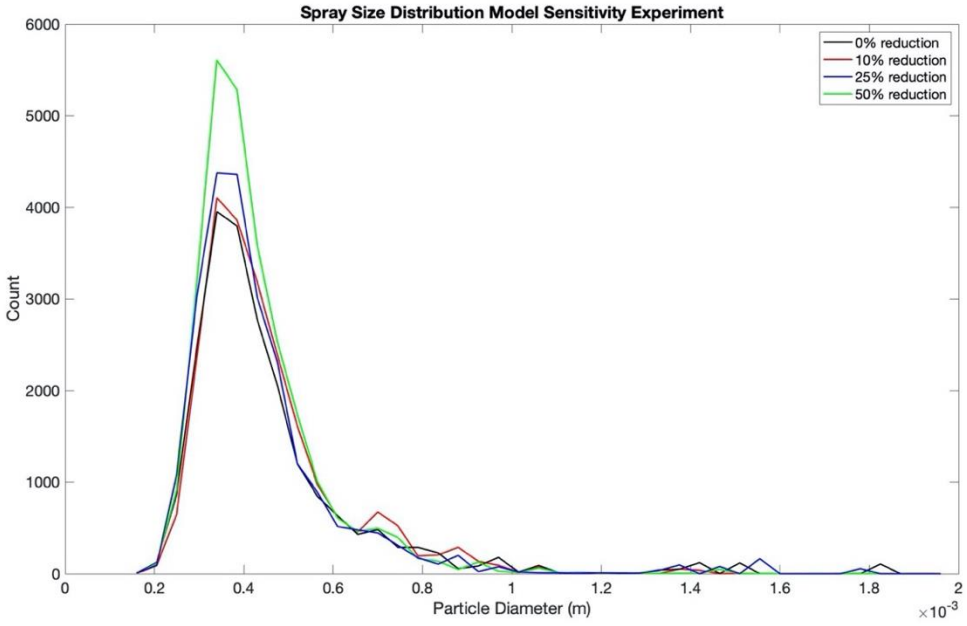

Figure 17. Sensitivity experiment of the VOF-to-DPM model using 50%, 25%, 10% and 0% reductions of surface tension.

Figures 18-21 show the individual results from each trial (without surfactants) with confidence intervals.

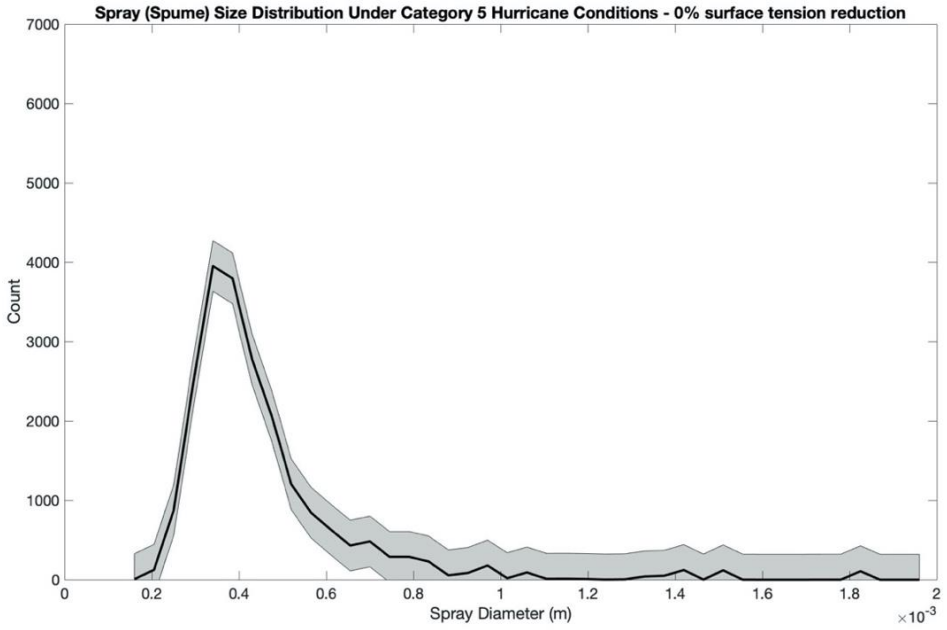

Figure 18. CFD model spray distribution with a 0% surface tension reduction.

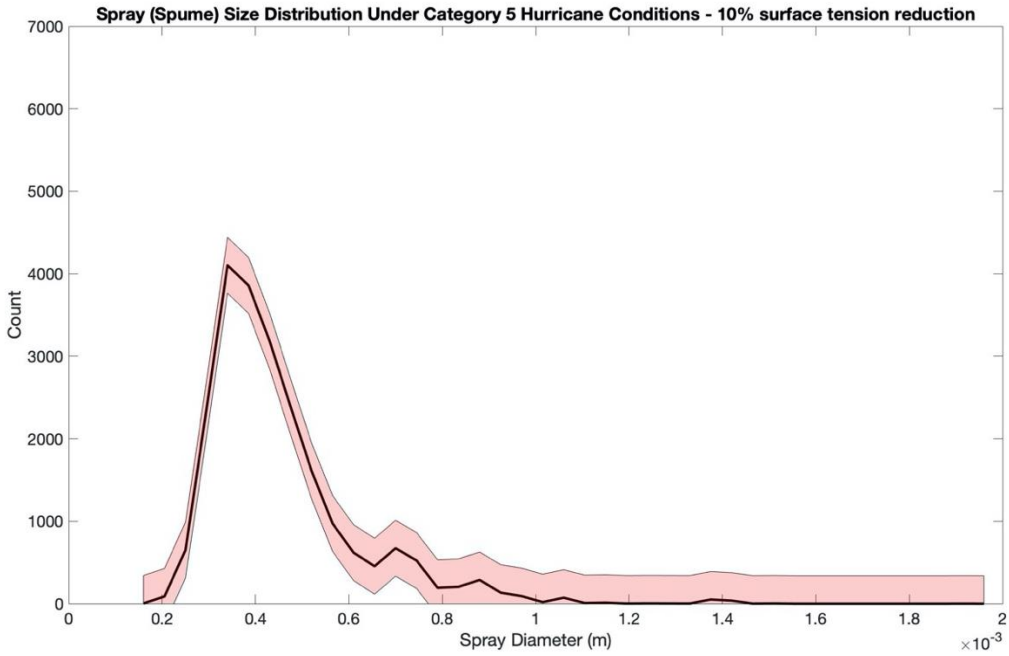

Figure 19. CFD model spray distribution with a 10% surface tension reduction.

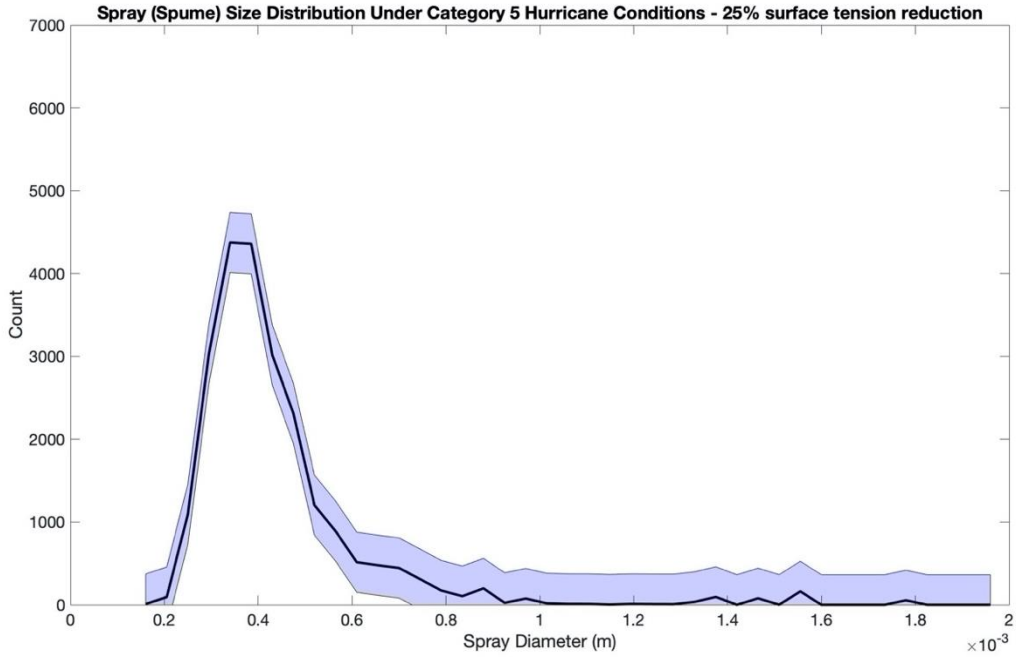

Figure 20. CFD model spray distribution with a 25% surface tension reduction.

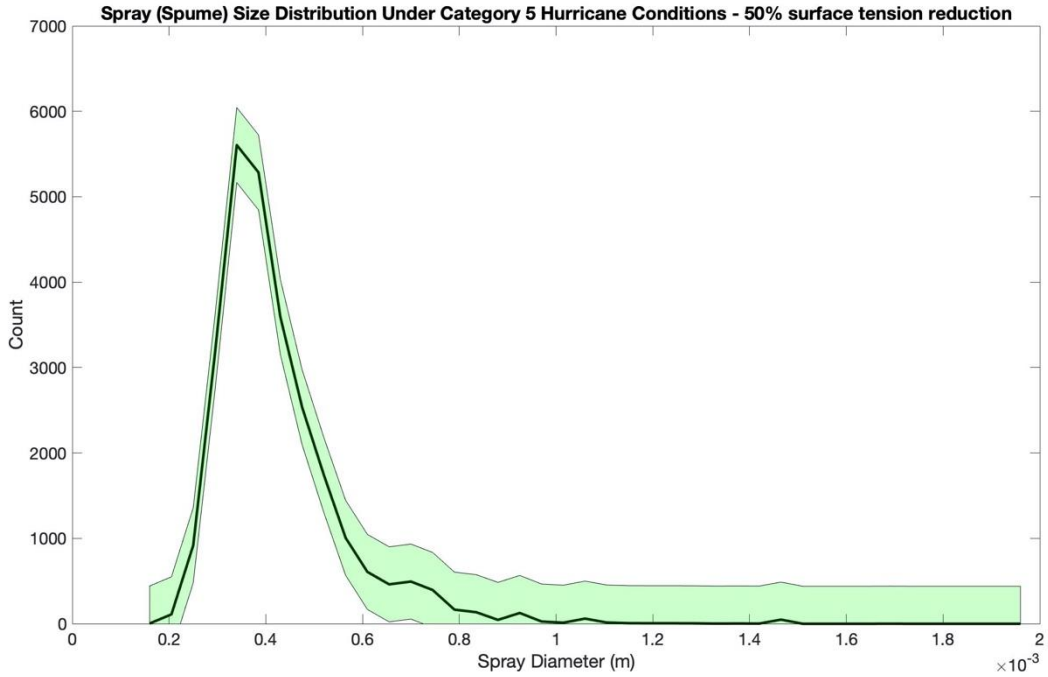

Figure 21. CFD model spray distribution with a 50% surface tension reduction.

One problem in evaluating the effect of surfactants on tropical cyclones is that the abundance of surfactants in the ocean is virtually unknown on a global scale. It is, however, well known that a small amount of surfactant can cover a large surface area (Alpers & Espedal, 2004). King et al. (2019) reported surface tension measurements in the coastal North Sea in the presence of surfactants in the range from 0.053 N/m to 0.0681 N/m. Based on these measurements and our sensitivity experiment, we set the surface tension reduction caused by surfactants to 0.054 N/m (25% reduction) compared to the surface tension of clean water 0.072 N/m (0% reduction). It is important to note the assumption here that there is a constant supply and concentration across the entire sea surface of surfactants, as the sea surface tension is a constant value throughout the model.

The phase model transitions were set to transfer water parcels tracked by VOF to Lagrangian particles set by DPM. This transition was specified to allow parcels that were within the volume-equivalent sphere diameter range of 0 to 0.005 m and upper limits of asphericity as calculated by the radius standard deviation of 0.5 and radius surface orthogonality of 0.5. Lumps that exceeded cell volume by a factor of 10 were split into parcels. To add nonspherical particles, another transition mechanism was set with different settings of asphericity: radius standard deviation of 1 and radius surface orthogonality of 1. The volume-equivalent sphere diameter range was set to of 0 to 1 m for the nonspherical particles. These settings will influence the generated spray but were set as recommended by researchers at ANSYS Fluent. DPM particles are tracked with the primary phase (air) and are not affected by the air-water interface. While they are an important factor to tropical cyclone intensity, evaporation and heat fluxes of spray are not included in this model. The mesh was coarsened immediately after lump conversion to save computational power. Mesh adaption is key to the transition process (Fig. 22). Mesh adaption was set based on the curvature of the volume fraction of water within each mesh cell. It was applied to coarsen and refine every two time-steps, up to 10 levels per cell in the x, y, and z direction. When lumps are converted to DPM particles, the mesh coarsens to the original mesh size. According to Eggers (1997), the timescale for breakup of free surface flows is on the order of 10^{-2} s. The time step in the ANSYS Fluent model was in the range of 10^{-9} to 10^{-6} s, which is several orders of magnitude less than the timescale for breakup of free surface flows. This is more than enough to capture any fast transients during the interface breakup.

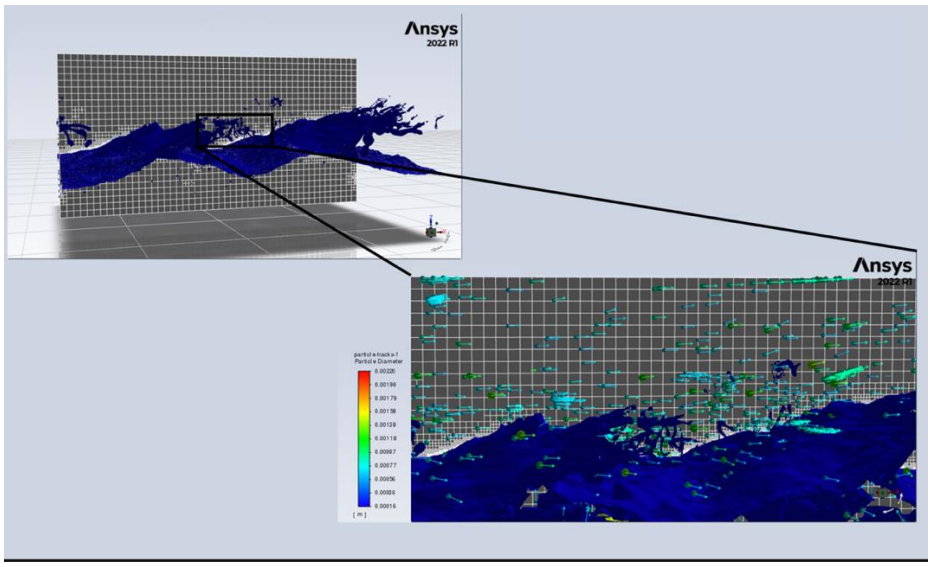

Figure 22. Dynamic remeshing at the air-sea interface in ANSYS Fluent.

This approach dramatically reduces the initial mesh size, which in turn allows for a larger domain (*ANSYS Fluent Theory Guide 2022R1*, 2022). Because the VOF-to-DPM is a new implementation by Fluent, there are no previous ocean applications of this model in the literature. I have closely collaborated with researchers at ANSYS to select the proper settings for this simulation.

4.1.c. Data analysis

Images from the University of Miami laboratory experiment were processed using the *Dantec Dynamics* shadow imaging software package to remove some background noise and focus on the spray droplets taken during the experiment. The software calculates the mean light intensity of each set of 250 images and then normalizes each image based on the mean image to remove background noise, increase contrast, and make particle detection easier. The images were then analyzed using MATLAB to determine how many pixels each spray droplet image is in the x and y direction. The average diameter can be calculated for each spray droplet (1 pixel = 42 μm) to determine the size distribution (in terms of radius). *Dantec Dynamics* software was also used for further image analysis. Data from other available wave tank experiments will also be used to compare to the numerical results. Numerical data can be exported from ANSYS Fluent as data files manually, depending on the parameters being specifically used. Spray information including position, time of generation, volume, and diameter are automatically written in a lump

injection file during the model runs. Data files containing CFD model spray diameters and laboratory experiment spray diameters will be analyzed in MATLAB using histograms, plots, and normalization to calculate spray radius probability distributions. For model verification, probability distribution plots can be created in MATLAB from laboratory data. Heat and momentum fluxes and gas exchange can be calculated both directly in fluent as well as verified by hand calculations in MATLAB.

4.1.d. Satellite imagery

Analysis of color satellite images included coupling the satellite images taken from NASA Aqua MODIS and NOAA VIIRS from the NOAA ERDDAP database online and comparing with data from Weather Underground to comprehensively analyze chlorophyll concentration before, during, and after the passage of various tropical cyclones.

The NASA Aqua satellite carries six instruments and was launched in 2002. Initially, the mission was planned for a six-year lifespan, but it is currently still collecting data from five of the original six instruments (AIRS, AMSU, CERES, MODIS, and AMSR-E). The sixth instrument, HSB, stopped collecting data in 2003. Currently, NASA expects Aqua to continue operations into the 2020s, as there are no current system issues (Graham, 2019). Using MODIS, the satellites can collect data on the chlorophyll-a concentration (in mg m^{-3}) in the near-surface waters of the ocean. This is accomplished using an empirical relationship derived from in situ chlorophyll-a measurements and blue-to-green band ratios from reflectance of remote sensors (Maccherone, 2018).

The Visible Infrared Imaging Radiometer Suite (VIIRS), located onboard the Suomi NPP and NOAA-20 satellites, is a crucial data collection instrument. VIIRS uses visible and infrared imagery to collect data from land, and in the atmosphere, cryosphere, and oceans. VIIRS covers wavelengths from 0.41 to 12.5 microns using 22 imaging and radiometric bands (Bai, 2019).

Satellite data were collected for the specific coordinates of the tropical cyclone path during the dates of its passage. The hurricane tracks were then drawn in Google Maps according to maximum wind speed and category and exported as an xml file. They were then imported to Google Earth and analyzed with the corresponding satellite data to emphasize and reveal any correlation between higher chlorophyll concentration and intensity of the storm. Future

considerations should include considering storm radii when choosing the resolution of chlorophyll satellite data.

4.2. Results and Discussion

The previous work this proposal continues from (Vanderplow, 2020) demonstrated, for the first time, the increase of the sea spray generation and change in size distribution under tropical cyclone conditions in the presence of surfactants using a CFD model confirmed with laboratory experiments that resolved spray size distributions starting from a 100-μm radius (Fig. 23). As surfactants increase spray generation and change the size distribution, they influence heat and momentum fluxes to the atmosphere, potentially affecting tropical cyclone intensity.

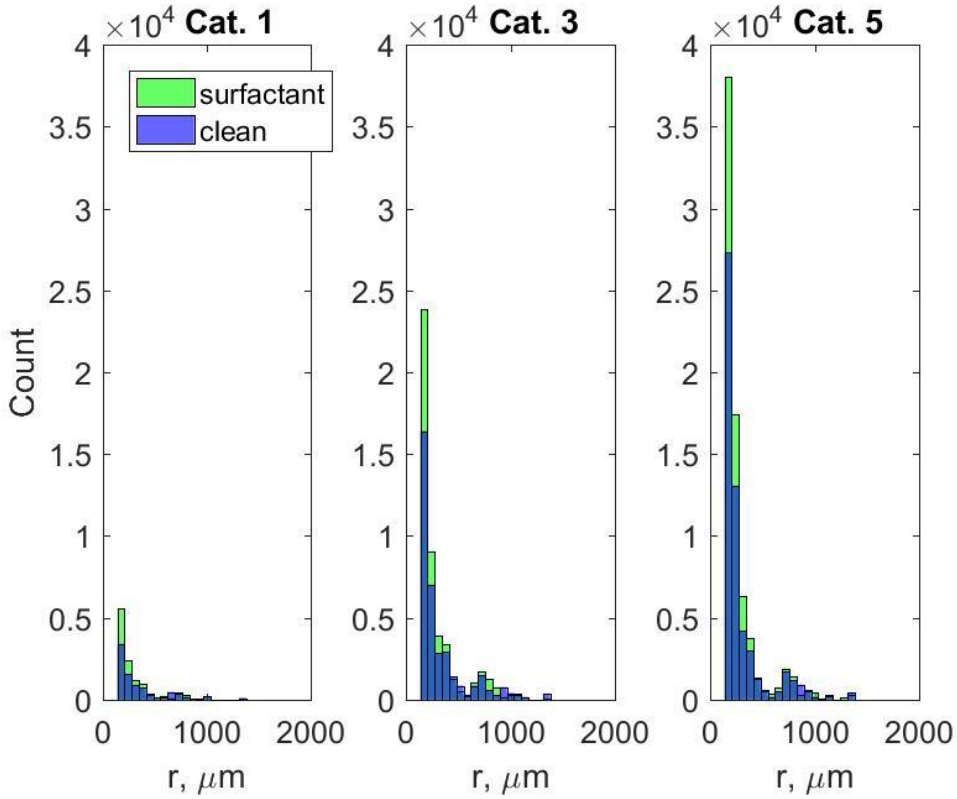

Figure 23. Spray radius distributions for Category 1 (4 Nm-2), 3 (10 Nm-2), and 5 (20 Nm-2) tropical cyclone conditions in the VOF-to-DPM model. Scales below 100 mm are not completely resolved and have been removed from graphs (Vanderplow 2020).

As a continuation of the previous work, additional models have been run to yield results from the entire spectrum of tropical cyclone conditions. The models from the previous work for

Category 1, 3, and 5 tropical cyclone conditions were also run longer to completely saturate in spray generation. Expanding the results from Vanderplow (2020), I was also able to plot the spray distributions from the model results to give a better idea of how the spray particles were distributed above the sea surface. This was done for both spherical and nonspherical spray, which will be shown for each tropical cyclone condition run in Figures 24, 26, 28, 30, 32, 34, 36, 38, 40, 42, and 44. Spray spatial distribution was also visualized in 3D and colored by their diameter for all models, shown in Figures 25, 26, 29, 31, 33, 35, 37, 39, 41, 43, and 45. Models for tropical storm force winds (0.5 Nm wind stress) without (Figs. 24 and 26) and with surfactants (Figs. (25 and 27), which resulted in little spray development.

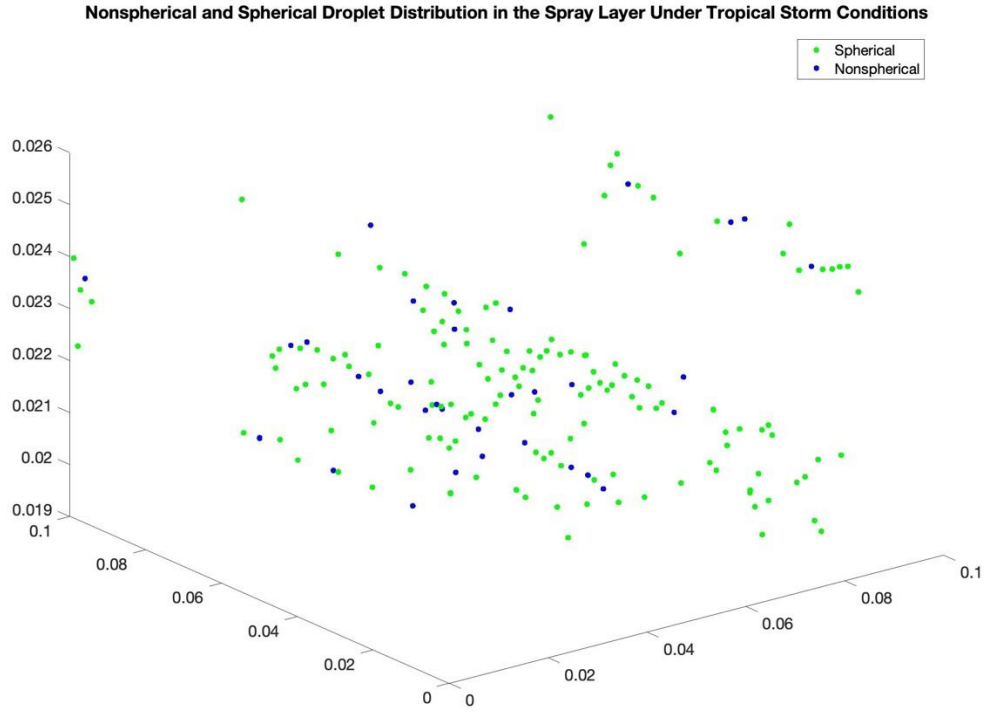

Figure 24. Spray layer distribution of spherical and nonspherical droplets under tropical storm conditions.

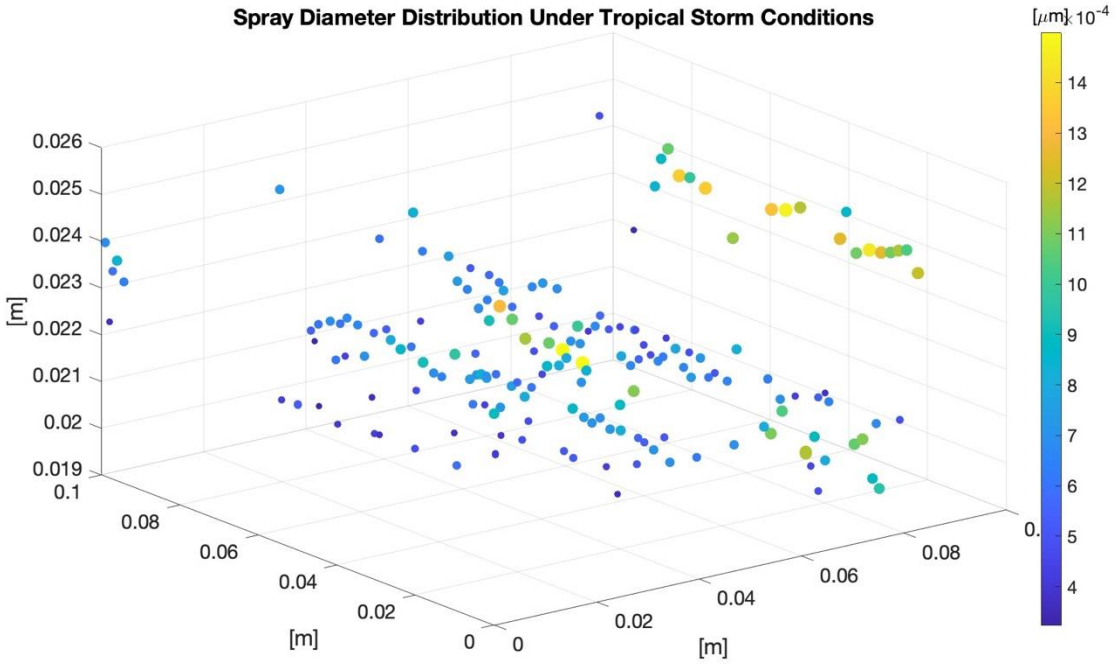

Figure 25. Spray layer distribution showing droplets colored by their diameter under tropical storm conditions.

When surfactants were present, the size distribution remained relatively similar to the case when surfactants were not present (Figs. 25 and 27). Under these lower winds, there were a significantly higher amount of spherical spray for both the surfactant and nonsurfactant cases (Figs. 24 and 26).

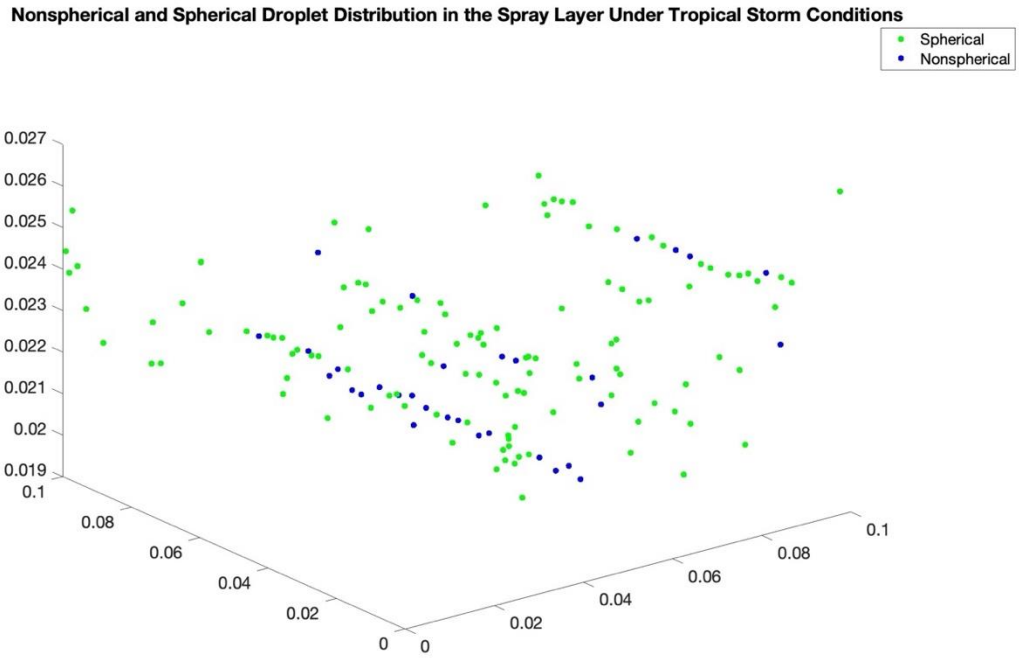

Figure 26. Surfactant spray layer spherical and nonspherical spray droplet spatial distribution under tropical storm conditions.

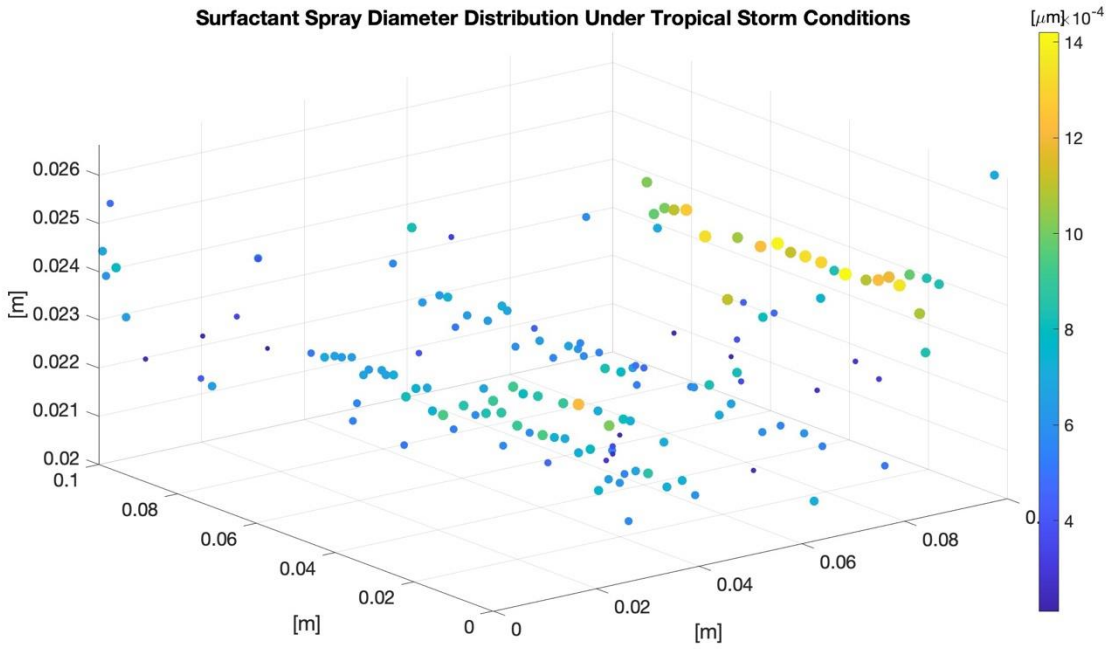

Figure 27. Surfactant spray layer distribution showing droplets colored by their diameter under tropical storm conditions.

Displaying the spray in this way can help us to better understand spray layer dynamics and implications for heat, momentum, and gas fluxes. Nonspherical spray are more likely to partake in secondary breakup, leading to a further increase in spray concentration as well as more smaller particles. This also has implications for air-sea fluxes, which is discussed in sections 5 and 7. After a flow time of 0.412 seconds, the Category 1 model saturated and generated a spray layer 0.0325 m thick. As seen in Figure 28, there is significantly more spherical spray droplets than nonspherical droplets. The same spray droplets were also plotted in 3D space according to their diameter (Fig. 29).

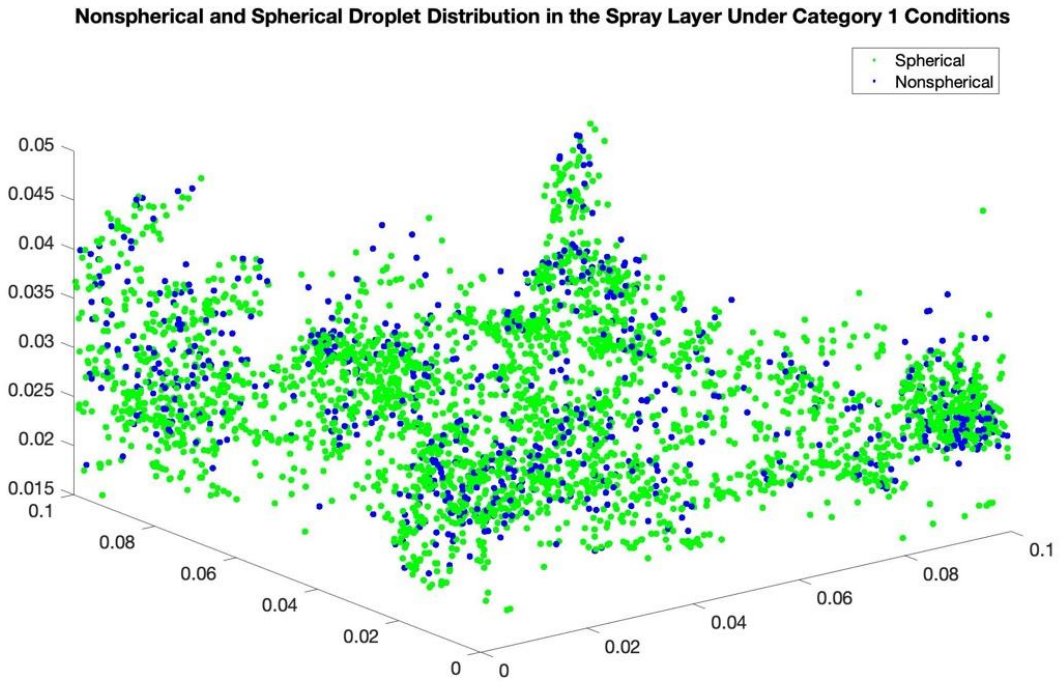

Figure 28. Spray layer distribution of spherical and nonspherical droplets under Category 1 tropical cyclone conditions.

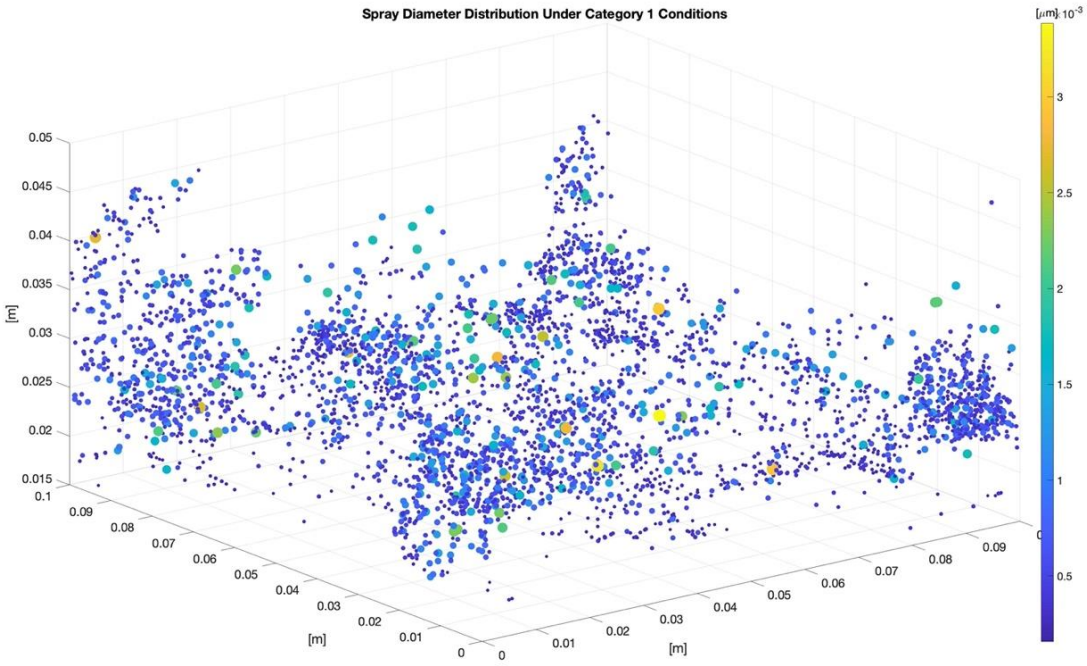

Figure 29. Spray layer droplet diameter under Category 1 tropical cyclone conditions.

When surfactants were present, the model ran to a flow time of 0.373 seconds before saturating. Qualitatively, the amount of spherical and nonspherical spray seems more comparable when surfactants are present, indicating an increase in nonspherical particles, as expected (Fig. 30). When visualized by their diameter (Fig. 31), we can see that the spray particles increase as compared to the case without surfactants, and that there appears to be a shift to smaller spray particles, as was seen in Vanderplow (2020). The spray layer with surfactants was 0.0263 m thick, which was slightly smaller than the case without surfactants.

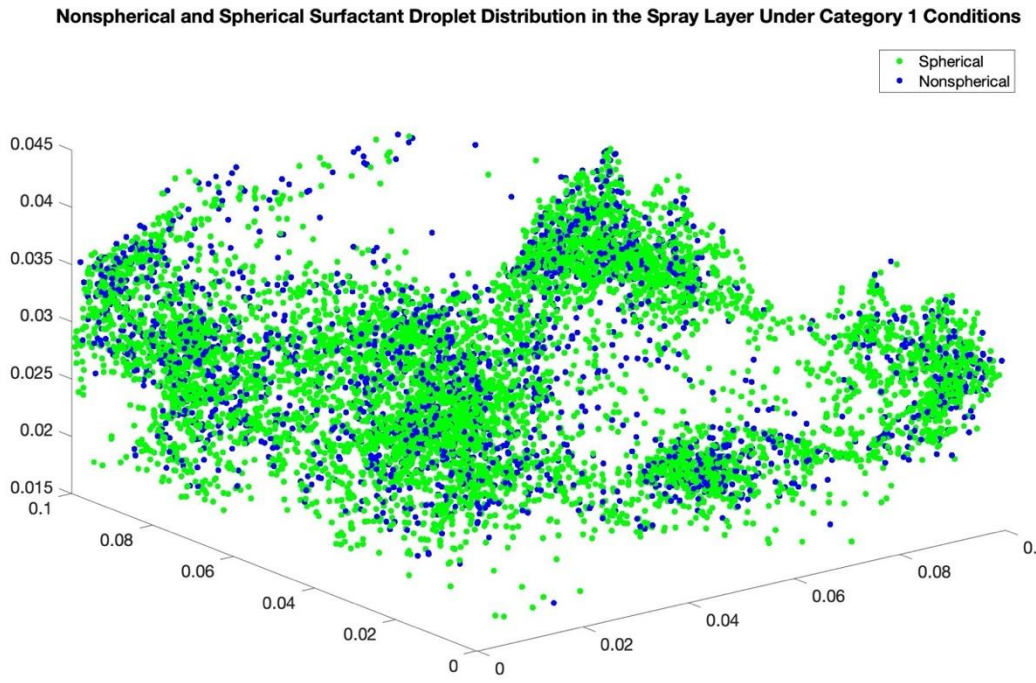

Figure 30. Surfactant spray layer distribution of spherical and nonspherical droplets under Category 1 tropical cyclone conditions.

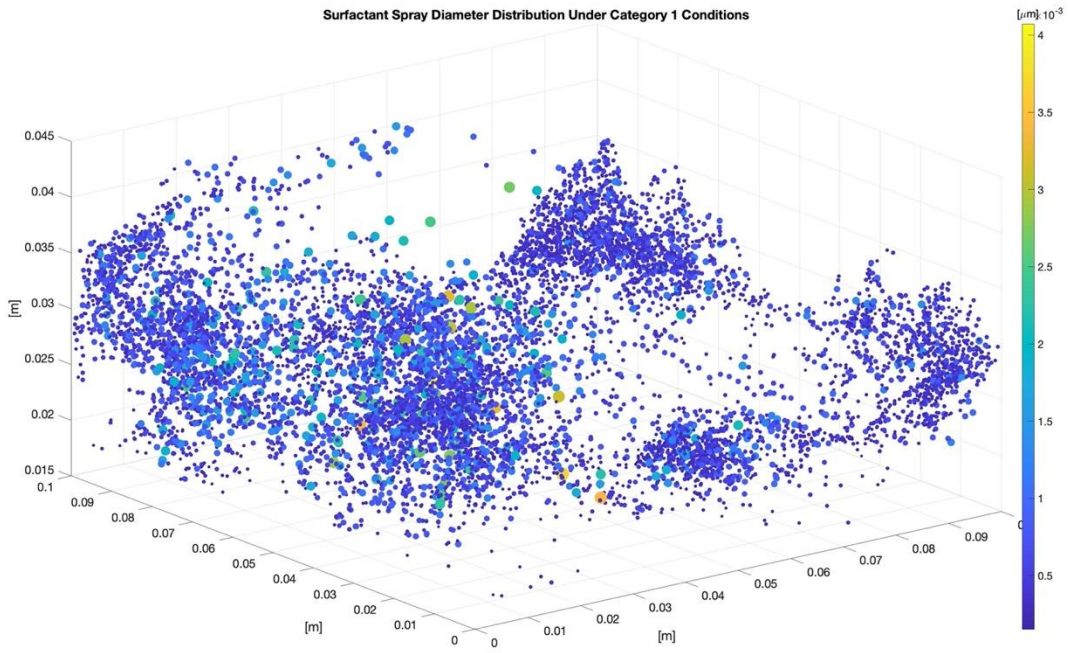

Figure 31. Surfactant spray layer droplet diameter under Category 1 tropical cyclone conditions.

After a flow time of 0.332 seconds, the Category 2 model saturated and displayed a spray layer 0.0388 m thick. The spray layer being thicker than the Category 1 model makes sense, as more spray is generated with increasing wind speed. It also ran for less time before saturation for this reason. As seen in Figure 32, the comparison between nonspherical and spherical droplets is more comparable than in the Category 1 model, but still shows the same trend of having more spherical particles. When we look at the particles colored by their diameter (Fig. 33), we can see a significant increase in spray concentration compared to Category 1 conditions.

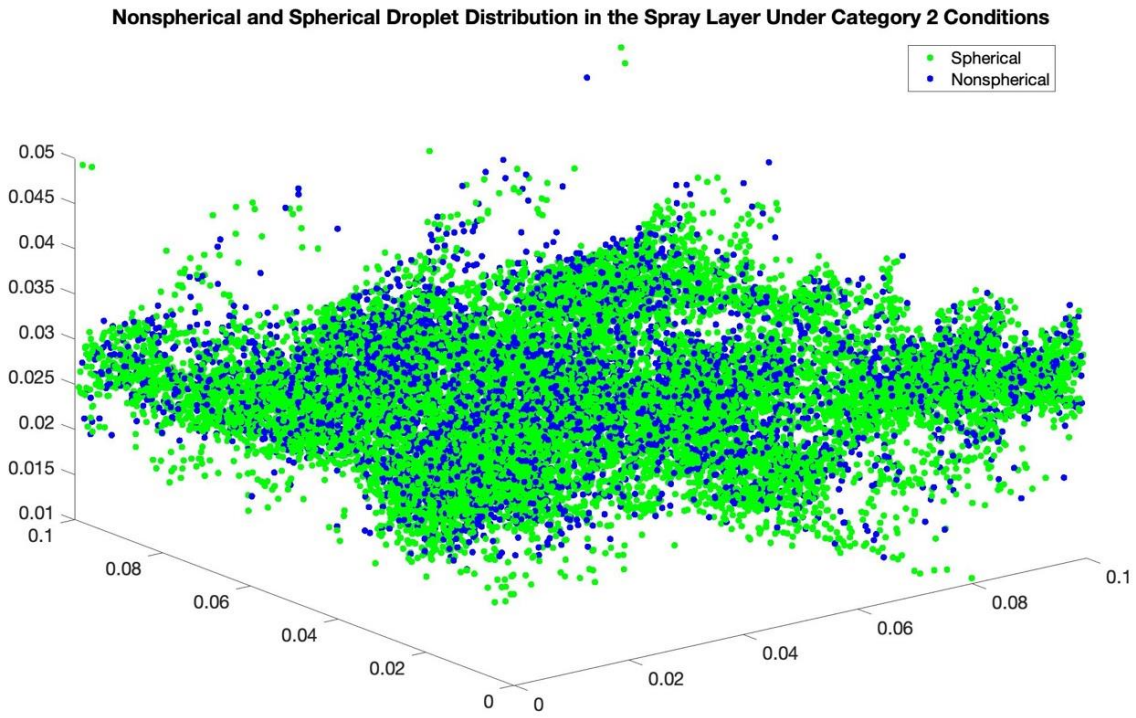

Figure 32. Spray layer distribution of spherical and nonspherical droplets under Category 2 tropical cyclone conditions.

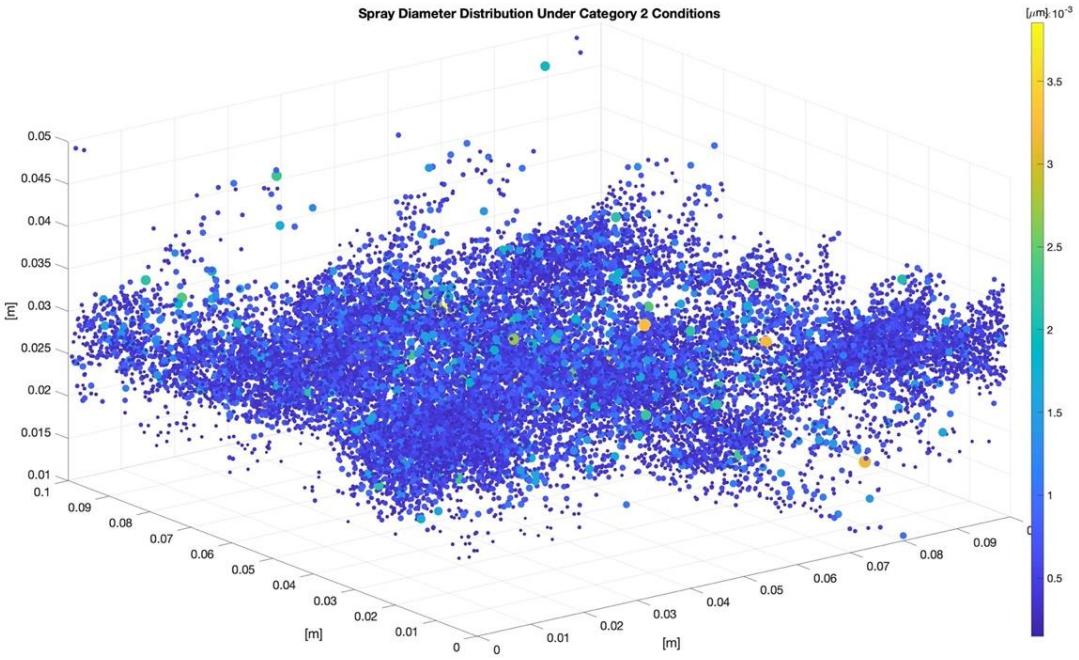

Figure 33. Spray layer droplet diameter under Category 2 tropical cyclone conditions.

In the presence of surfactants, the Category 2 model ran for a flow 0.334 seconds and saturated with a spray layer thickness of 0.0345 m. The spray layer was slightly thinner than the model without surfactants. This appears to be due to more grouping of the spray droplets as seen in Figures 34 and 35.

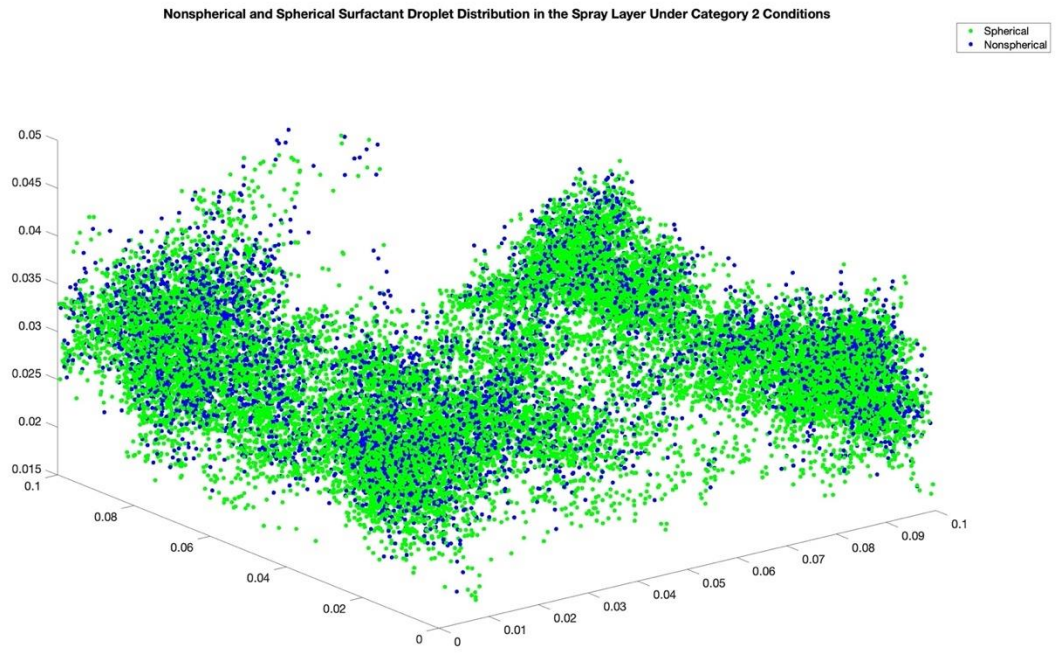

Figure 34. Surfactant spray layer distribution of spherical and nonspherical droplets under Category 2 tropical cyclone conditions.

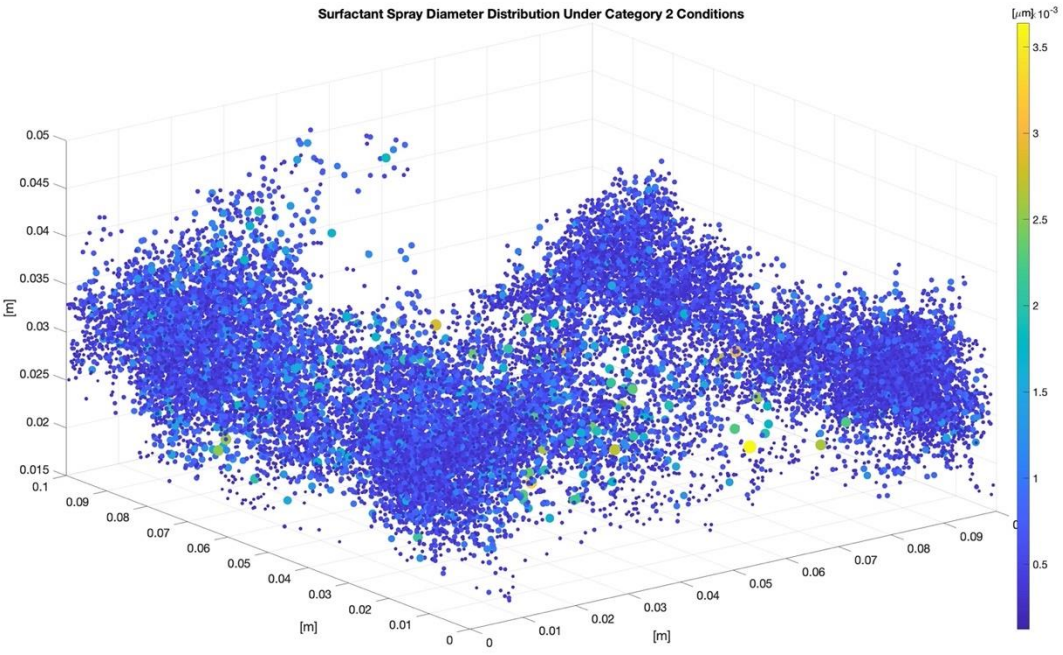

Figure 35. Surfactant spray layer droplet diameter under Category 2 tropical cyclone conditions.

After a flow time of 0.233 seconds, the Category 3 model saturated and displayed a spray layer 0.0328 m thick. As wind increases, the flow time decreases since more particles are generated and the model saturates faster, as expected. The spray layer thickness is comparable to Category 2 and did not increase. As seen in Figure 36, the comparison between nonspherical and spherical droplets is similar to that of than in the Category 2 model. When we look at the particles colored by their diameter (Fig. 37), we can see a grouping of the spray particles near the wave crests, which was not seen in the Category 1 conditions but was seen in Category 2 surfactant conditions. This may have contributed to the lack of increase in spray layer thickness compared to the Category 2 model.

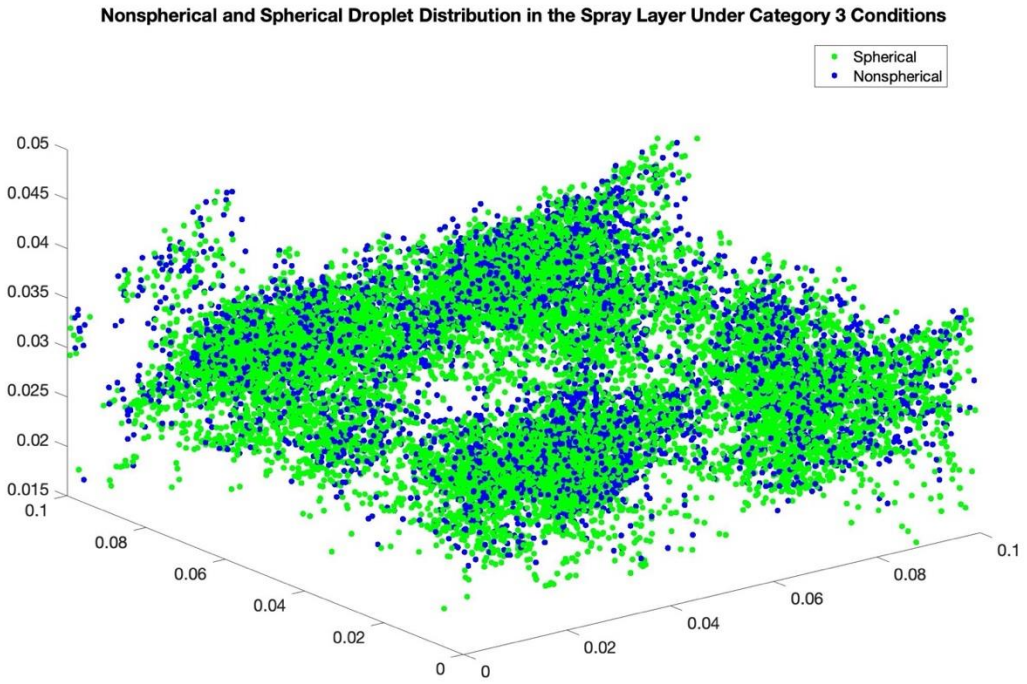

Figure 36. Spray layer distribution of spherical and nonspherical droplets under Category 3 tropical cyclone conditions.

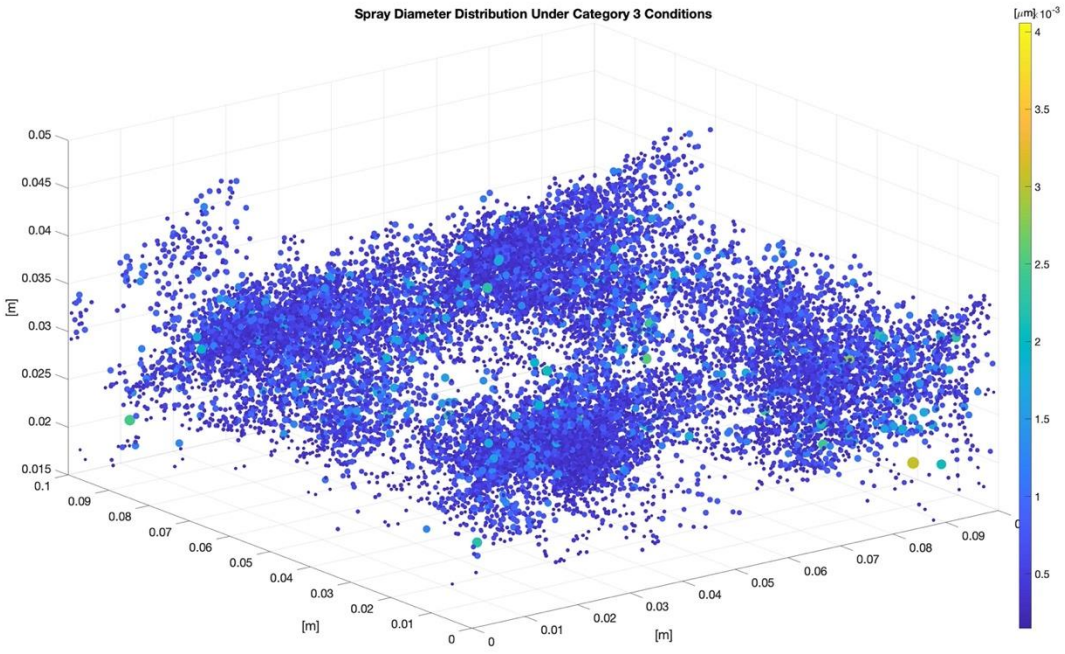

Figure 37. Spray layer droplet diameter under Category 3 tropical cyclone conditions.

When surfactants were present, the Category 3 model ran to a flow time of 0.318 seconds before saturating. Qualitatively, the amount of spherical and nonspherical spray seems comparable when surfactants are present to when they are not (Figs. 38 and 40). When visualized by their diameter (Fig. 39), we can see that the spray particles increase as compared to the case without surfactants (Fig. 37), and that there appears to be a shift to smaller spray particles, as was seen in Vanderplow (2020). We see the same grouping tendency that was seen in the Category 3 model without surfactants. The spray layer with surfactants was 0.0345 m thick, which was slightly larger than the case without surfactants, likely due to increase spray generation and a shift to smaller spray particles, which will reach higher in the air layer.

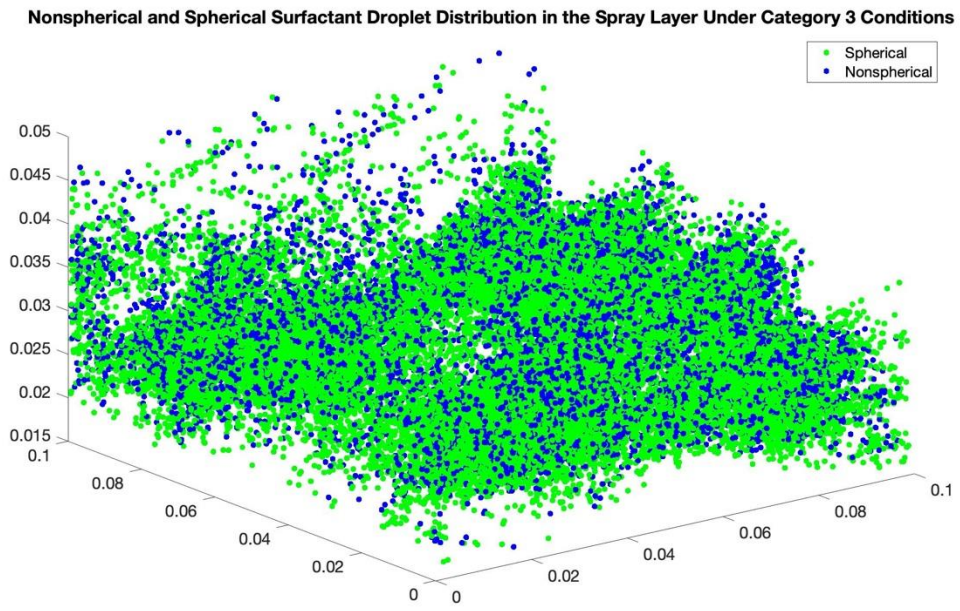

Figure 38. Surfactant spray layer distribution of spherical and nonspherical droplets under Category 3 tropical cyclone conditions.

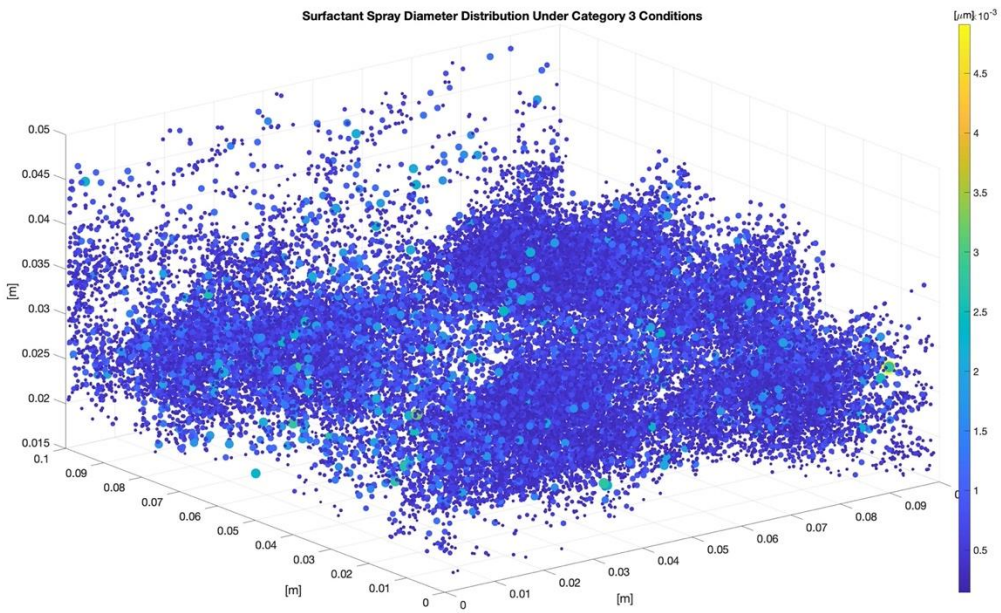

Figure 39. Surfactant spray layer droplet diameter under Category 3 tropical cyclone conditions.

After a flow time of 0.227 seconds, the Category 4 model saturated and displayed a spray layer 0.0377 m thick. Once again, the flow time decreased as more particles were generated with

wind speed, and the spray layer became thicker than the Category 3 model, but not as thick as the Category 2 model. As seen in Figure 40, the nonspherical and spherical droplets are comparable in concentration. When we look at the particles colored by their diameter (Fig. 41), we can see an increase in spray concentration compared to Category 1-3 conditions, and interestingly a lack of the grouping trend seen in Category 3 conditions and instead a pattern of grouping towards the center of the domain.

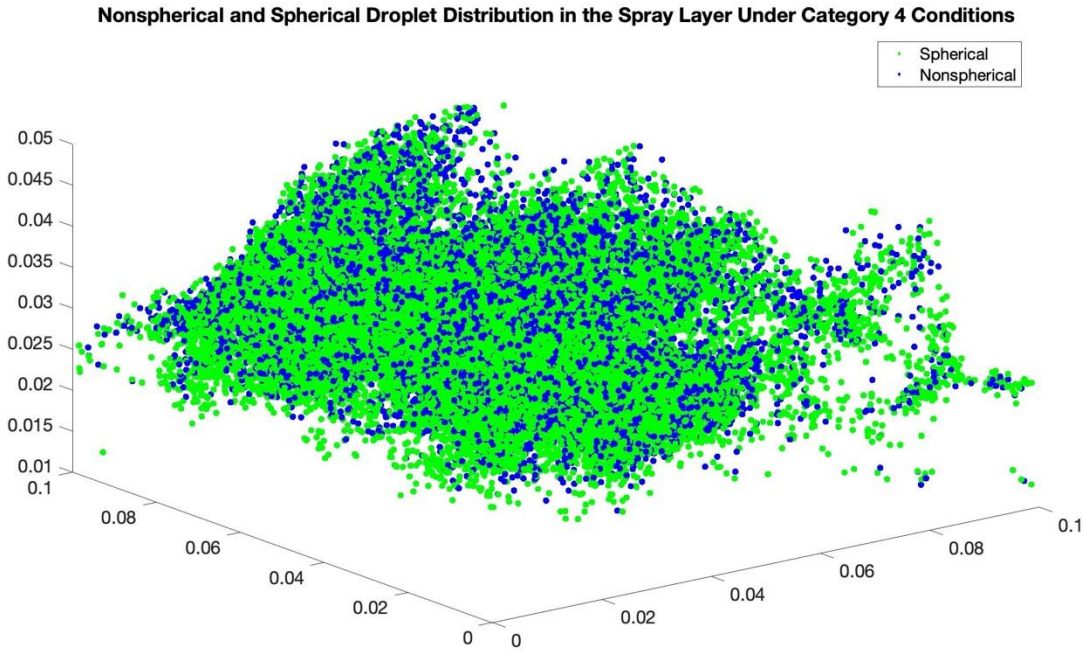

Figure 40. Spray layer distribution of spherical and nonspherical droplets under Category 4 tropical cyclone conditions.

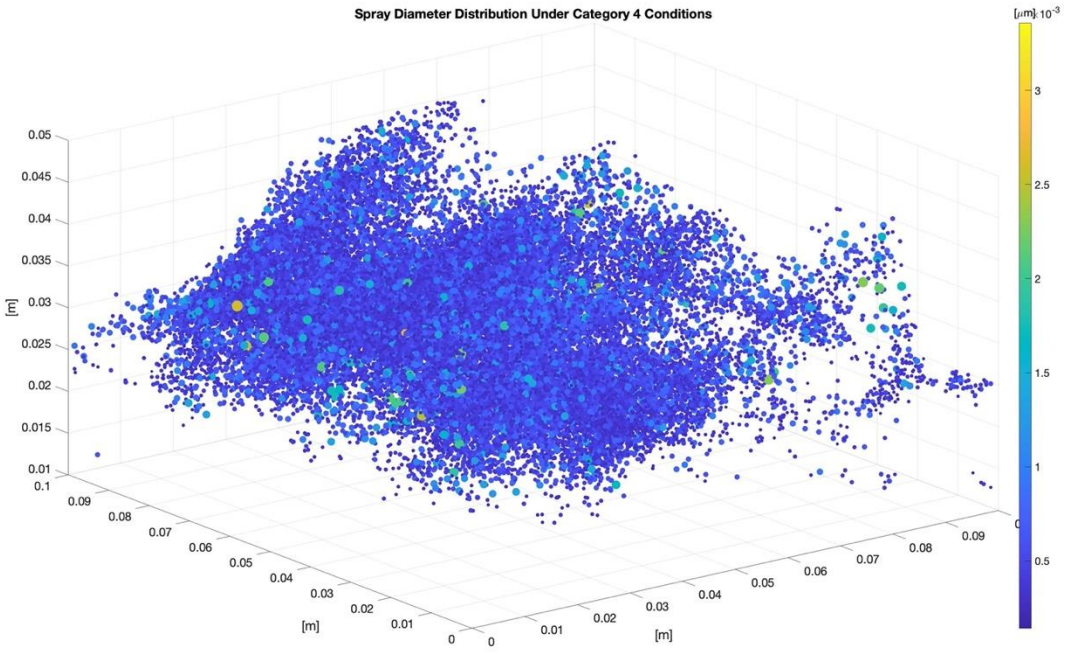

Figure 41. Spray layer droplet diameter under Category 4 tropical cyclone conditions.

The Category 4 surfactant model ran to a flow time of 0.255 seconds before saturating, which was slightly longer than the nonsurfactant case, but still shorter than the Category 3 surfactant case, as expected. Qualitatively, the amount of spherical and nonspherical spray seems comparable when surfactants are present to when they are not (Fig. 42). When visualized by their diameter (Fig. 43), we can see that the spray particles increase once again as compared to the case without surfactants, and that there appears to be a shift to smaller spray particles, as well as more large spume particles, which could be caused by higher winds and more nonspherical spray susceptible to secondary breakup. The spray layer with surfactants was 0.0385 m thick, which was slightly larger than the case without surfactants, likely due to increase spray generation and a shift to smaller spray particles, which reach higher in the air layer.

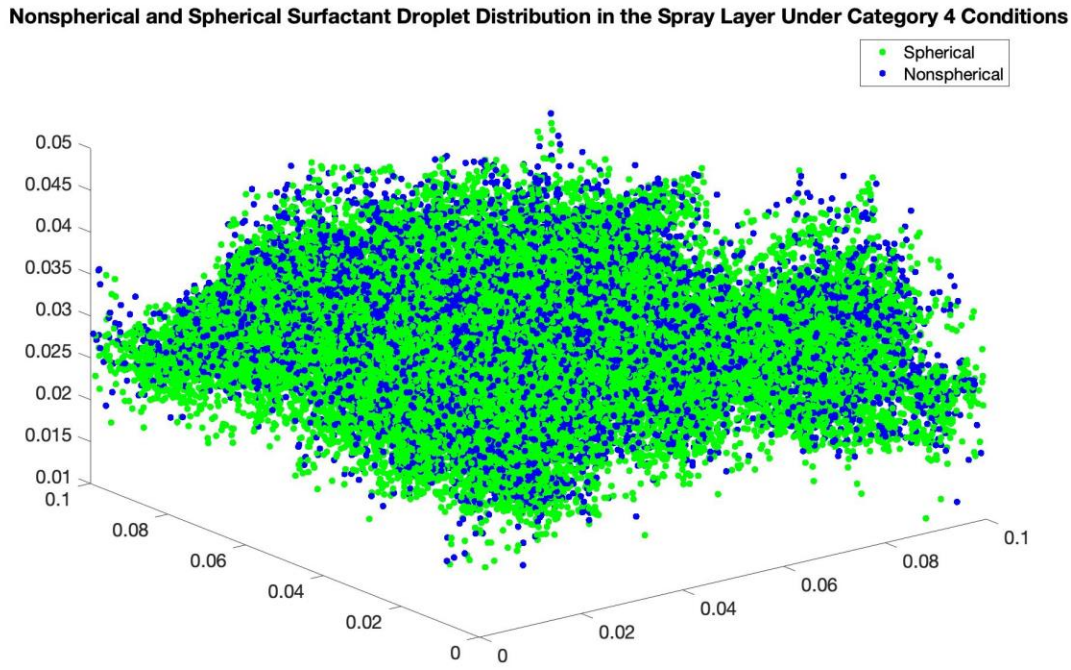

Figure 42. Surfactant spray layer distribution of spherical and nonspherical droplets under Category 4 tropical cyclone conditions.

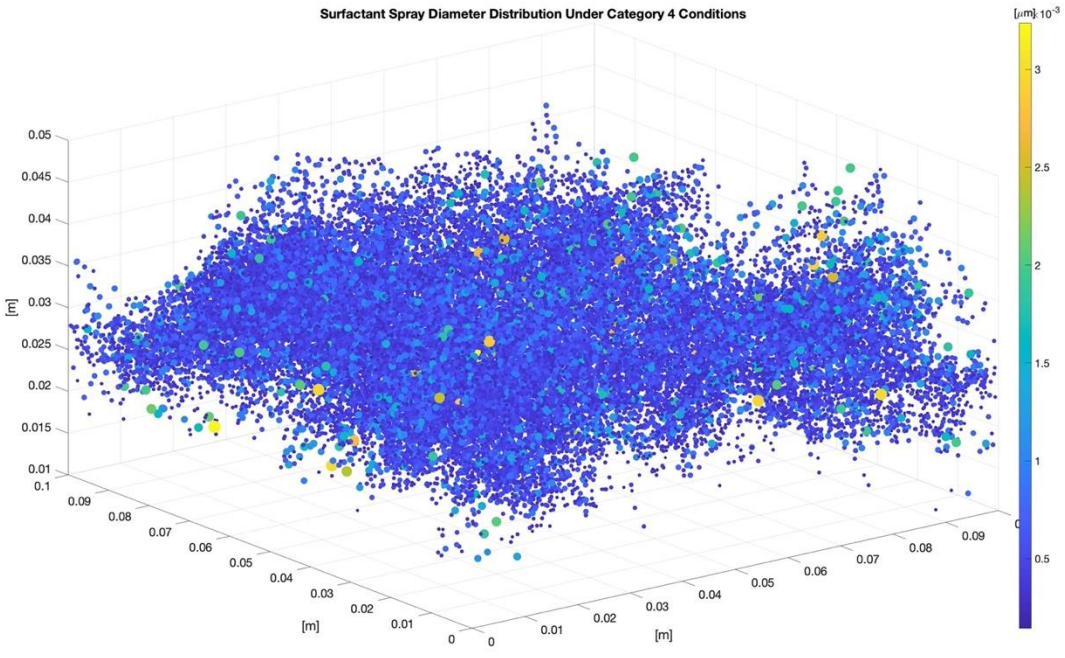

Figure 43. Surfactant spray layer droplet diameter under Category 4 tropical cyclone conditions.

After a flow time of 0.191 seconds, the Category 5 model saturated and displayed a spray layer 0.0332 m thick. This was the shortest flow time of the nonsurfactant models, as expected. The comparison between nonspherical and spherical droplets (Fig. 44) shows more spherical than nonspheical particles. Figure 45 shows the particles colored by their diameter, where it is honestly difficult to see a dramatic increase in spray generation compared to the nonsurfactant Category 4 case.

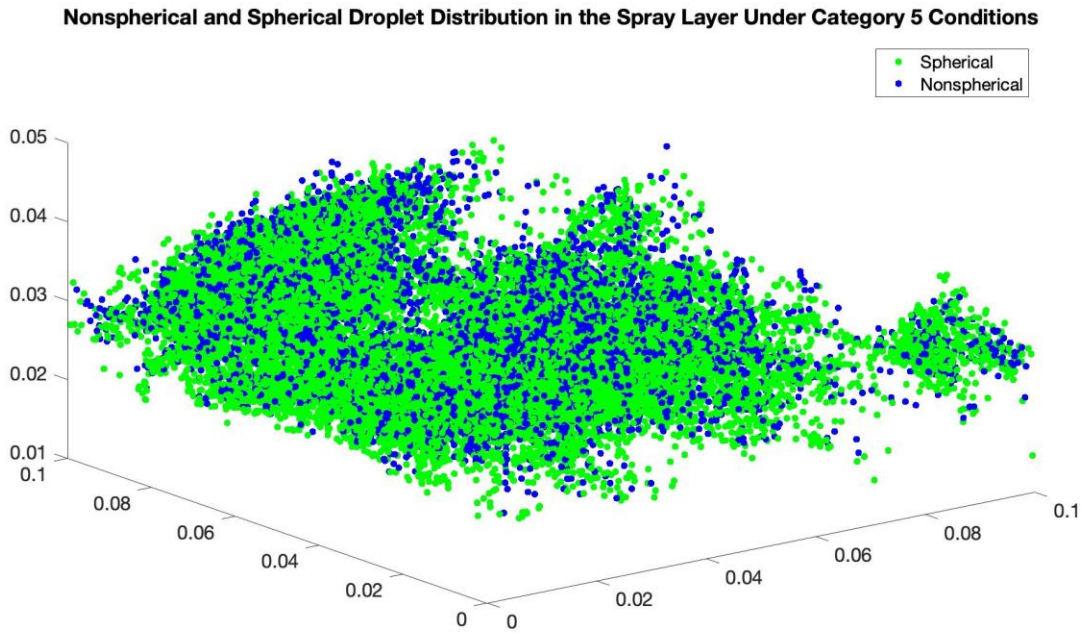

Figure 44. Spray layer distribution of spherical and nonspherical droplets under Category 5 tropical cyclone conditions.

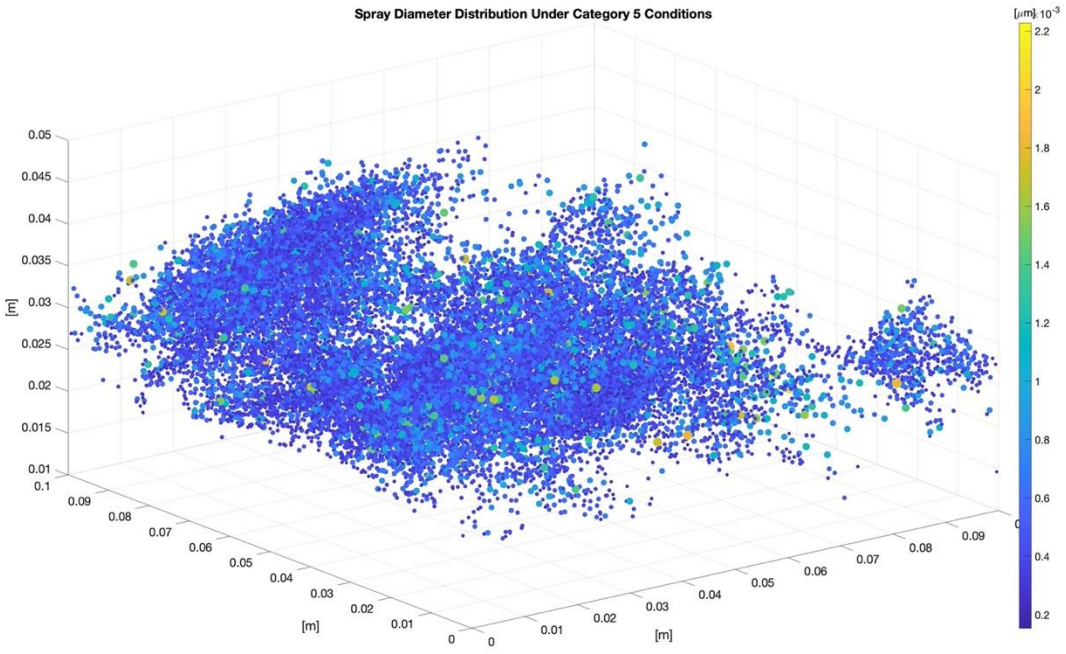

Figure 45. Spray layer droplet diameter under Category 5 tropical cyclone conditions.

The Category 5 surfactant model ran for 0.212 seconds before saturating, which was slightly longer than the nonsurfactant case, but still shorter than the Category 4 surfactant case, as expected. Qualitatively, the amount of spherical and nonspherical spray seems comparable to the nonsurfactant case (Fig. 46). When visualized by their diameter, shown in Figure 47, we can see that the spray particles increase dramatically as compared to the case without surfactants, and that there appears to be a shift to smaller spray particles, as well as more large spume particles, which could be caused by higher winds and more nonspherical spray susceptible to secondary breakup. The spray layer with surfactants was 0.0371 m thick, which was slightly larger than the case without surfactants, likely due to increase spray generation and a shift to smaller spray particles, which reach higher in the air layer.

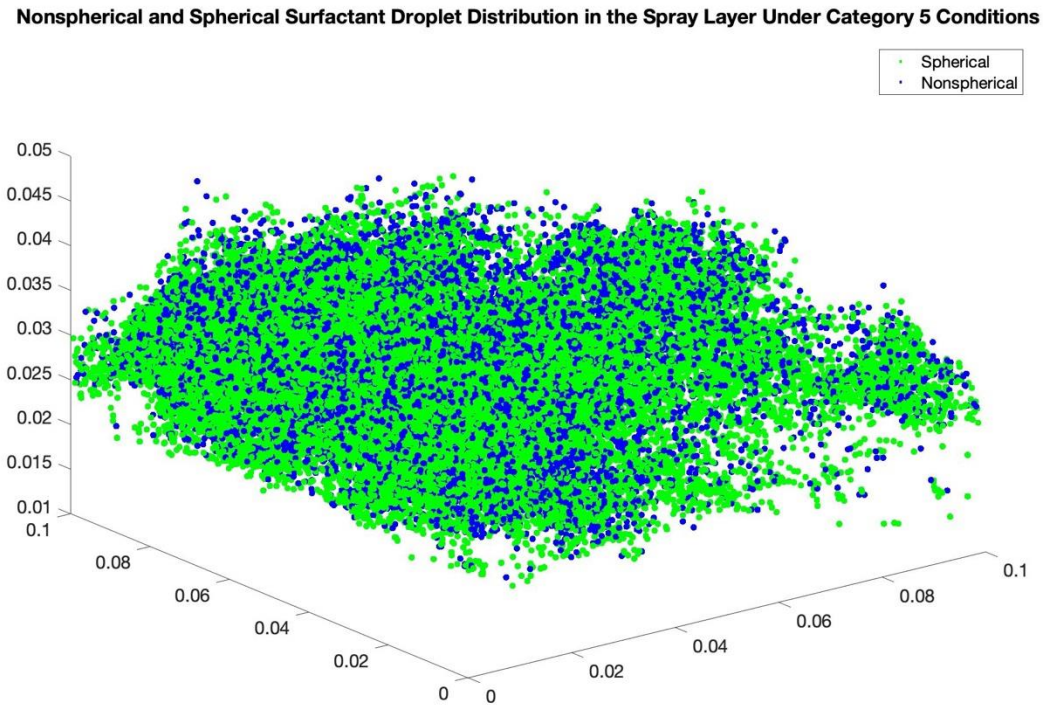

Figure 46. Surfactant spray layer distribution of spherical and nonspherical droplets under Category 5 tropical cyclone conditions.

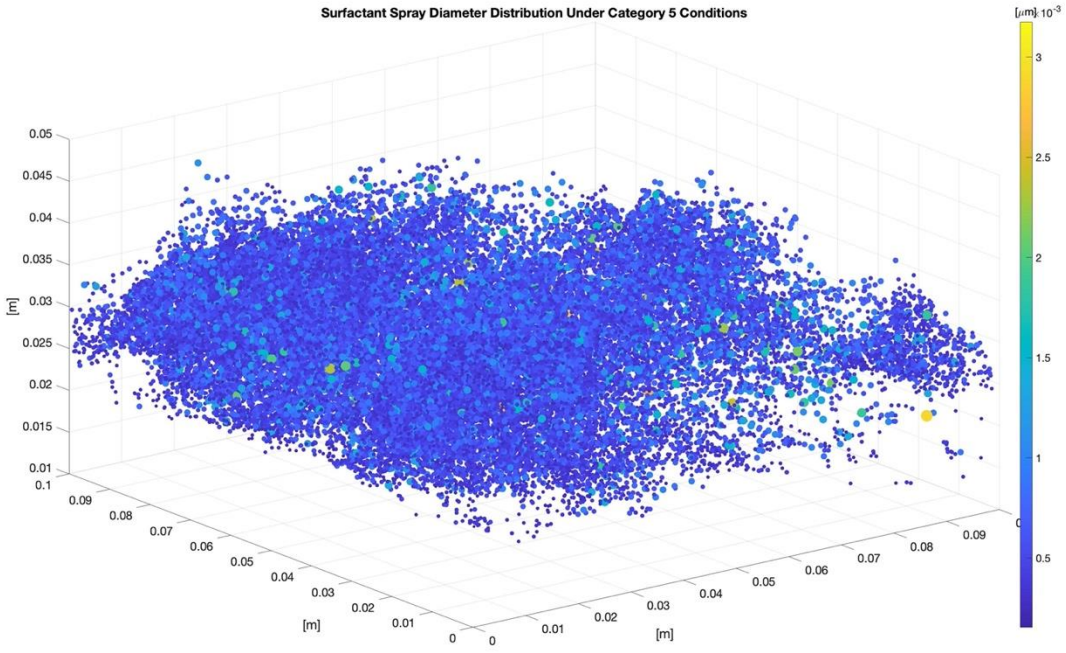

Figure 47. Surfactant spray layer droplet diameter under Category 5 tropical cyclone conditions.

The results from analyzing spherical and nonspherical spray for each category storm is shown in Table 1. Surprisingly, results did not follow the initial hypothesis based on previous literature for all cases. Since surfactants reduce surface tension, there should be more nonspherical spray since this change results in a less structured droplet surface. From the VOF-to-DPM model, category 3 and 4 results were slightly less nonspherical particles when surfactants were present than in regular conditions.

Table 1. Percent nonspherical particles from each tropical cyclone category model

Category	Nonsurfactant	Surfactant
1	18.3%	22.2%
2	25.5%	25.2%
3	26.7%	26.3%
4	28.5%	27.4%
5	27.2%	29.2%

4.2.a. Satellite imagery: primary productivity as a proxy for surfactants

The color satellite imagery analysis using chlorophyll as an indicator of primary productivity focuses mainly on qualitative comparison but shows that there are potential applications in this direction for color satellite oceanography. While various satellite imagery is often used to collect data on tropical cyclones, conventional satellites are limited by cloud cover. C-band SAR is an exception to this, as it can penetrate cloud cover while maintaining high resolution (Friedman & Li, 2000; Katsaros et al., 2002). Zhang and Perrie (2012) specifically used a C-band Cross-Polarization Ocean (C- 2PO) model to observe tropical cyclones from space. The presence of surfactants and rainstorms could be identified from dualpolarimetric SAR imagery using the co-polarized phase difference filter (Wahl et al., 1996; Lu et al., 1999; 2000; Gade & Alpers, 1999, Migliaccio et al., 2009; Soloviev et al., 2011; Velotto et al., 2013), which may contribute to better understanding the potential effect of surfactants and rain droplets on the air-sea interface and tropical cyclone intensity and intensification.

Case studies from Ian 2022, Ida 2021, Otis 2023, and Mocha 2023 were analyzed with chlorophyll-a satellite data from NOAA VIIRS. Examples from previous tropical cyclone seasons can be found in Vanderplow (2020). Hurricane Ian 2022 transitioned from a hurricane to

major hurricane within one day before landfall in Cuba. Ian then made a second landfall in southwest Florida and destroying Fort Meyers. Finally, after crossing Florida, Ian made a third landfall in South Carolina bringing major damage to the area. Figure 48 shows Ian's track overlayed with chlorophyll-a data. Near all coasts before landfall, and specifically before the Florida landfall, Ian passed over areas of higher chlorophyll concentration, and therefore likely areas of higher surfactant concentration.

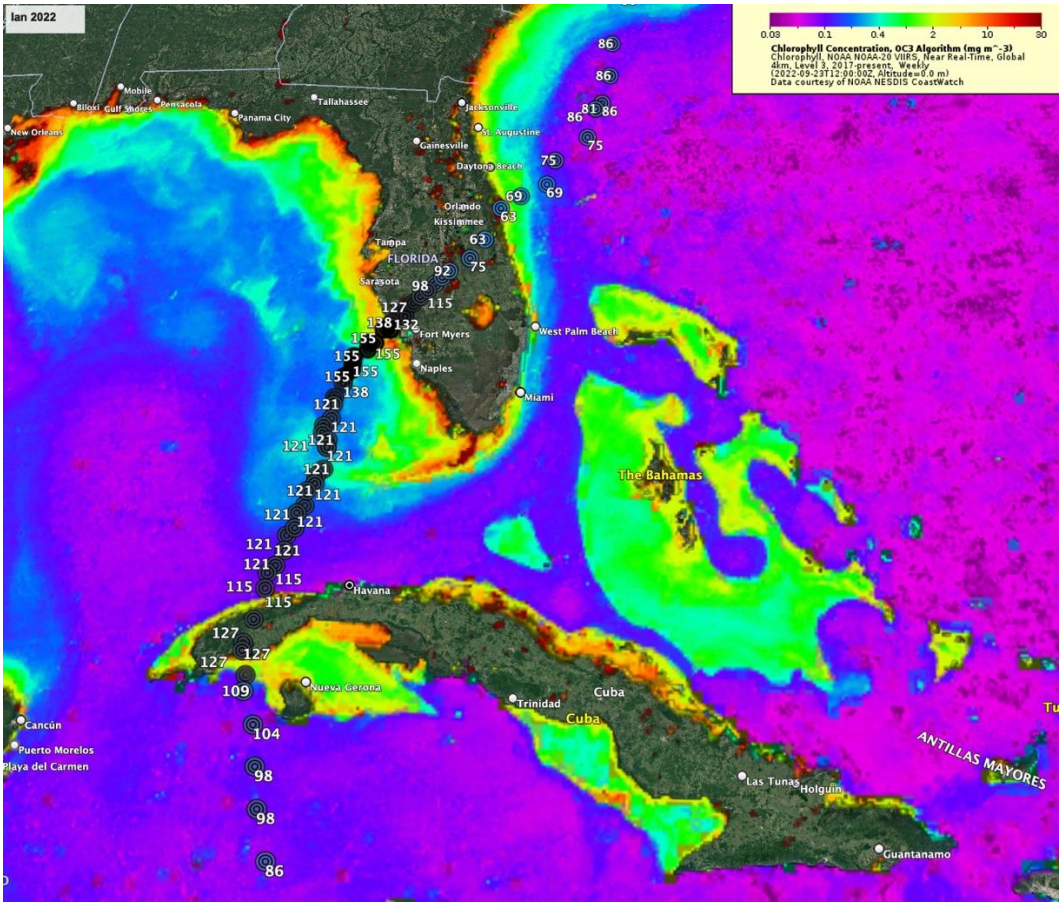

Figure 48. Tropical Cyclone Ian track with wind speed overlaid onto NOAA VIIRS chlorophyll data.

Hurricane Ida (Fig. 49) made two landfalls in Cuba as a Category 1 storm before strengthening over the Gulf of Mexico during two rapid intensification periods. The first period was over central Gulf of Mexico at 115 mph winds, just after passing over the area of ~0.25 mg m^{-3} chlorophyll-a concentration. The second period occurred near the coastline when Ida reached

150 mph winds in the areas of 0.5 – 10 mg m^{-3} chlorophyll-a concentration. Ida brought catastrophic damage to Louisiana.

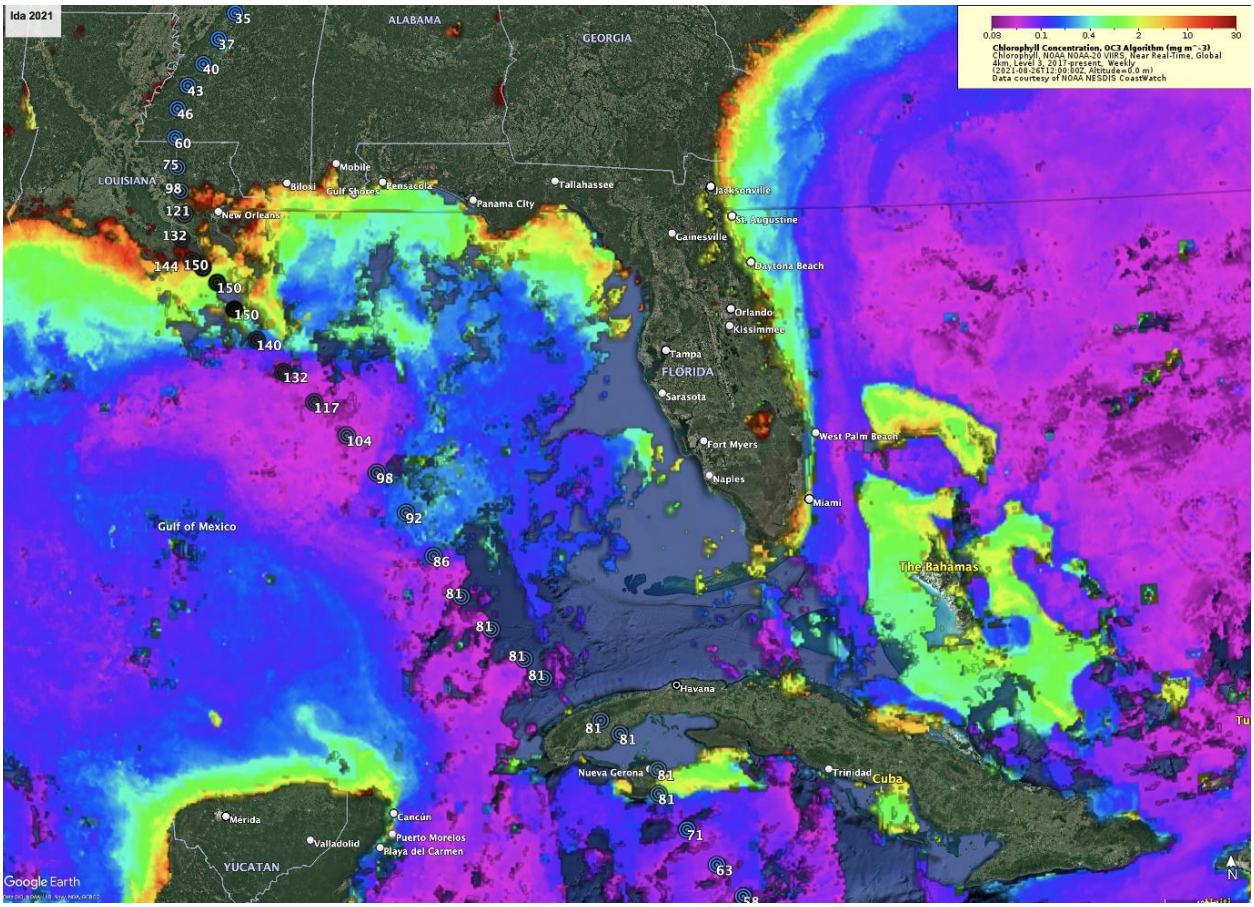

Figure 49. Tropical Cyclone Ida track with wind speed overlaid onto NOAA VIIRS chlorophyll data.

Hurricane Otis (2023) made landfall in Acapulco, Mexico as a Category 5 storm, setting record as the strongest hurricane to make landfall in the Eastern Pacific during the time of satellite imagery. Otis rapidly intensified dramatically, with winds increasing 115 mph within 24 hours. The coastal communities were completely unprepared and suffered immense damage and chaos. While Otis did not pass over any significantly high areas of chlorophyll-a concentration, the vast majority of the waters the storm passed over were above the baseline values of 0.03 mg m^{-3} (Fig. 50).

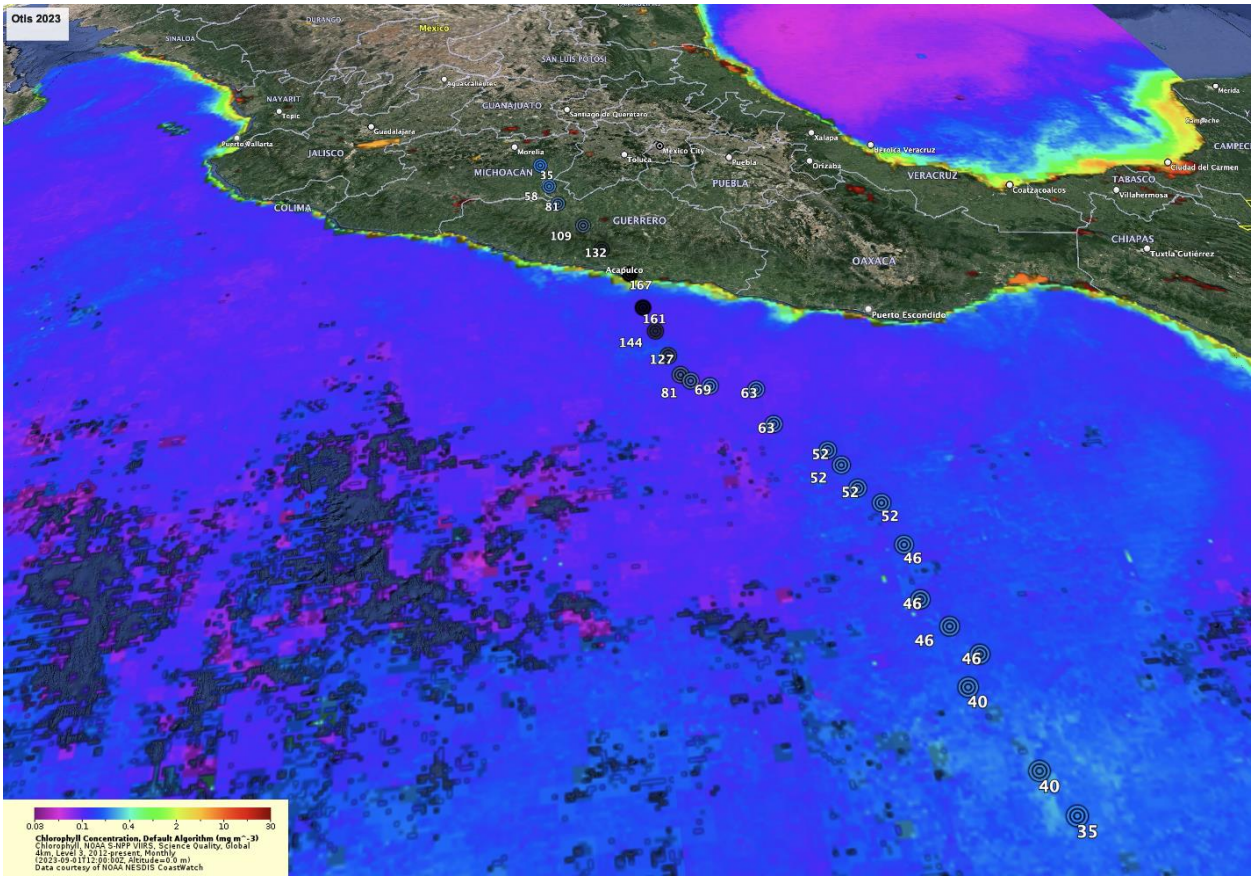

Figure 50. Tropical Cyclone Otis track with wind speed overlaid onto NOAA VIIRS chlorophyll data.

Cyclone Mocha (2023) rapidly intensified to a Category 5 storm in the Bay of Bengal before making landfall in Myanmar and tied with Cyclone Fani as the strongest North Indian Ocean storm on record. Death tolls and storm damage were significant despite some evacuation warnings and preparation. As seen in Figure 51, Mocha passed over multiple areas of increased chlorophyll-a concentration ranging in value from 0.1 to 0.5 mg m^{-3} during rapid intensification periods.

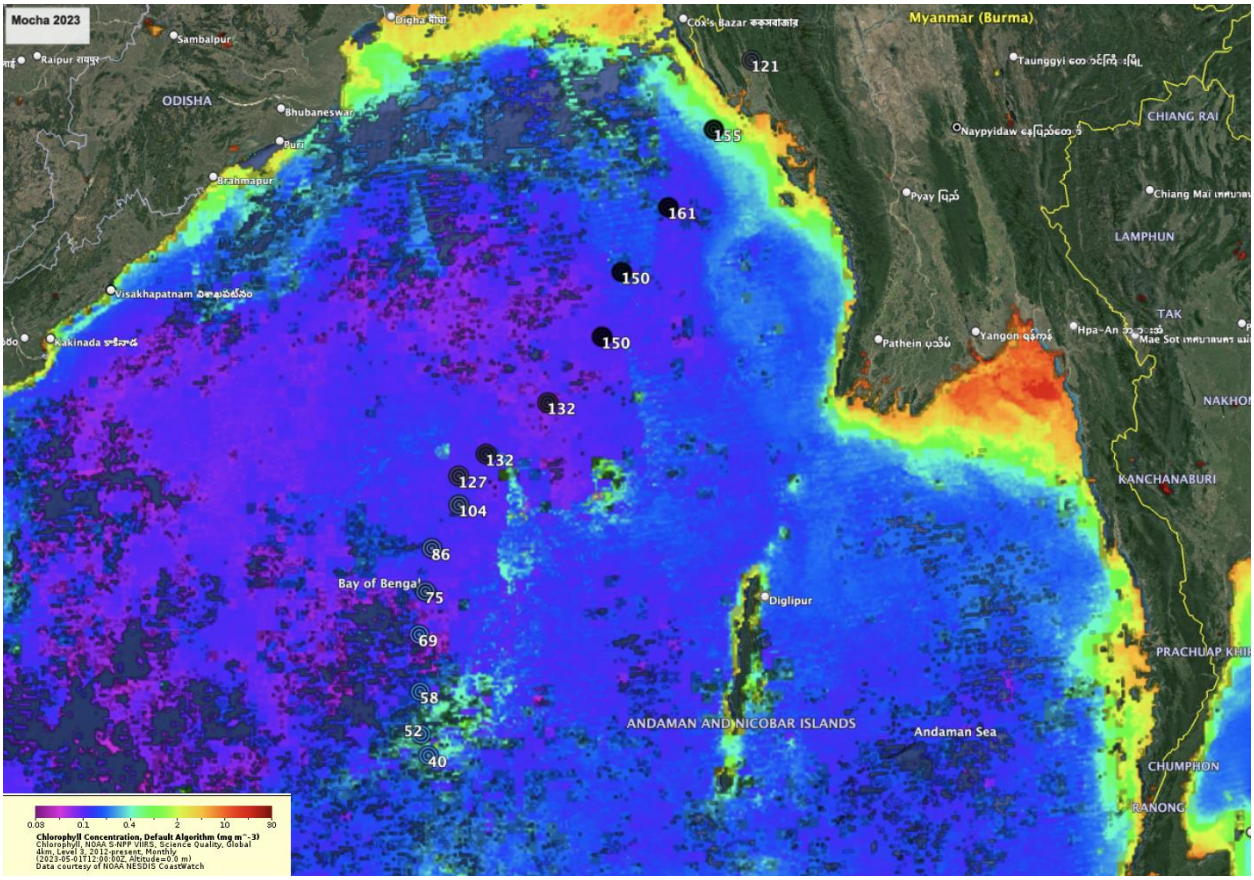

Figure 51. Tropical Cyclone Mocha track with wind speed overlaid onto NOAA VIIRS chlorophyll data.

As seen in the satellite images, primary productivity is higher in coastal areas in all ocean basins. Productivity is higher in coastal waters due to land runoff, which is high in nutrients that trigger production, and due to the shallow continental shelf, that keeps nutrients near the coast and readily available for microorganisms (Webb, 2021). There is likely a higher concentration of surfactants presents in areas of high productivity, and therefore at the coasts. Uning et al. (2018) studied surfactants in coastal areas, finding that in areas with increased runoff and anthropogenic activity, surfactant concentrations in the sea surface microlayer were dramatically higher.

Often, storms rapidly intensify right before landfall. Of course, this could be due to a variety of factors, including warmer coastal waters, decreased drag, and changes in atmospheric parameters such as humidity. An increase in surfactant concentration, which as shown in the previous section of this work and Vanderplow (2020), increases spray generation and shifts spray to smaller radii, could also play a role in coastal rapid intensification of tropical cyclones.

Barr et al. (2023) also found that coastal areas are of critical importance for the role of spray in tropical cyclone intensity. Wave shoaling occurs when surface waves reach shallow waters and slow down and wavelength decreases, while the wave height increases. With changes in wave properties, spray generation will also be altered. Barr et al. (2023) found that their sea state-dependent spray flux differed significantly from the wind-dependent spray flux in coastal areas due to wave shoaling. The enthalpy flux increased over 35% for their case run for Hurricane Michael's landfall.

A complete investigation of the effect of bio-surfactants on the tropical cyclone intensity and intensification is likely not feasible at this point due to the complexity of the problem and scarcity of the field data. The extent of the surfactant effect on tropical cyclones might be qualitatively estimated by correlating the tropical cyclone intensity changes and the presence of chlorophyll identified from color satellite imagery, assuming that primary productivity is favorable for the generation of bio-surfactants. The presence of biosurfactants, as well as anthropogenic surfactants (oil spills and dispersants), can also be identified from dual-polarimetric synthetic aperture radar (SAR) imagery using the co-polarized phase difference filter, which may contribute to a better understanding of the potential effect of surfactants on tropical cyclone intensity and intensification.

5. Heat and momentum fluxes

Another extension of the existing model was planned to implement the evaporation-condensation model within Fluent requires modification through a user-defined function to accurately model sea spray evaporation and heat fluxes. Unfortunately, there was not sufficient time and resources to complete this portion of the planned work, but a discussion of the completed results in application to heat and momentum fluxes will be discussed in this section. The current progress set relative humidity (RH) in the air to 96% and 100% at the sea surface to simulate evaporation as spray separates from the sea surface and interacts with the air (Fig. 52).

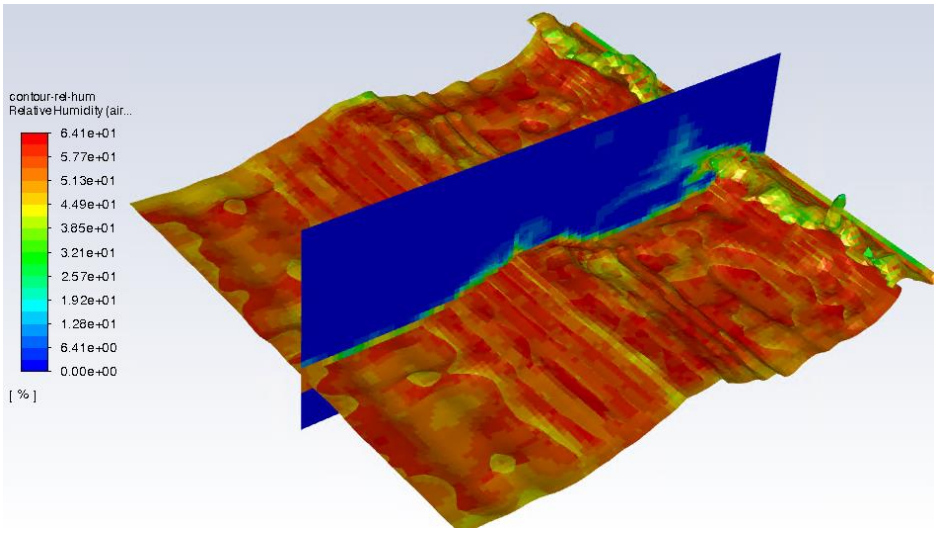

Figure 52. Results from implementing a user-defined function to simulate evaporation at the air-sea interface.

Including evaporation and heat fluxes in the CFD model will greatly increase the understanding of these relationships, which are difficult to observe and measure in the field and laboratory. One goal of this dissertation work was implementing evaporation and heat fluxes into the VOF-to-DPM model. Figures 53 and 54 show contours of enthalpy (air, left and water, right) in our model domain as well as the DPM particles (spray droplets) colored by their temperature and displayed by their diameter size. This upgrade is complex and requires implementation of additional parameters and variables through a user-defined function that the existing evaporation-condensation model does not currently have, which is currently still in work. Improving the air-sea flux implementation in forecast models for enhanced tropical cyclone intensity forecasting is essential to prevent the loss of lives, making the work of this proposed dissertation extremely valuable.

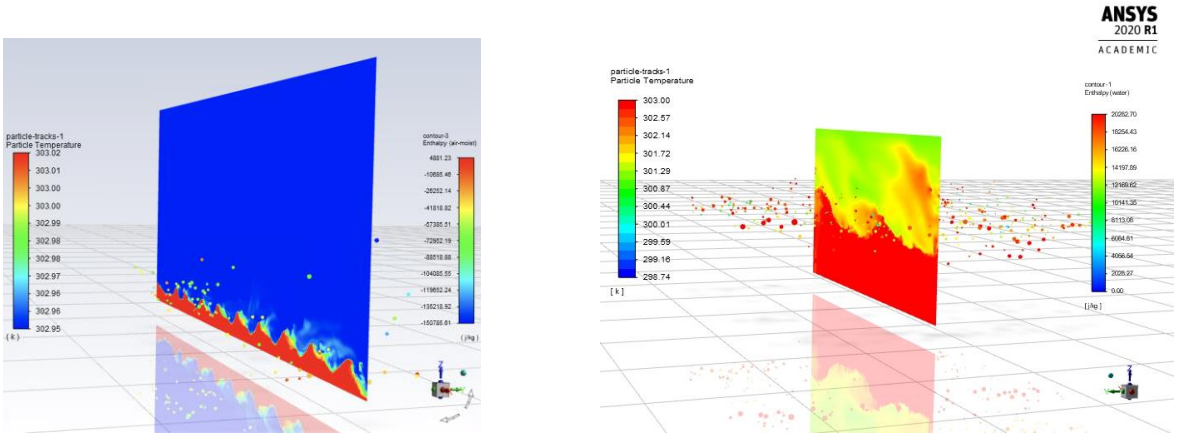

Figure 53. Implementation of heat fluxes and evaporation of spray particles in ANSYS Fluent. The particles are colored by their temperature and the contour, taken from the center of the domain, shows enthalpy (left – air, right – water).

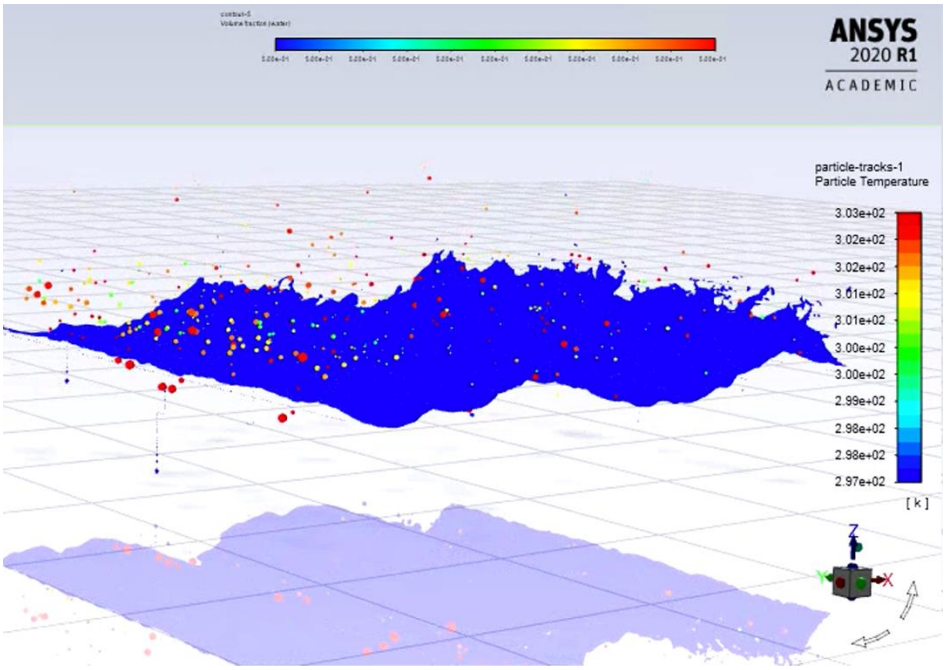

Figure 54. Spray colored by their temperature above an iso-surface of the sea surface within the VOF-to-DPM model.

Trial runs of the model implementing temperature, density, and relative humidity were successful enough for preliminary figures as shown above as well as some data analysis. Figure 55 shows the distribution of spray droplets by their diameter and temperature. We can see here that the largest droplets tended to stay near ambient water temperature (303 K) meanwhile

smaller droplets evaporated and cooled to lower temperatures (lowest being 297 K). This was as expected and provided some expectation that the model will work with future refinement.

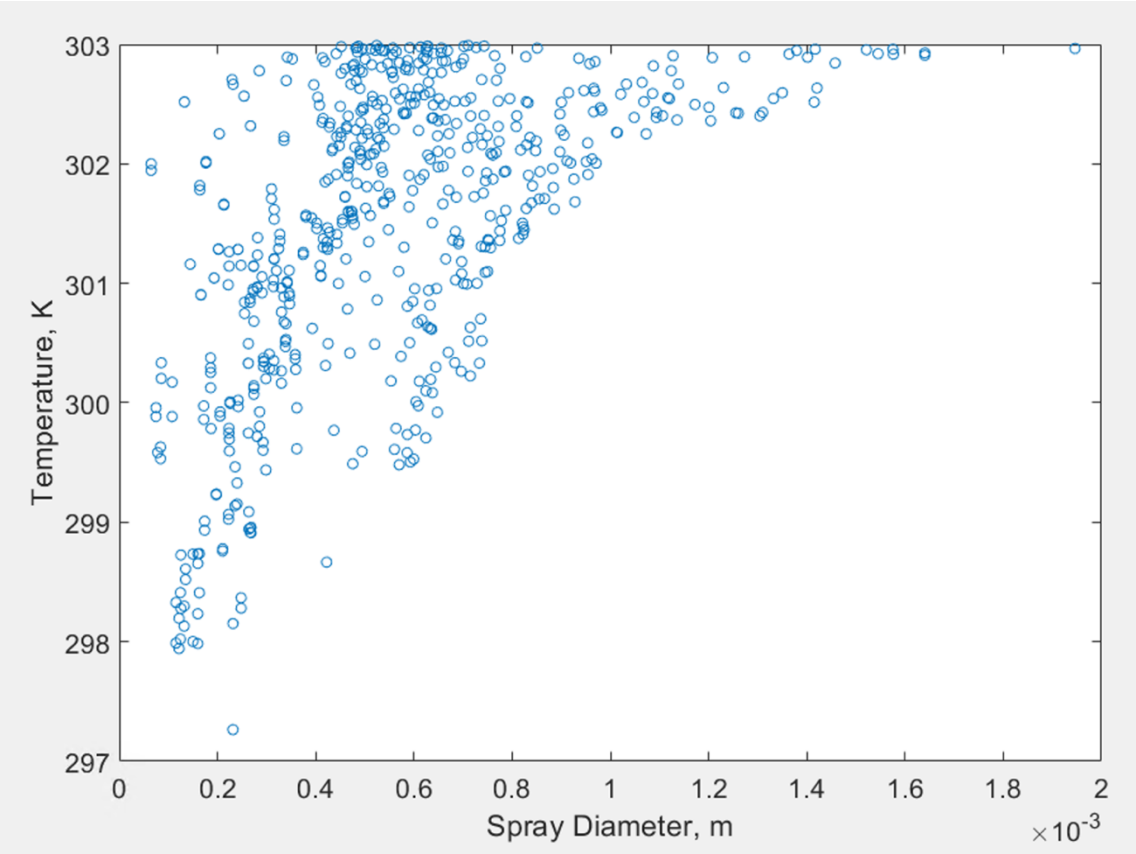

Figure 55. Temperatures of spray according to their diameter from the VOF-to-DPM model.

Fluent has recently implemented the DPM-to-VOF model to simulate particles re-entering the fluid, which will allow us to model re-entrant spray (spume) and the resulting heat and momentum fluxes that are crucial to tropical cyclone intensity forecasting. The DPM-to-VOF model tracks in the opposite direction as the VOF-to-DPM, as the Lagrangian particles reach the liquid phase (water), they convert from Lagrangian particles back into parcels of water ultimately re-integrating with the volume of fluid. The model ensures conservation of mass during this transition. Figure 56(a) shows the surface mesh as the particles are converted from Lagrangian to parcels of water. During this transition, mesh adaption will occur as many times as necessary to convert the particles successfully and accurately to parcels and create a cohesive

boundary while conserving mass. The mesh adaption also coarsens the mesh within the particle, where the interface is no longer needed (*ANSYS Fluent Theory Guide 2022R1*, 2022).

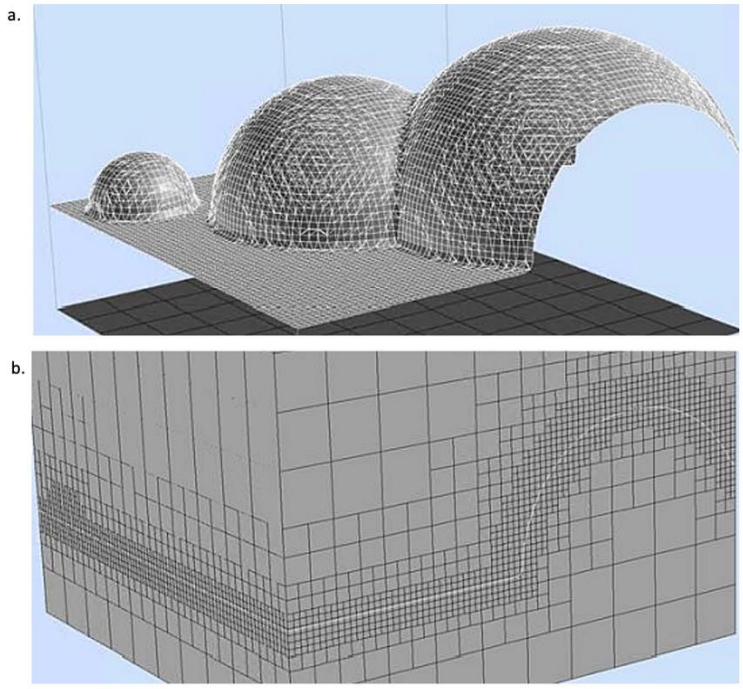

Figure 56. (a) The mesh at the gas-liquid interface after the DPM-to-VOF model is transitioned. (b) The surface mesh after adaption and transition of particles to volume of fluid (*ANSYS Fluent Theory Guide 2022R1*, 2022).

Trial cases were run to test this new implementation, despite the difficulties faced with the initial inclusion of heat and momentum fluxes. To implement this model, energy, temperature, and humidity had to be included in the model setup, as well as creating a third phase for the water droplets as parcels of water using the species module within Fluent. A second mechanism was added to our volume of fluid model converting between the DPM and VOF models, setting particles without secondary breakup with a volume fraction of above 0.8 to convert back to parcels of water, and particles with secondary breakup with a volume fraction above 0.01. After running the model for a short period of time (2.4 s of flow time), Figure 57 shows that droplets did indeed evaporate over the model run.

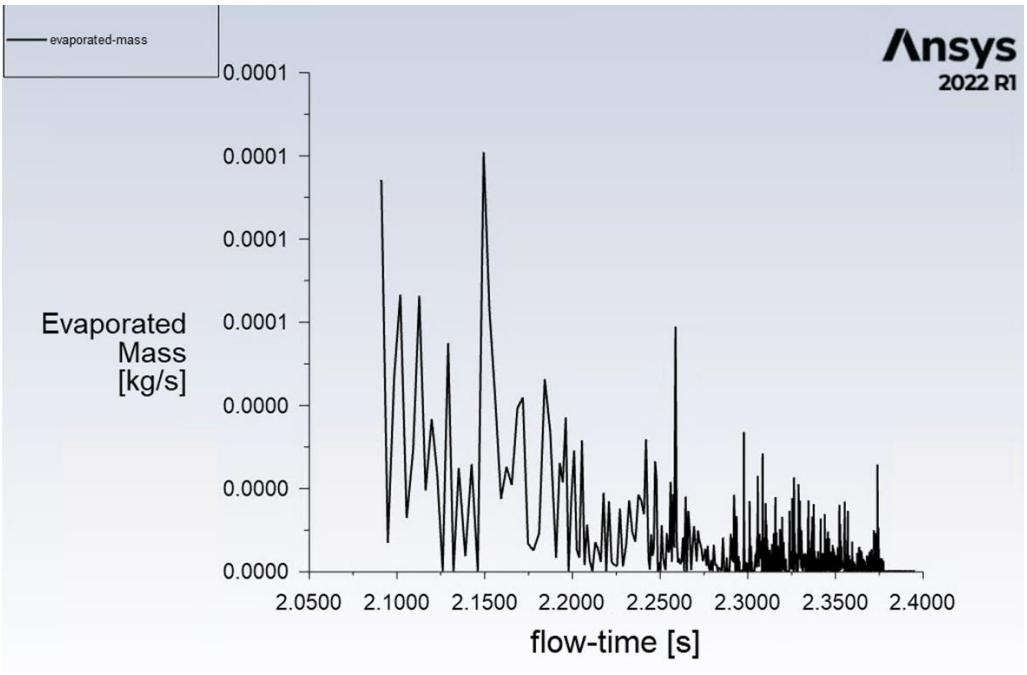

Figure 57. Evaporated mass from the VOF-to-DPM and DPM-to-VOF model.

The particles were tracked the same way as the VOF-to-DPM model and are shown in Figure 58. The smaller particles were entrained in the airflow, while the larger particles re-entered the water. By the end of the short model run, only one particle remained within the domain, as the rest had either evaporated or returned to the sea surface. The model does need further refinement to accurately calculate heat and momentum fluxes, as well as better tracking parameters to follow the tracks and eventual fates of the particles, whether they evaporated, re-entered the sea surface, or remained in the turbulent airflow.

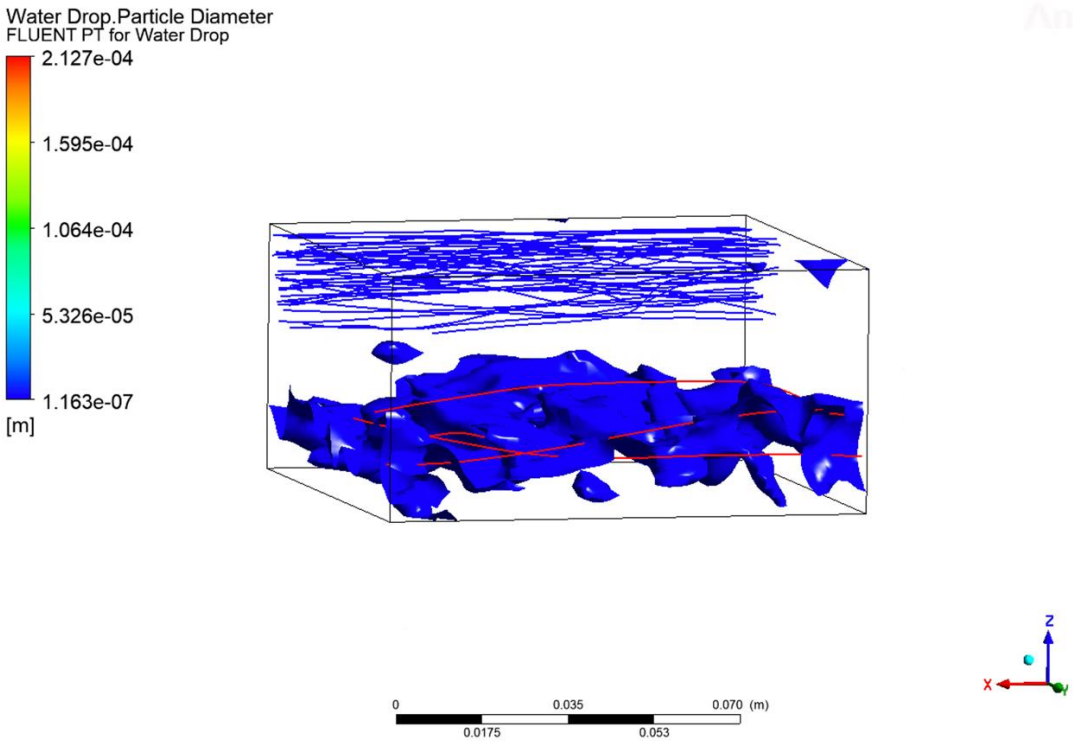

Figure 58. Spray droplet tracks from the DPM-to-VOF model.

Barr et al. (2023) successfully implemented heat and momentum fluxes into their spray model, from which they calculated a sea state-based SSGF based on that of Fairall et al. (2009). Like our model, they did not focus on film and jet droplets formed by bubble bursting, since they have little influence on heat and momentum fluxes of spray. Spray droplet heat transfer was approximated in their model based on Andreas (1989, 1990, 2005):

$$T_{drop,f} = T_{wb} + \left(T_0 - T_{wb} \right) exp\left(- \frac{\tau_f}{\tau_T} \right),$$
$$r_f = r_{eq} = \left(r_0 - r_{eq} \right) exp\left(- \frac{\tau_f}{\tau_R} \right), \quad (50\text{-}51)$$

where $T_{drop,f}$ and r_f are the droplet re-entry temperature and radius, and τ_T, τ_f, τ_R are characteristic time scales for droplet cooling, evaporation, and settling. Barr et al. (2023) then calculated the spray heat fluxes based on the temperature and size change calculated, respectively, as:

$$H_{T,spr} = \int c_{p,sw}\left(T_0 - T_{drop,f}\right)\frac{dm}{dr_0}dr_{0,}$$
$$H_{R,spr} = \int L_v\left[1-\left(\frac{r_f}{r_0}\right)^3\right]\frac{dm}{dr_0}dr_{0,} \quad (52\text{-}53)$$

where c_p, s_w, and L_y are the specific heat capacity and latent heat of vaporization of seawater.

Applying similar formulations for spray fluxes into the VOF-to-DPM and DPM-to-VOF model in future work would greatly enhance the overall research in the direction of fully understanding spray and spume fluxes, distributions, and the impact of surfactants in relation to tropical cyclone intensity.

6. Sea spray generation function

Another uncertainty in air-sea tropical cyclone dynamics is the sea spray generation function (SSGF). The SSGF is defined as the number of sea spray particles generated per square meter of surface per second per micrometer increment in the particle radius and is critical to understanding tropical cyclone dynamics and thermodynamics. Multiple estimates of the SSGF have been produced for low winds (Fairall et al., 1994; Andreas, 1998; 2002; Zhao et al., 2006; Veron, 2015; Ortiz-Suslow et al., 2016; Troitskaya et al., 2018a), but with a lack of experimental data in high wind conditions, a confident SSGF for tropical cyclones remains a challenge (Sroka & Emanuel, 2021). A critical component of the SSGF under high winds is the generation of spume (>250-um radius). Using the previously described numerical results, this proposal plans to produce a SSGF for high wind speeds.

6.1. Methods

During all model runs in ANSYS Fluent, a direct export of the spray generation was set up to save to a file. This file contained the location (cartesian coordinates), diameter, and time of generation for the individual spray particles. Using this file, I was able to generate plots for results including spray counts, spray spatial distributions, and calculate the SSGF. The SSGF as a function of volume flux was calculated as the number of drops produced per unit area, per unit time, per unit drop radius (Eq. 4). Error bars were calculated from the standard deviation.

Figure 59 shows an example of the air-water interface within this model for Category 3 tropical cyclone winds. Those close to spherical shape are converted into rigid Lagrangian particles, which interact with the airflow in two ways. Those which are nonspherical are less rigid and are often larger and more susceptible to breakup.

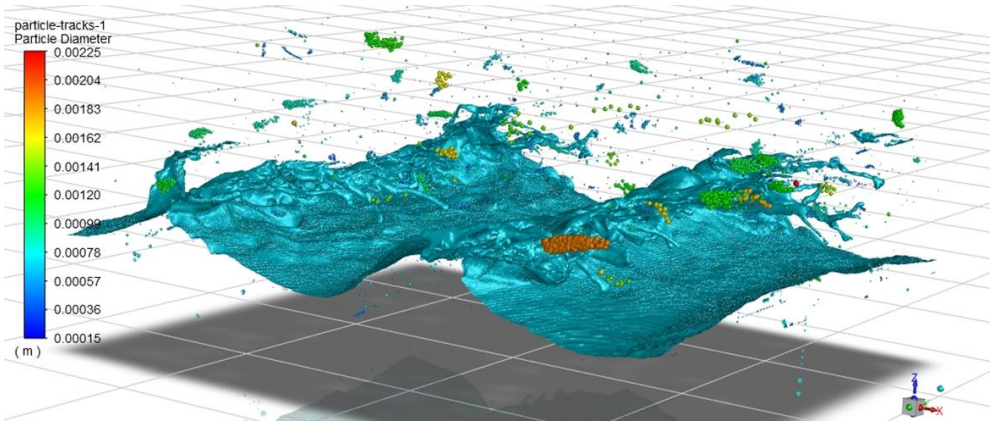

Figure 59. VOF to DPM iso-surface and spray particles colored by diameter under Category 3 tropical cyclone conditions.

6.2. Results and Discussion

Multiple SSGF parameterizations have been produced for low winds (Fairall et al., 1994; Andreas, 1998; 2002; Zhao et al., 2006; Veron, 2015; Ortiz-Suslow et al., 2016; Troitskaya et al., 2018a), but with a lack of experimental data in high wind conditions, a confident SSGF for tropical cyclones remains a challenge (Sroka & Emanuel, 2021). A critical component of the SSGF under high winds is the generation of spume (>250-um radius).

A key aspect of the VOF-to-DPM model is that spray is generated at the air-sea interface in real time, compared to traditional sea spray models (Richter & Sullivan 2014; Peng & Richter 2019) where sea spray is artificially injected into the model domain. Because of this, the VOF-to-DPM model has the advantage of allowing for the calculation of the SSGF directly at the air-sea interface with very few assumptions involved. The SSGF as a function of the volume flux was calculated from the Category 1 models both with and without surfactants is shown in Figure 60. When surfactants are present, there is an increase in the SSGF by roughly a factor of three. The rate of spray produced is particularly higher in the 150-250 μm radii range where we saw the

most influence from surfactants on our distribution results (Fig. 23). In larger radii, ripples can be seen in the SSGF due to less particles in this range.

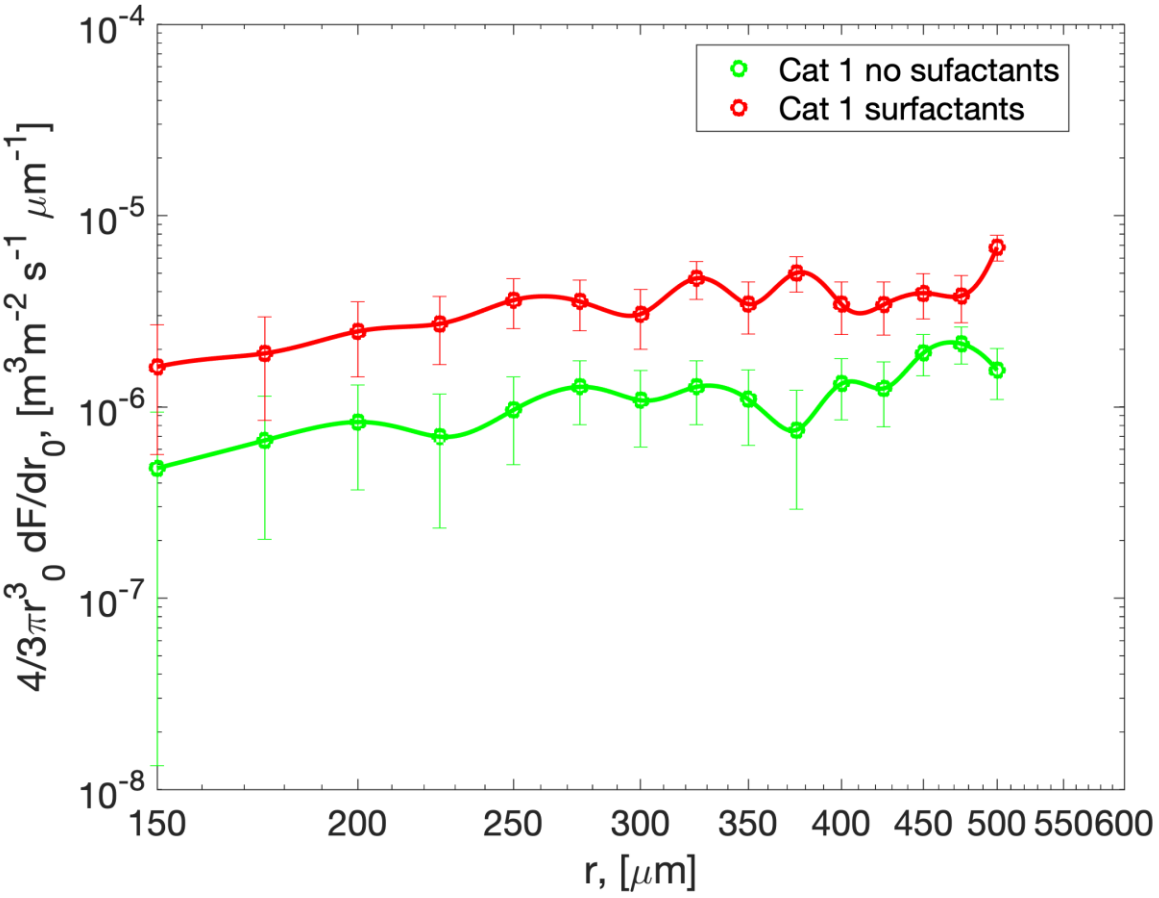

Figure 60. SSGF for Category 1 tropical cyclone conditions with (red) and without (green) surfactants.

As seen in Figure 61, under Category 2 conditions, the difference between nonsurfactant and surfactant conditions begins to narrow, especially once larger droplet sizes are reached. The Category 3 model SSGF is shown in Figure 62. Overall, there is an increase in the SSGF with increasing wind speed, as expected. The difference between the case with and without surfactants remains narrow once Category 3 conditions are reached, as seen in Category 2 conditions (Fig. 61).

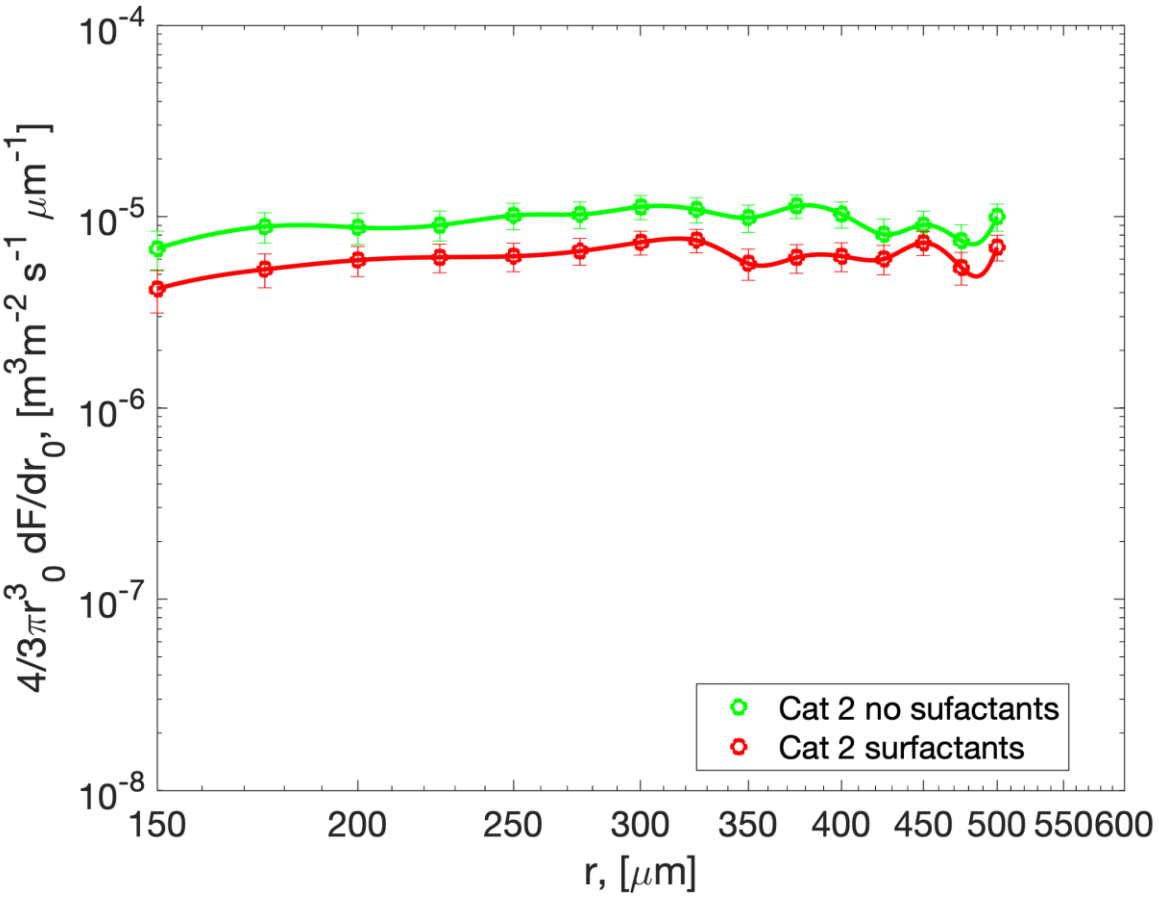

Figure 61. SSGF for Category 2 tropical cyclone conditions with (red) and without (green).

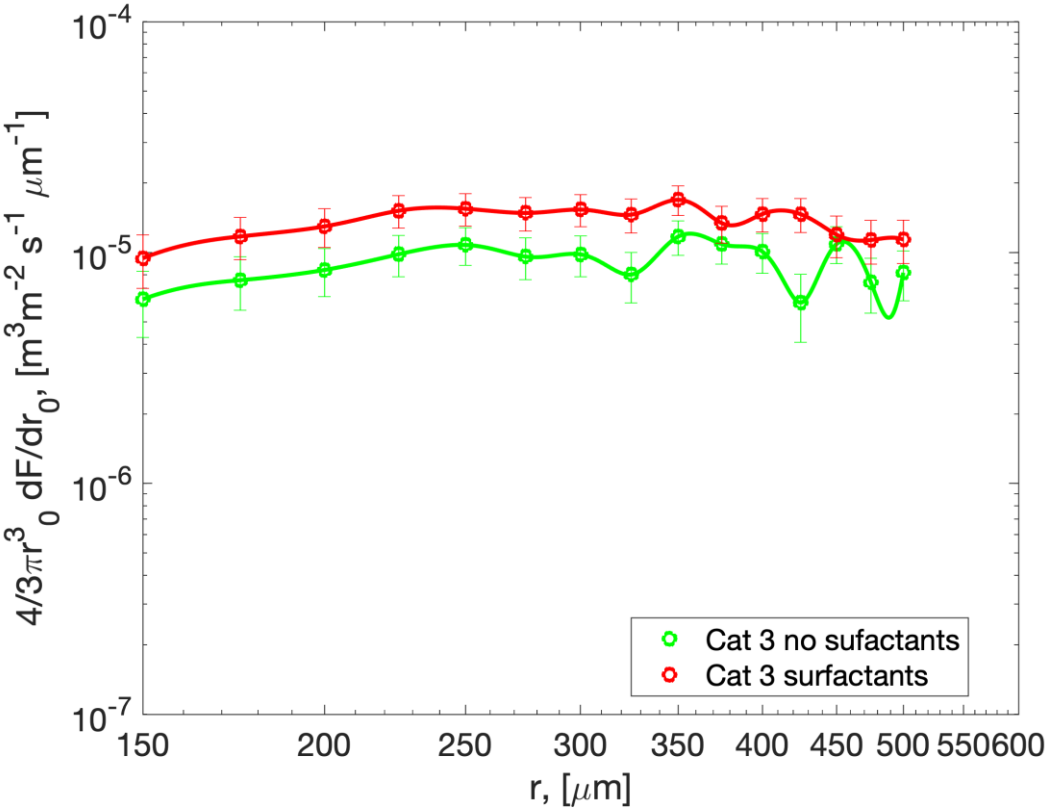

Figure 62. SSGF for Category 3 tropical cyclone conditions with (red) and without (green) surfactants.

As we reach Category 4 tropical cyclone conditions, there is almost no difference between the case with and without surfactants (Fig. 63). This varies from the direct count results, which show an increase of spray with surfactants at all tropical cyclone conditions. Even more surprising, the case without surfactants is slightly higher than the run with surfactants for this category. There is, as expected, an increase in the overall SSGF as compared to Category 3 conditions.

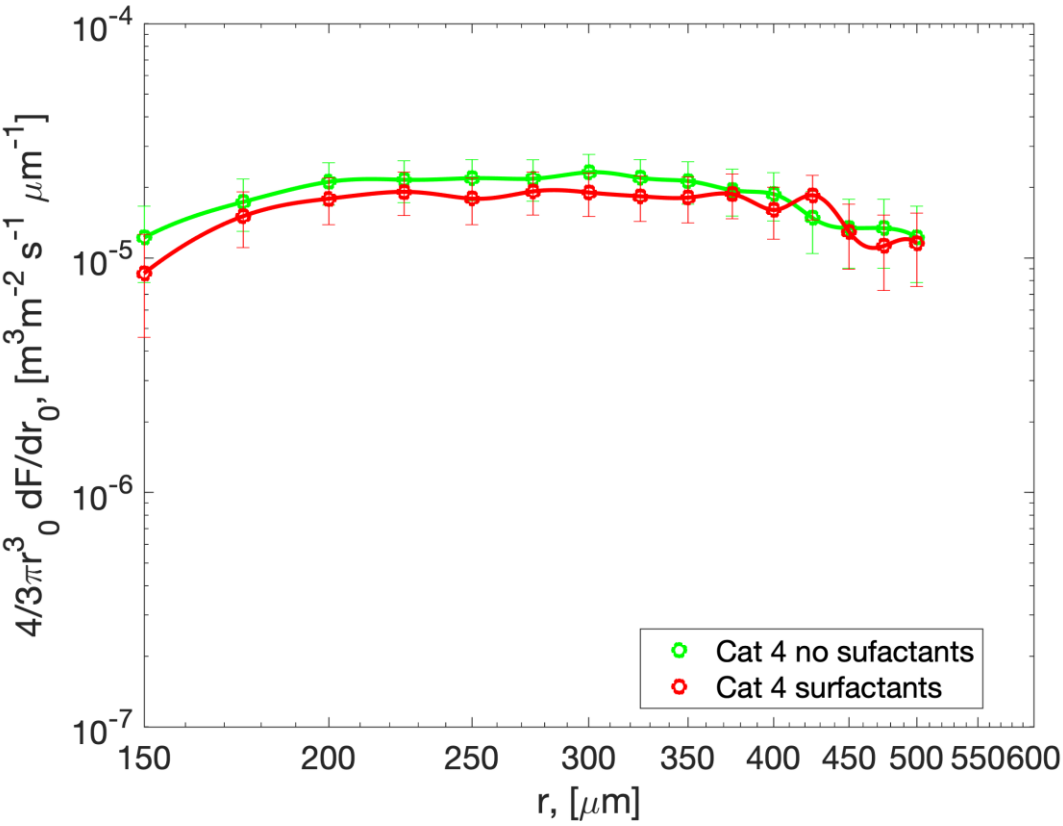

Figure 63. SSGF for Category 4 tropical cyclone conditions with (red) and without (green) surfactants.

Category 5 tropical cyclone conditions, shown in Figure 64, yields the highest SSGF, as anticipated. Surprisingly, there is little difference between the surfactant and nonsurfactant case, as seen in the Category 4 SSGF as well. As we reach higher radii, the surfactant case increases to surpass the SSGF from the nonsurfactant case, which could be due to an increase in nonspherical particles, which are usually larger and breakup.

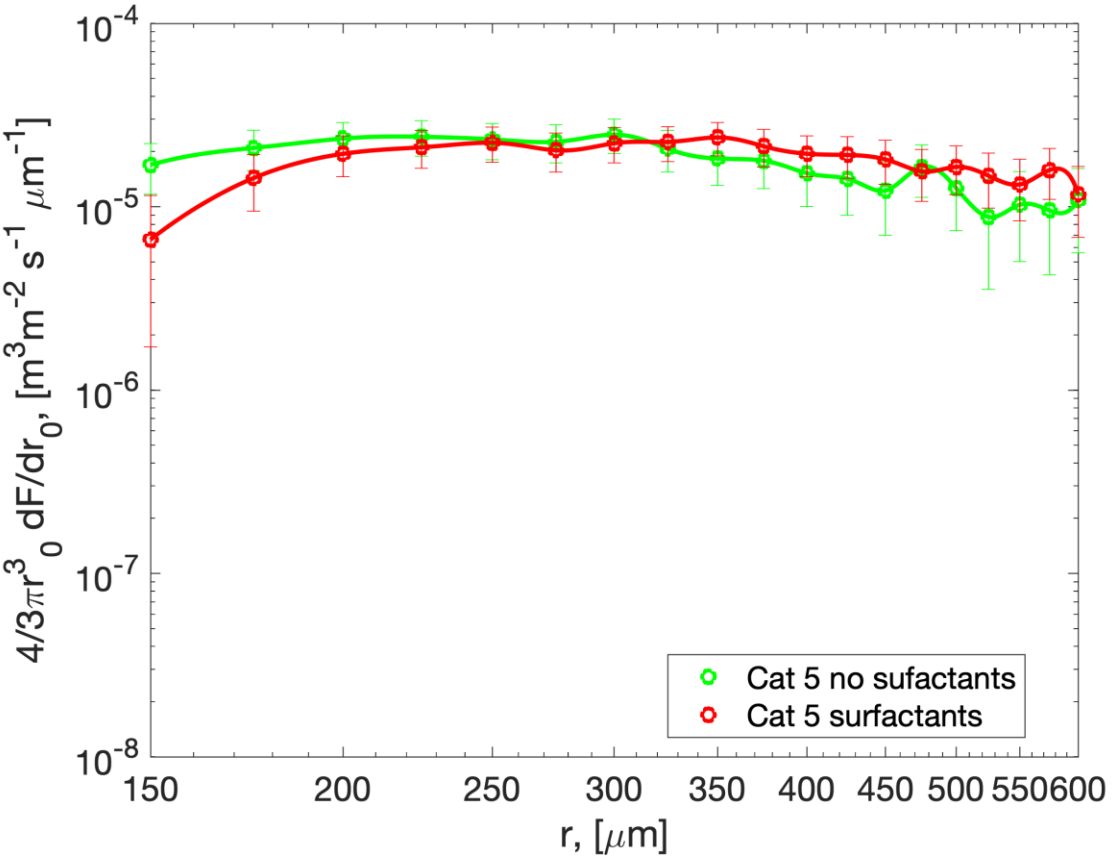

Figure 64. SSGF for Category 5 tropical cyclone conditions with (red) and without (green) surfactants.

Plotting all the tropical cyclone category SSGFs together (nonsurfactant), shown in Figure 65, shows the significant increase with increasing category and therefore with wind. Unexpectedly, Categories 2 and 3 were much closer than expected, as were Categories 4 and 5.

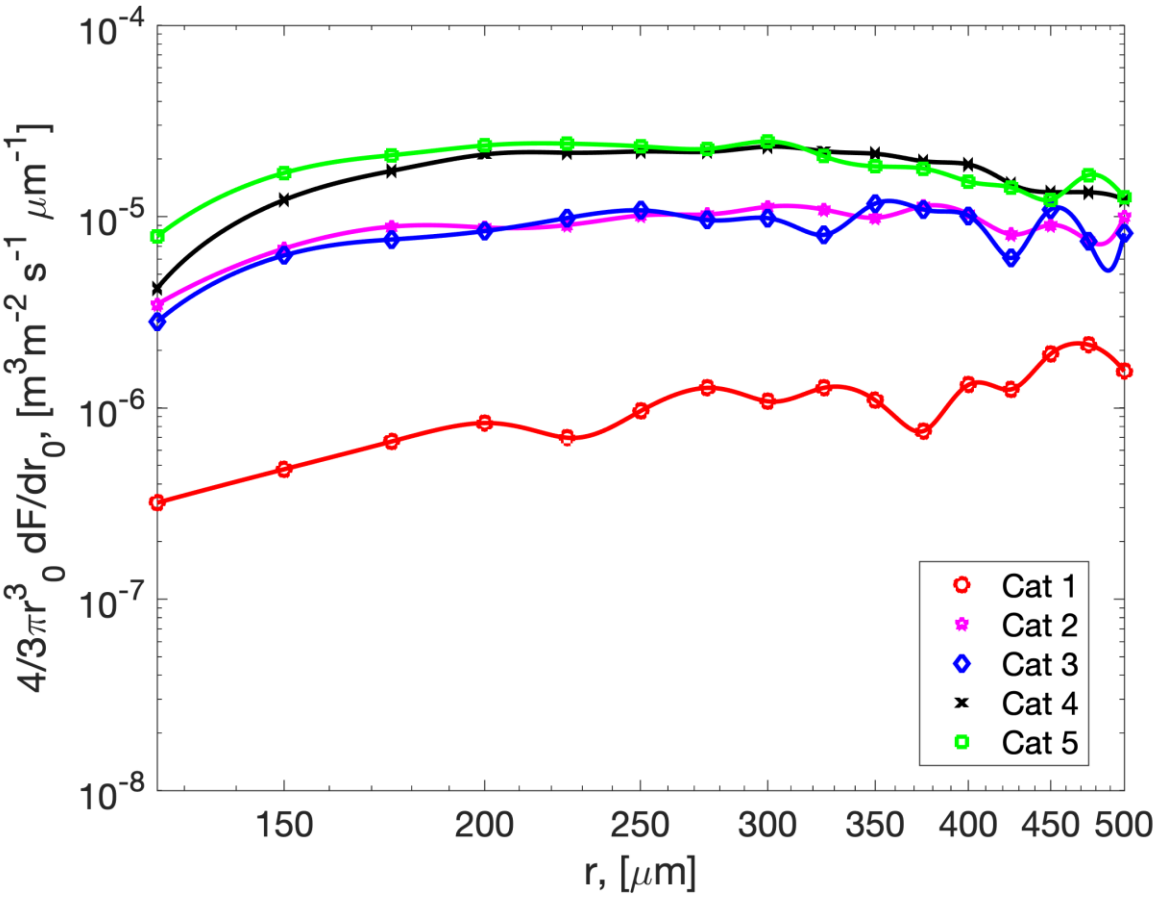

Figure 65. SSGF for all tropical cyclone conditions (without surfactants).

When surfactants were present (Fig. 66), Category 1 increased and was much closer to Category 2 conditions, and Category 3 also increased to be closer to Category 4 conditions.

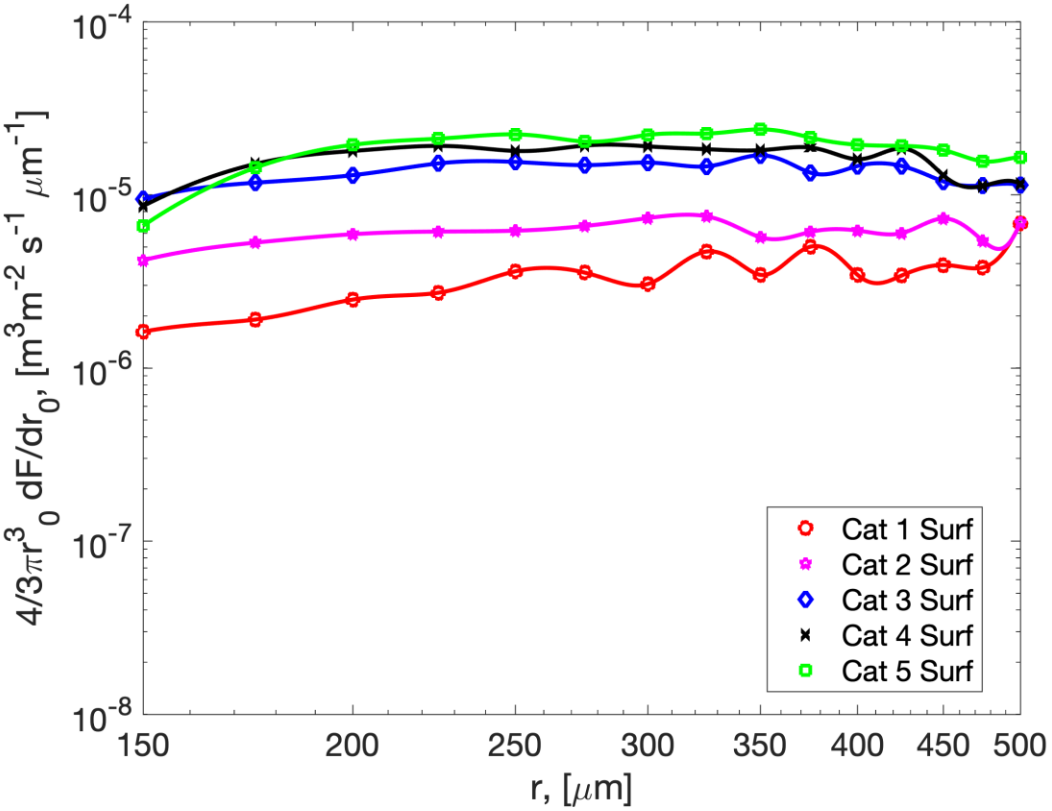

Figure 66. SSGF for all tropical cyclone conditions with surfactants.

It is important to note that the results from spray counts and the SSGF seem contradictory. This is because the results from Figure 23 strictly focused on counts of spray over the entire time of the model run. Meanwhile, the results from the SSGFs (Figs. 60-64) give a more accurate picture of spray generation by calculating the spray volume flux, rather than just abundance. This is key to understanding the impact spray and spume has on heat, momentum, and gas fluxes under high wind speeds. Looking solely at the SSGF may not yield a full understanding of spray at the sea surface, and looking at other parameters including abundance, size distributions, and the fate of the spray droplets (evaporation or re-entrance to the sea surface) are also important to completely understand the microscale processes that occur.

The calculated SSGFs from the model revealed an increase in the spray generation under Category 1 and 3 tropical cyclone conditions. However, under Category 4 and 5 conditions, there was little to no impact of surfactants on spray generation, which could be explained by a change in regime under major (greater than Cat. 3) tropical cyclones. Emanuel (2003) hypothesized that, at high enough wind speeds, the air-sea transition is governed by a single length scale, implying

that exchange coefficients based on a gradient wind will become independent of wind speed. There are three important length scales in this system: a Charnock-like length scale, a length scale governing the molecular diffusion of momentum, and an equilibrium drop size (sea spray), determined by gravity and surface tension. Emanuel (2003) formed three dimensionless combinations of the control parameters: the square of the ratio of the Charnock length to a measure of the maximum stable size of a spray droplet in a gravitational field, a nondimensional measure of surface tension, and the ratio of the kinematic viscosities of the two fluids, respectively:

$$R_u \equiv \frac{u_*^4}{\sigma g'} \qquad R_\sigma \equiv \frac{\sigma}{v_l^{4/3} g'^{1/3}} \qquad R_v \equiv \frac{v_l}{v_a} \tag{54-56}$$

Based on this theory, as wind stress becomes very large, air-sea transfer is dominated by spray physics. At high wind speeds, the character of the system becomes independent of R_u and u_*. Emanuel (2003) hypothesized that at extreme wind conditions, the air-sea interface is no longer defined corresponding to the sea surface (Fig. 67). It was seen in our SSGF results that surface tension no longer influenced the spray generation once winds above Category 3 tropical cyclone conditions were reached.

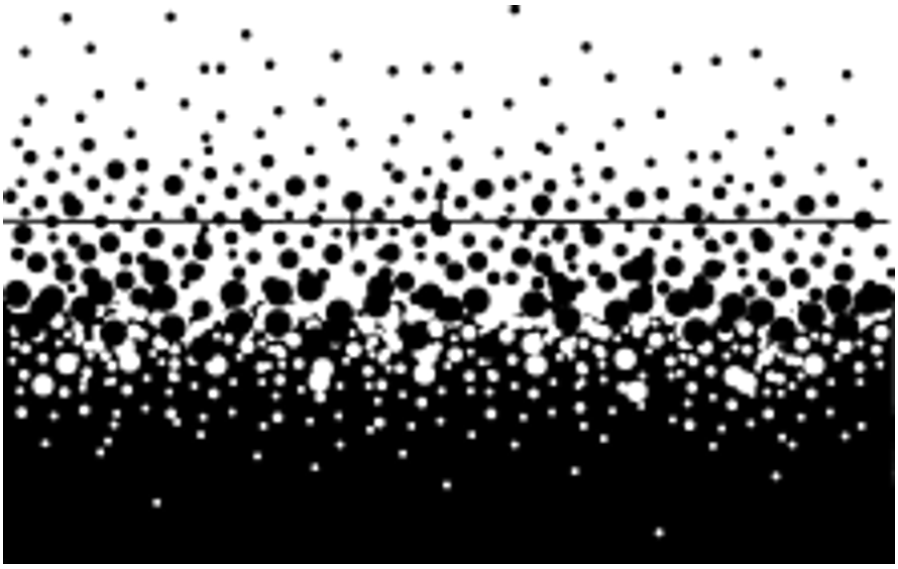

Figure 67. The air-sea interface under extreme winds. Spray droplets are ejected upward and accelerate towards the free stream velocity, absorbing momentum from the atmosphere (From Emanuel 2003).

Visual observations under extreme conditions describe spray filled air and suppressed wind waves, suggesting a difference regime prevails at very high winds. Based on the hypothesis and dimensional analysis of Emanuel (2003), lab results from (Krall et al., 2019; Jähne, 2019), and field observations, there is likely a change in regime at the air-sea interface under extreme tropical cyclone conditions. We also see this change of the regime in our CFD modeling. Our SSGF results indicate a change in regime under major tropical cyclones and no dependence on surface tension under major storms. This finding reinforces the need for an enhanced understanding and parameterization of the underlying physics in existing forecast models to improve the accuracy of tropical cyclone intensity predictions.

The sea state-based SSGF implemented by Barr et al. (2023) favored larger droplet production at higher wind speeds, which is the area we focused on in this work (>150 μm). The shape of the SSGF was analyzed from their model, revealing that the inclusion of the sea state altered the shape of the SSGF, notably at the smallest and largest radii ranges. The efficiency of the SSGF to transfer heat shape of the wind based SSGF does not change based on windspeed, since the determining factor is the change in residence time of the droplet with increasing wind. Meanwhile, the sea state-based SSGF has the highest efficiency for heat transfer at the wind speeds around 30 m s^{-1}, which can be seen in Figure 68a. This means that the SSGF favors smaller droplets since the largest droplets decrease the heat transfer efficiency at the highest wind speeds. The efficiency for size change dramatically increases with wind speed for the sea state-based SSGF, and slightly for the wind based (Fig. 68b).

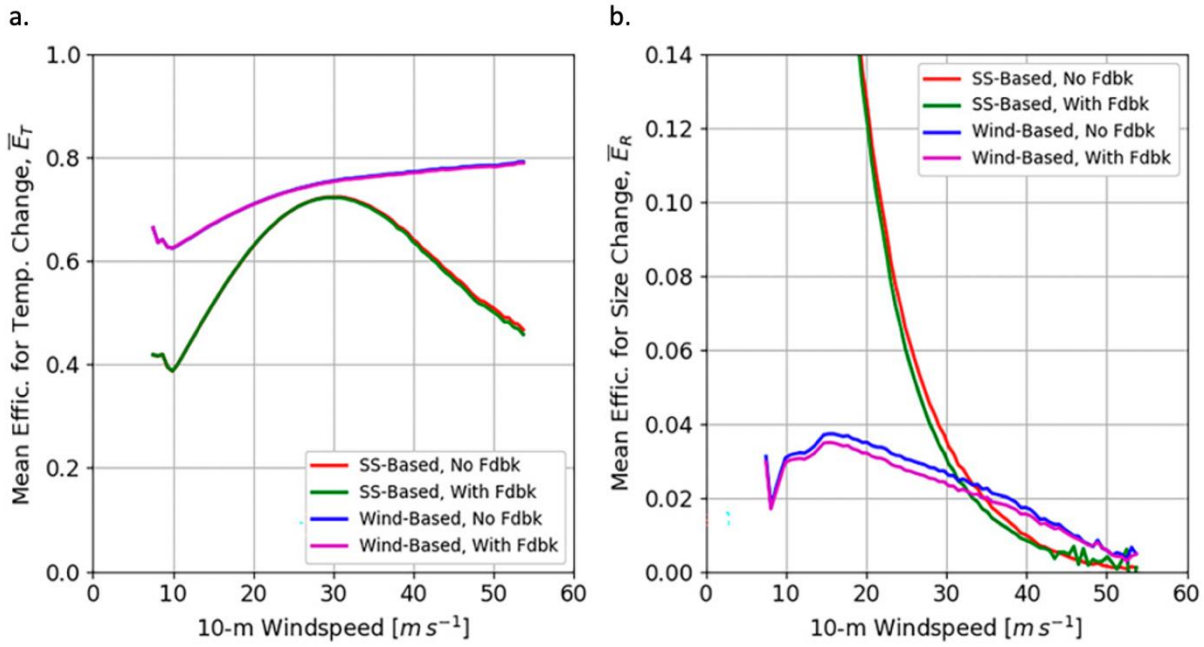

Figure 68. From Barr et al. 2023. Mean (a) heat transfer efficiency and (b) size change efficiency, showing results with and without near-surface feedback using both SS- and wind-based SSGFs.

When considering the total heat flux, the sea state-based SSGF increased the total latent heat flux at the radius of maximum wind. Outside of the storm's eyewall, the sensible heat flux was reduced by including a SSGF in the model runs. At the radius of maximum wind, however, the sea state-based SSGF increased the sensible heat flux by 20%. Their SSGF that incorporated the sea state rather than just wind yielded a spray mass flux higher by an entire order of magnitude, showing the importance of incorporating the sea state into spray functions. This is likely due to changes in microphysics at the air-sea interface, as discussed in the introduction of this dissertation. The changes in the air-sea interface including whitecapping and whiteout ultimately change the spray distribution and radii, and therefore the heat and mass fluxes. The spray heat fluxes are impacted by the spray mass, the energy available for heat transfer, and the efficiency with which the flow can take the available energy. Barr et al. (2023) found that heat transfer was most efficient for droplets near 20 μm with respect to size change and 300 μm due to temperature change. Overall, their results concluded that spray depends significantly on the sea state, droplet heat transfer efficiency depends on ejection height of the droplet, the sensible

and latent heat fluxes are strongly coupled through evaporative cooling, and that the heat fluxes in general of droplets are coupled through near-surface feedback effects.

Ideally, the new SSGF parameterization from the VOF-to-DPM will assist in an accurate estimation of spray and spume's contribution to tropical cyclones and could be implemented into models such as Barr et al. (2023) to yield more realistic spray generation than previous injected spray diameter ranges in various spray models. This parameterization could then be implemented into forecasting models to better predict tropical cyclone intensity.

7. Gas exchange

While air-sea gas exchange has been studied for many years, Krall et al. (2019) was the first to do so under high wind speeds in saltwater by utilizing wind-wave tanks at Kyoto University and University of Miami. Krall et al. (2019) were successful in determining that gas transfer velocity's dependence on solubility at the air-sea interface is reduced dramatically under tropical cyclone winds, but they did not study spray and spume's influence on gas exchange. They did find that there was low gas transfer of Helium at high winds, which indicates that wave breaking, spray and spume generation influence gas transfer, but exactly how is still poorly understood. Potentially, gas flux at high winds is proportional to surface area of spray since it is no longer dependent on gas solubility. Spray and spume generation are dramatically increased under increasing wind speeds, meaning that the gas flux may also increase significantly. Using our CFD model results of spray and spume distributions could present crucial insight into understanding the influence of spray on gas flux under tropical cyclones. Using the species mass transfer implemented into our VOF-to-DPM to model trace gas transfer under tropical cyclones and validate the model with results from Krall et al. (2019) is also a method in work. Once again, surfactants add another aspect into understanding this phenomenon. Because surfactants dampen waves, they ultimately alter the wave slope spectra which has been shown to reduce gas exchange (Frew, 1997; Bock et al., 1999). Surfactants also increase spray generation (Vanderplow et al., 2020) and therefore will potentially increase the gas flux through increased spray and spume concentration.

Andreas et al. (2017) assessed the time scales that control spray-mediated air-sea gas transfer. During gas transfer, a gas molecule undergoes the same processes from the droplet to the air and vice versa, but in reverse order. A gas molecule mixes between the interior surface

and the deeper interior of the aqueous droplet, crosses the droplet's surface interface, and passes through a 'jump' layer between the exterior surface of the droplet and the air. The internal mixing, crossing of the interface, and passing through the jump layer are dictated by the time scales τ_{aq}, τ_{int}, and τ_{air}, respectively (Fig. 69).

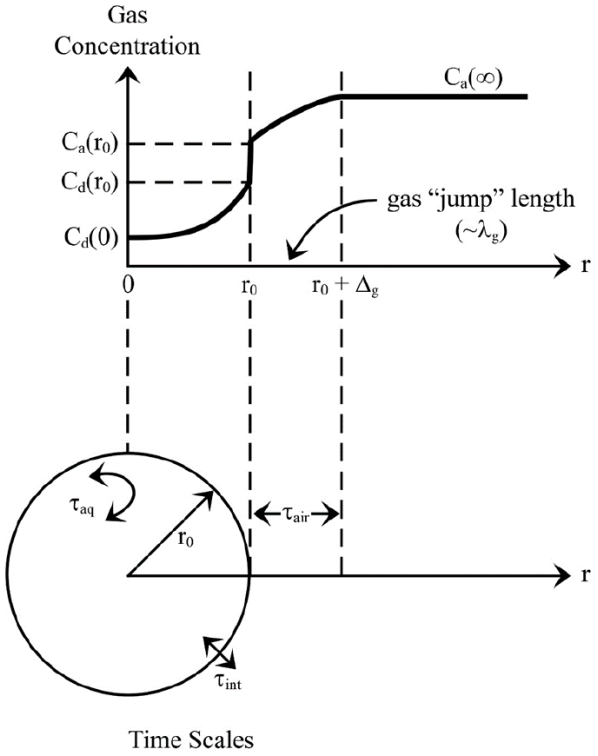

Figure 69. The gas concentration, C, as a function of radial distance, r, from the center of a spray droplet and the three time scales (τ_{aq}, τ_{int}, τ_{air}) relevant to spray-mediated gas exchange (Andreas et al. 2017).

As shown in Figure 70, τ_{aq} is the largest time scale and is the most comparable with the droplet's residence time (τ_f). Surfactant contamination of a droplet will decrease mixing within the droplet, consequently increasing τ_{aq}. On the other hand, when surfactants are absent, mixing within the droplet will increase, leading to a decrease in the time scale, shown as 0.1 and 0.01 τ_{aq} in Figure 70. As the droplet radius increases, τ_{aq} becomes larger than the residence time of the droplet, meaning there is not sufficient time for the droplet to fully de-gas before it returns to the sea surface. On the other hand, τ_{int} is much smaller than τ_f, meaning that the droplet has enough time to equilibrate before it either evaporates or returns to the water. Surfactants

increasing τ_{int} will still not change this trend, and therefore is less critical to understand the effect of surfactants on spray-mediated gas exchange than τ_{aq}. In summary, gas transfer at the droplet surface is less important than the volume when surfactants are present. When surfactants are present under extremely high winds, spray generation is increased. As the volume of spray increases, gas transfer is also likely to increase the aqueous time scale should still be considered under high winds, as it could potentially decrease gas transfer through increased mixing in the presence of surfactants.

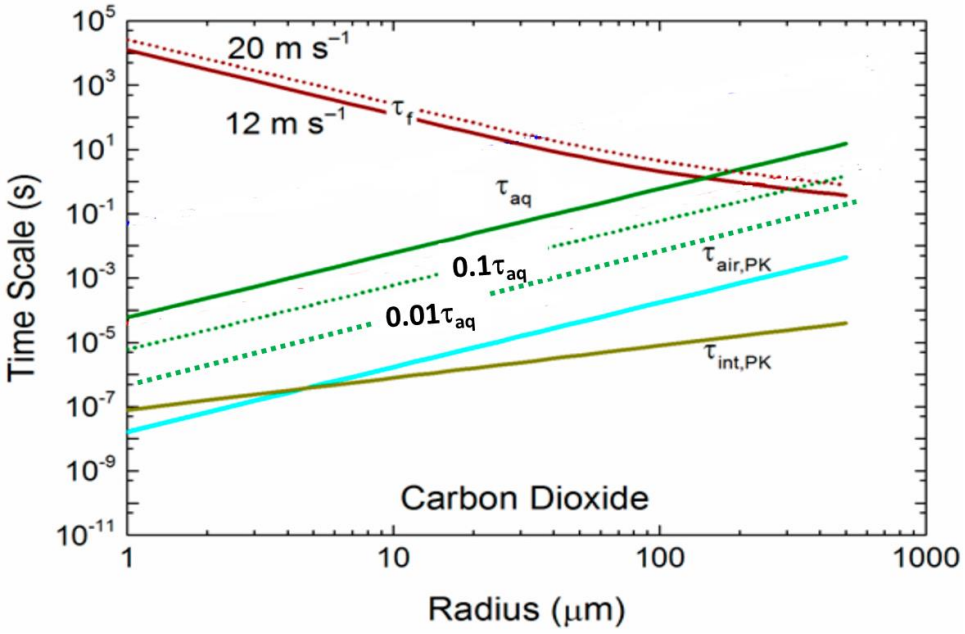

Figure 70. Microphysical time scales for droplet residence time (τ_f), the transfer of carbon dioxide molecules to or from a droplet in air (τ_{air}), across the spray droplets interface (τ_{int}), and within the droplet (τ_{aq}). The time scale in air derives from Pruppacher and Klett (2010). 0.1 and 0.01 τ_{aq} represent increased mixing within the droplet when there is no contamination from surfactants.

Previous work by Krall et al. (2019) and Jähne (2019) found that above 33 m s^{-1} a new gas transfer regime is established, which we also see in our CFD modeling. In this consideration of surfactant effects on gas transfer under extremely high winds, the effect of surfactants on air-sea gas transfer remains unclear. The presence of surfactants increases air-sea gas exchange velocity proportional to the volume flux of sea spray. Based on the considerations of Andreas et al. (2017), the interfacial time scale of spray droplets is very small and has little effect on gas

transfer. Surfactants may increase the internal mixing time scale for spray droplets, which would result in a reduction of the gas transfer velocity. Taking these factors into consideration, the total effect of surfactants on spray-mediated gas transfer remains uncertain.

8. Measurement and modeling of small-scale to mesoscale features in a western boundary current

A major challenge in modeling western boundary current dynamics is that it is a very energetic sub-mesoscale environment. Majority of ocean circulation modeling is done on regional and global scales. With recent technological advances, most of today's high-resolution models still only reach a resolution near 1 km. Traditional ocean models are hydrostatic, meaning they use the hydrostatic approximation to make calculations of the flow easier to compute (Fox-Kemper et al., 2019). Thompson and Schmitz (1989) modeled of Gulf Stream dynamics using a 0.2-degree model grid (~23 km). The Regional Ocean Modeling System (ROMS) is a hydrostatic model often used in ocean circulation studies. Gula, Molemaker, and McWilliams (2015) used ROMS to reproduce Gulf Stream dynamics with a horizontal parent grid of 6 km, nested with a maximum horizontal resolution of 750 m. Kang and Curchitser (2013) focused on eddy characteristic in the Gulf Stream using their model with a 7 km horizontal resolution. Models that do not rely on the hydrostatic approximation are less common. Nonhydrostatic models are more computationally expensive, but provide a more accurate, three-dimensional simulation. Mahadevan, Oliger, and Street (1996a,b) developed a nonhydrostatic circulation model that included a free-surface for the Gulf of Mexico with a 40 km horizontal resolution. SUNTANS (Fringer et al., 2002) and MITgcm (Marshall et al., 1997) are both nonhydrostatic models that can resolve mesoscale oceanic processes. Marshall et al. (2006) used 1/20° and 1/100° grid resolution to model eddies in the Southern Ocean, a resolution not fine enough to resolve small-scale to sub-mesoscale processes. Suzuki et al. (2016) produced a remarkable model of small-scale to sub-mesoscale fronts down to a 4.9 m x 4.9 m x 1.25 m grid scale within a numerical domain size of 20 km × 20 km × 160 m. Unfortunately, their model could not be validated with direct observations. Finger, McWilliams, and Street (2006) developed a hybrid ROMS-SUNTANS model to combine large-scale and mesoscale to sub-mesoscale ocean circulation modeling. Nonydrostatic effects are only important on small-scales to sub-mesoscales. Modeling ocean circulation on these scales is essential to characterizing ocean dynamics in energetic areas such as western boundary currents. The nonhydrostatic model

described in this work is a novel approach for an ocean circulation model with a horizontal resolution of 10 m that has the ability to describe small-scale to sub-mesoscale oceanic features in the challenging environment of a western boundary current. In addition, this model is verified with observations.

A new approach to modeling in the range of small-scale to sub-mesoscale features in a western boundary current - computational fluid dynamics model

Replicating ocean dynamics on sub-mesoscales is challenging in numerical models. Here we have implemented an engineering type modeling - Computational Fluid Dynamics (CFD). ANSYS Fluent CFD software provides a large assortment of physical model capabilities, including flow, turbulence, multiphase, and heat transfer that have been validated and produce highly accurate results. CFD, while computationally expensive, provides a rigorous nonlinear treatment of the Navier-Stokes equations involved in modeling mass and momentum transfer, critical to fluid dynamics. By discretizing CFD domains in space and time, the system of equations is formed and implemented into a domain mesh and timesteps during the simulation (Windt, Davidson, and Ringwood, 2018). CFD-based modeling of ocean processes can capture small-scale to mesoscale features and provide high-resolution results to better understand flow and currents in places challenging to study, such as western boundary currents like the Florida Current.

ANSYS Fluent has been used to study various fluid dynamics and related oceanographic processes. Soloviev, Fujimura, and Matt (2012), Soloviev et al. (2014; 2017), and Vanderplow et al. (2020) applied ANSYS Fluent CFD modeling for air-sea interaction studies. Dean (2018) applied ANSYS Fluent to various oceanographic processes including internal waves, ocean circulation, and freshwater lenses. Jiang et al. (2014) modeled the structures and behaviors of turbidity currents in the South China Sea. Machado et al. (2018) modeled the generation and propagation of waves in a numerical wave tank using ANSYS. Park et al. (2018) compared Fluent and IHFOAM models of wave breaking on elevated structures, finding that both models showed relatively good agreement with field measurements. Simonetti et al. (2015) compared two common CFD turbulence models, k-w SST and LES, for application to oscillating water column wave energy converters and found that while both methods provided agreeable results to their measurements, the LES model results were closer to experimental data, although it was more computationally expensive. Sjökvist et al. (2017) utilized Fluent to simulate wave energy

converters and verify their models using experimental results. CFD has aided in studying the interaction between oil and dispersants, which is critical to oil spill mitigation (Soloviev et al., 2016). Soloviev, Dean, & Fujimura (2015) used CFD to study salinity fluxes in freshwater lenses and their connection to the ocean barrier layer (Lukas & Lindstrom, 1991). CFD is an effective tool to model and predict a variety of oceanographic processes once validated with field or laboratory measurements.

In this work we demonstrate that validated CFD simulations combined with field data provide an effective way to assimilate available oceanic information and predict small-scale to sub-mesoscale processes in the area of interest within a certain time range.

8.1. Methods

8.1.a. Field Experiments

The deployment in the Straits of Florida was designed to measure ocean currents, water conductivity-temperature-depth, and bottom pressure variability necessary to develop a CFD model of the Florida Current in the study area. The mooring array deployed ~12.9 km offshore at roughly 250 m depth contained fourteen moorings: six acoustic Doppler current profiler (ADCP) moorings intended to measure ocean current velocity profiles, five pressure moorings intended to measure bottom pressure, three temperature-conductivity-depth (CTD) mooring strings to measure water density throughout the water column. The pressure and CTD mooring data are not used for the version of the CFD model presented in this paper (see Discussion). The moorings were deployed in a rectangular pattern (Fig. 71) across the shelf. ADCP moorings were spaced ~850 m apart from one another, as were the CTD mooring chains.

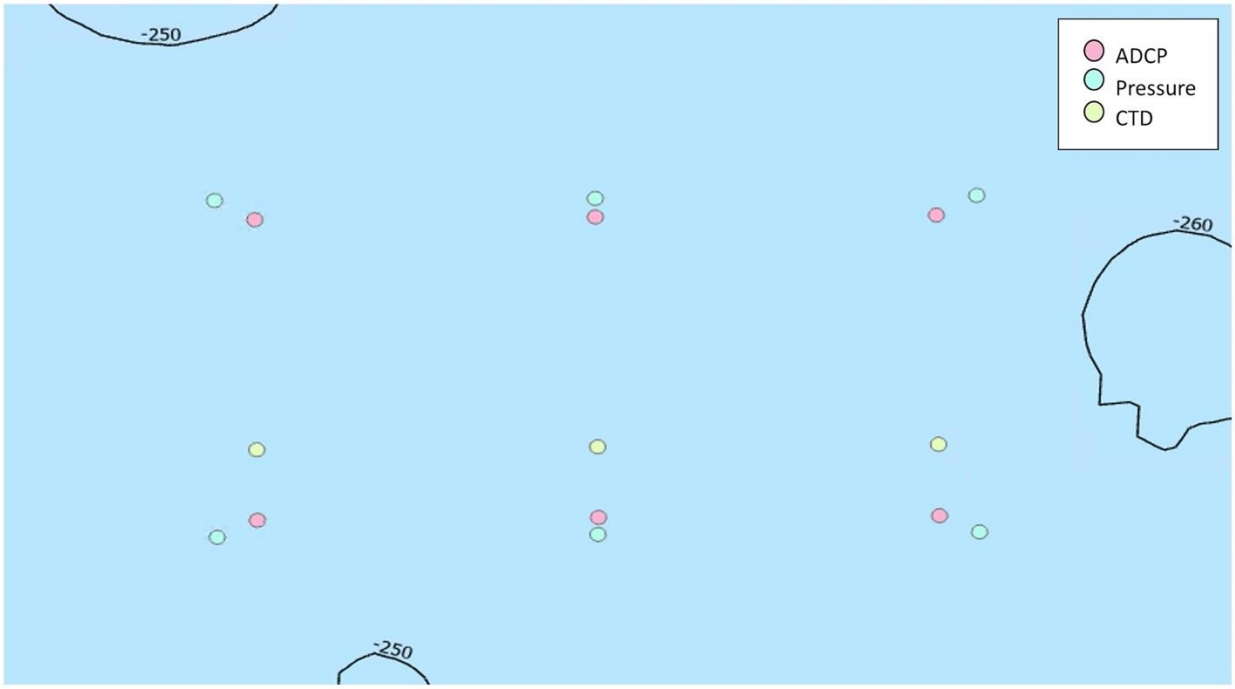

Figure 71. Mooring array design in the Straits of Florida showing location of the moorings and the bottom topography in the area of interest.

Current measurements were obtained with upward-looking Teledyne RD Instruments 150 kHz Quartermaster ADCPs placed 8 m from the seafloor and looked upwards with a 4 m vertical resolution (ensemble-averaged every 1 min). Each ADCP was fixed with a Deepwater Buoyancy, Inc. 49" syntactic spherical buoy and protected by a stainless-steel mounting cage (Fig 72b). A 900 kg railroad wheel anchor with a 3/8" proof coil chain was used as an anchor for each mooring. A Teledyne Benthos model R2k acoustic release was placed halfway between the anchor and buoy. For the pressure moorings, an RBR, Ltd RBRquartz^3 Q digiquartz high-accuracy pressure transducer was mounted using clamps in a stable bottom-mounted stainless-steel frame and cast concrete anchor ~20 cm above the seafloor. Trawl floats were used to add 25 kg of net positive buoyancy. The pressure moorings were also equipped with a Xeos satellite beacon and Teledyne Benthos R500 acoustic release. The CTD mooring strings consisted of eight Sea-Bird Electronics, Inc. SBE-37SMP CTD sensors spaced 25 m apart along the mooring line, beginning at 22 m below the sea surface to ~197 m below the sea surface. A Stable-Moor torpedo-shaped syntactic foam buoy was used for stability (620 kg of positive buoyancy) at the top of the mooring wire (Fig. 72a). This type of buoy effectively improved the lift-to-drag ratio of the CTD mooring and, therefore,

increased overall mooring performance and data quality. The CTD moorings also contained a spherical backup buoy, A Teledyne Benthos model R12k acoustic release, and a 1550 kg railroad wheel anchor. Figure 73a shows a contour plot of the northward velocity component from an ADCP deployed during June-September 2020, while Figure 73b shows the temperature time series for one of the CTD moorings deployed during the same time period.

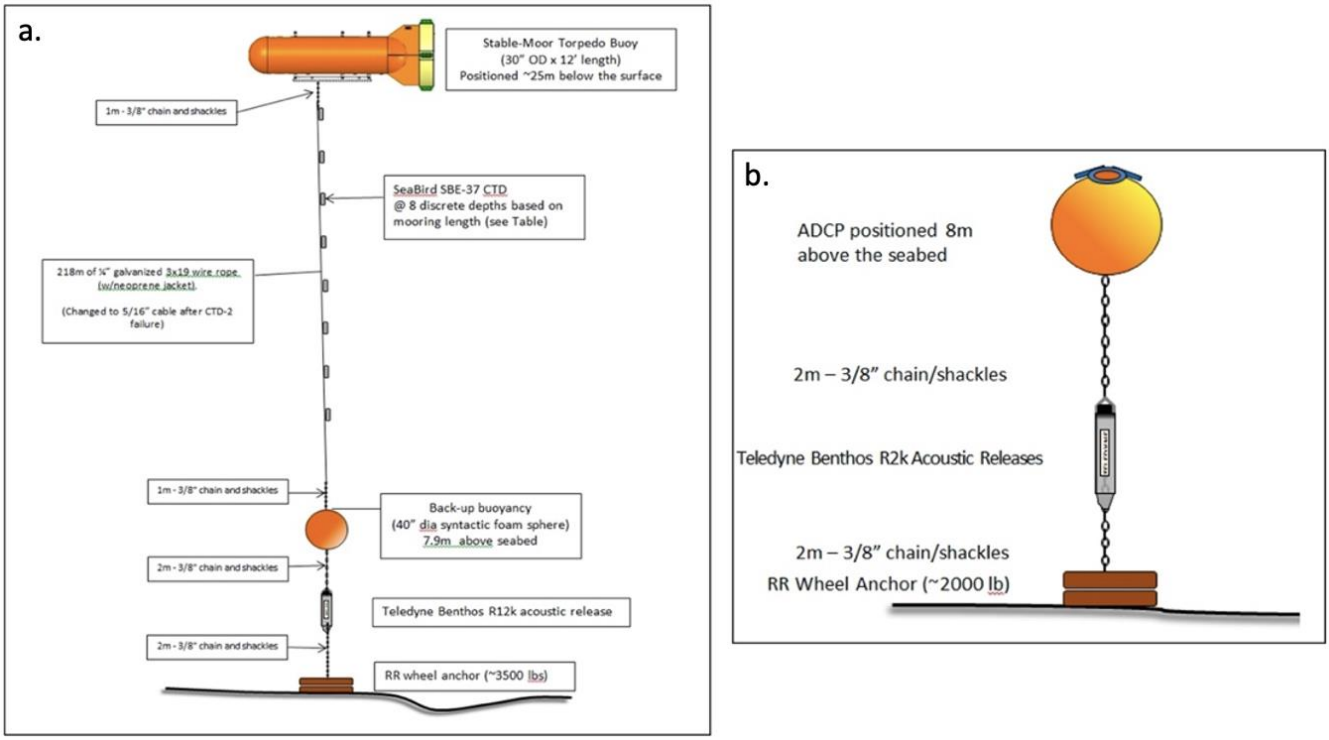

Figure 72. Mooring designs for CTD chains and ADCP moorings (a) The Stable-Moor buoy and (b) the ADCP buoy.

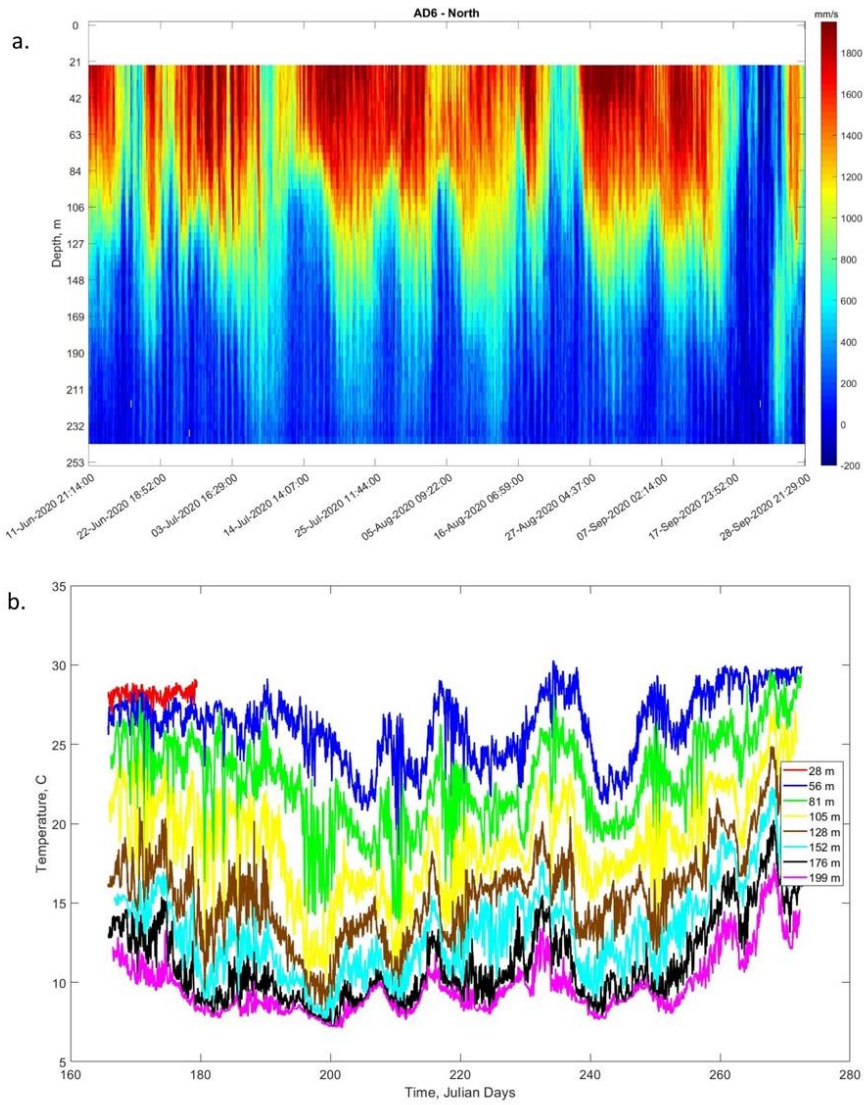

Figure 73. (a) Northward velocity component in the Straits of Florida. (b) Temperature time series from one of the CTD moorings in the Straits of Florida.

8.1.b. CFD modeling

Using ANSYS Fluent, in this work, we have created a CFD model to characterize sub-mesoscale flows in the Florida Current over 3D space and time using field data and realistic bottom topography from an area off the East coast of Florida. The model uses a transient, pressure-based solver and Large Eddy Simulation (LES) option. LES resolves large eddies as they incorporate momentum, mass, and energy and depend on the geometry and boundary conditions. Meanwhile, small eddies are universal when modeling turbulence. The LES governing equations are

formulated from time-dependent Navier-Stokes equations, filtered in either Fourier (wavenumber) space or physical space. Filtering removes eddies with scales that are too small for the grid spacing in Fluent (*ANSYS Fluent Theory Guide 2022R1*, 2022).

Straits of Florida ANSYS Fluent CFD model domain and mesh

The model domain was 1700 m in the X direction (East/West) and 852 m in the Y direction (North/South). The model domain (Fig. 74) includes the seafloor, top boundary (rigid lid), side boundaries (three inlets and one outlet), and fluid (water layer). The model was initialized with ADCP velocity data and contained bottom topography from the area of the mooring array that was imported from NOAA data.

Bottom topography data, downloaded from NOAA's Digital Elevation Model as a GeoTIFF, first had to be converted into an STL file for import to ANSYS geometry software using the DEM to 3D plugin QGIS. The STL was then imported into ANSYS SpaceClaim as a faceted body. Each side of the faceted body was skinned using ANSYS SpaceClaim's reverse engineering tool to form a 'solid' body. Then three fluid zones were added above the bottom topography consisting of the surface fluid zone (0 m to -30 m), main fluid zone (-30 m to -200 m) and the bottom fluid zone (-200 m to bottom topography). The surface fluid zone was initialized with ADCP field data that was repeated from the topmost available ADCP bin from the field experiment. The bottom fluid zone was initialized with ADCP field data that was repeated from the bottommost available ADCP bin from the field experiment. Since the boundary condition on the seafloor was set to no slip, Fluent automatically interpolated the data to 0 m s^{-1} at the seafloor. Once these zones were created, it was necessary to form a single component with all three solids and share topology between them to avoid auto-generated walls at interfaces when imported into ANSYS Fluent.

The domain was then transferred to ANSYS Meshing to generate the mesh. In the surface and main fluid zones, the cubic mesh in the Z direction matched the ADCP resolution of 4 m. The cubic mesh in the X direction was 10 m and in the Y direction 6 m. The bottom fluid zone and bottom topography zones had a tetrahedral mesh to reflect the shape of the seafloor.

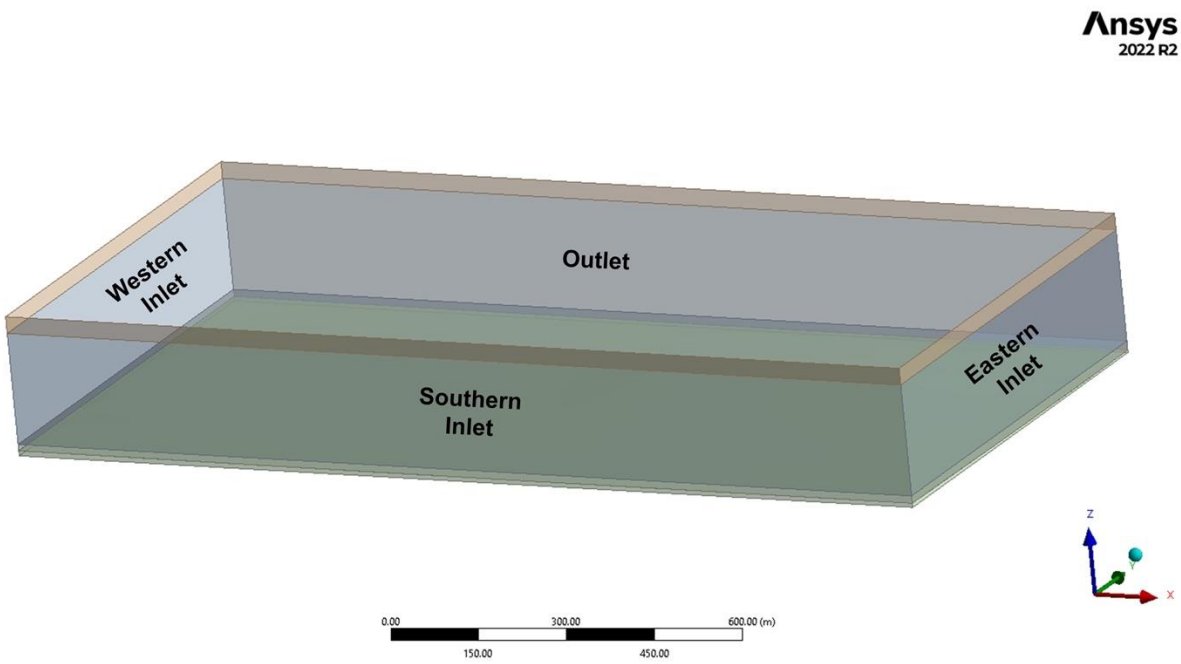

Figure 74. The model domain including the surface, main, and bottom fluid zones and solid (seafloor) zone in the area of the mooring array in the Straits of Florida. The solid zone includes data imported from a NOAA digital elevation model imported into ANSYS Fluent using reverse engineering in SpaceClaim.

To implement an air layer, which was done after the initial model run from Figure 74, an additional box was added to the existing domain. This box was connected directly to the surface layer box and shared topology with the rest of the domain to ensure continuity in the model run. The updated domain is shown in Figure 75.

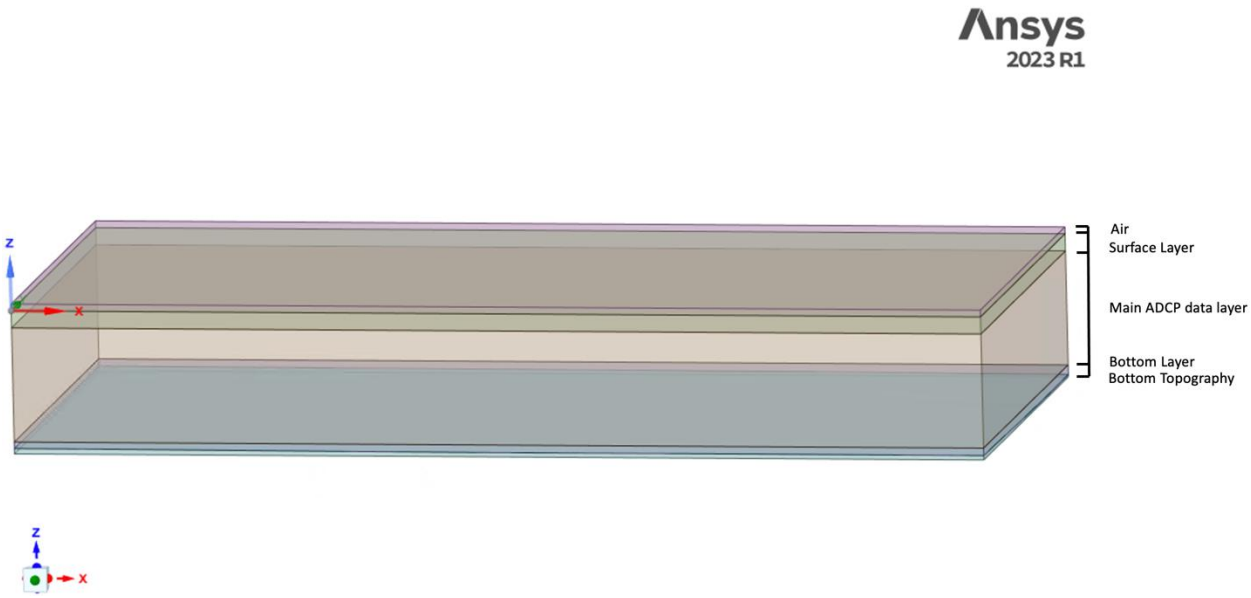

Figure 75. Domain in ANSYS SpaceClaim including bottom topography, fluid zone, and air layer.

Smoothed data for North, East, and vertical velocity components were used to make horizontal and vertical planes to initialize the model domain. Using the 6 ADCPs, we created vertical planes of data. Horizontal planes were created for each depth at the resolution of the ADCP (4 m). The data was linearly interpolated between the available data points to create full planes that matched the model domain and mesh size. To fill the surface and bottom fluid zones, the topmost and bottommost available ADCP data bin from the field experiment was repeated, respectively. In the air layer run, 0 m s^{-1} velocities were added to the air layer. Profile files were used to initialize the velocity values from field data in the volume of the domain and at the boundaries of the model. From the field data, text files were made containing the velocity measurements, that is, the proper number of cells for the horizontal and vertical mesh. One file was made for all velocity components of the volume initialization and individual files for each boundary. Journal files were used to read in the profile files automatically every 1 min.

After loading the mesh into ANSYS Fluent, the volume profiles for velocity were read and added to the fixed values input of the fluid cell zone. A transient formulation and a pressure-based solver were used, and gravity was set to -9.81 m s^{-2} in the Z direction. The viscous LES WALE model was used for turbulence. Water was the material in the fluid zone. The solid zone was left to default aluminum (does not interact with the fluid zone in our model). Coriolis force was

implemented into the model using a user-defined function that added x and y momentum to the domain. The seafloor boundary was set to no-slip. Wind stress calculated from averaged wind speed taken from Fowey Rock Meteorological Station during the time of the field deployment was applied to the top of the domain for the case without an air layer. Since the top of the domain is a rigid lid, this results in a complication for simulation of internal waves and tides. Due to the rigid lid at the top of the domain, internal waves and tides periodically induce backflow at the outlet. This was remedied by including the air layer shown in Figure 75, which allows for tidal fluctuations within the model domain. The velocity in the volume of the domain and velocity boundary conditions for the inlets of the fluid zones (East, West, and South inlets) were set using the previously mentioned ADCP field data planes. After the initialization, the boundary conditions were set to update using the ADCP velocity data every 1 min at the East, West, and South inlets of the fluid zones. The vertical velocity was initialized in the volume and at the inlet boundary conditions, but after initialization was no longer updated every 1 min as the North and East velocity components were.

8.2. Results and Discussion

Model without air layer

The outlet of the domain was left without boundary conditions so that the model results could be compared to an ADCP on the North side of the array for validation. Figure 76a-c shows contours of the North, East, vertical velocity components after 21228 s of running the model. Figure 76d shows the East velocity just above the bottom topography. After running the model for a flow time of 21228 s, or about six hours, we compared the model output results to the field data. Velocity profiles were exported from the outlet (North side of the domain) using CFD-Post post-processing software.

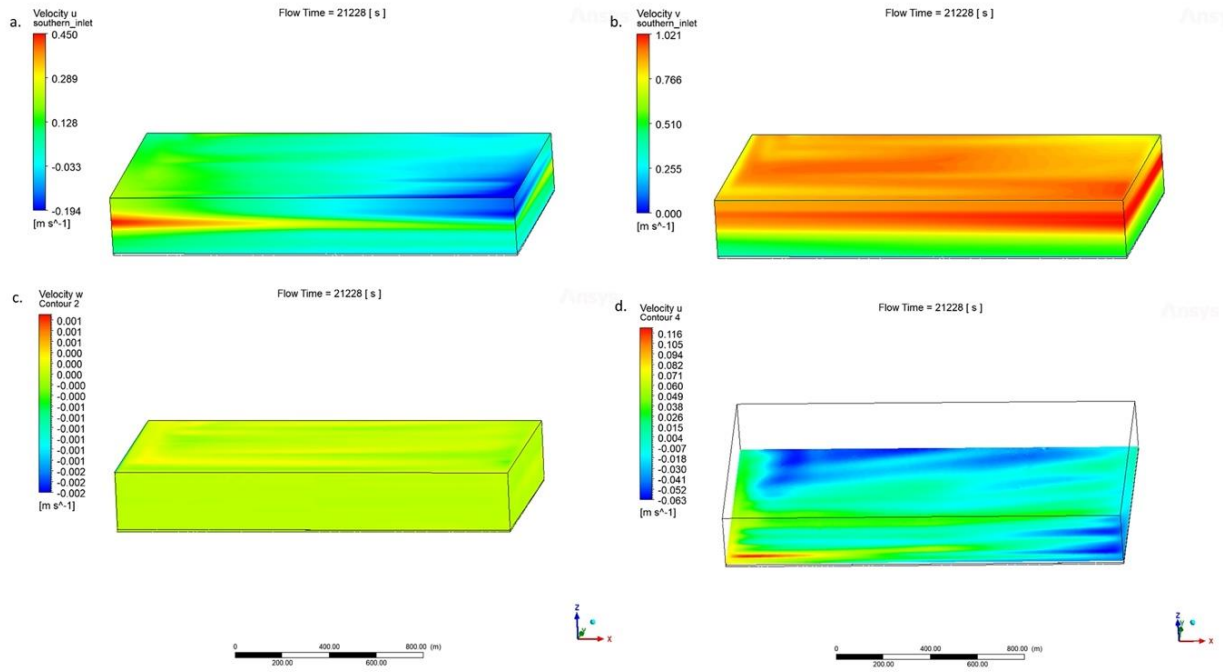

Figure 76. (a.) East velocity, (b.) North velocity, and (c.) vertical velocity contours at the East, South and Top boundaries and (d.) East velocity near the bottom boundary after 21228 s of flow time (~6 hours).

The model was able to sufficiently predict small-scale and sub-mesoscale oceanic features when initialized with field data from the Gulf Stream. A quantitative comparison between the model and the field data was done using the control ADCP (whose data was not used for boundary conditions) located in the middle of the north side of the mooring array. After ~6 hours of simulation, model results from the middle of the north outlet, the location of the control ADCP mooring, were exported from the model to compare to the field data. The model was verified by the comparison to the field data. Examples of the velocity components taken during time steps throughout the model run are shown in Figures 77 and 78. The green line shows the interpolated ADCP data, red the raw ADCP data, the blue line shows the model output, and the dashed line near the bottom shows the interpolated field data to the seafloor. Figure 79 shows the component average of the velocity over the entire model run. The field data in Figures 77 and 78 have much more variability than the output in Figure 79, since they are not averaged, but the trends in the velocity components between the model and field data still follow one another, particularly as the model run progresses (Fig. 78). Note that there was no field data near the seafloor because the

upward looking ADCP was providing data only starting from ~10 m above the bottom (Fig. 72b). Though this 10 m thick near bottom layer was covered by the model.

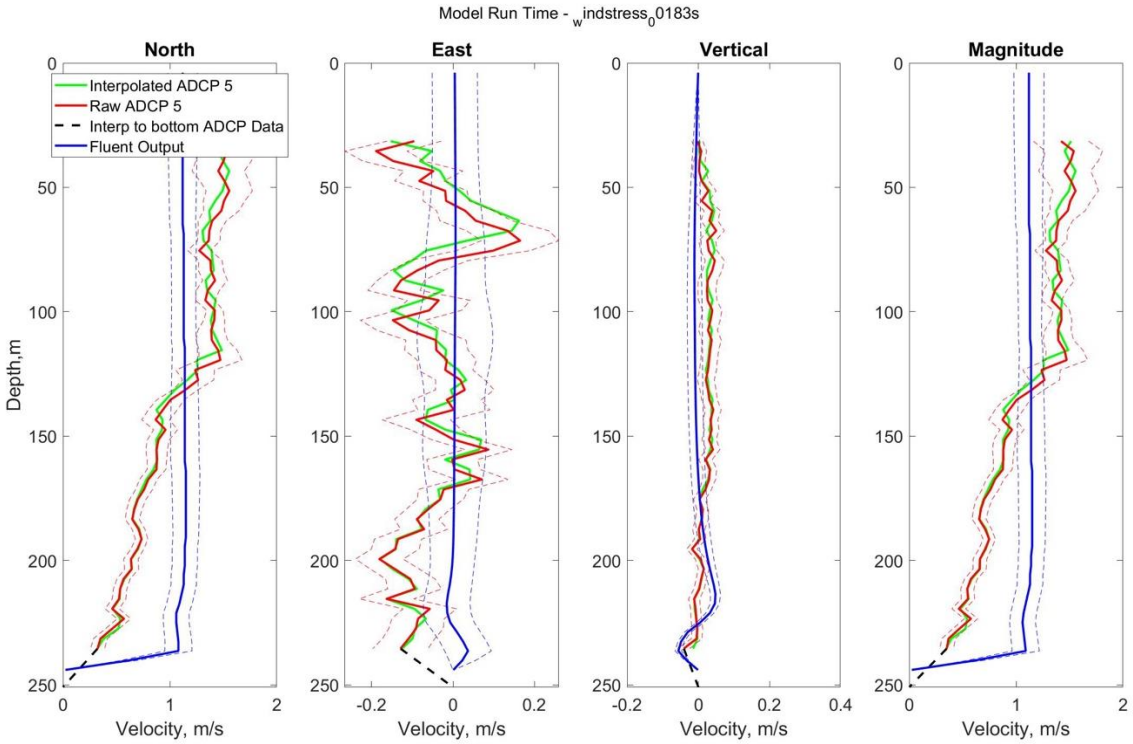

Figure 77. Comparison of North (left), East (second), vertical (third) velocity, and velocity magnitude (right) components between the ADCP field data and model output at 183 seconds of flow time.

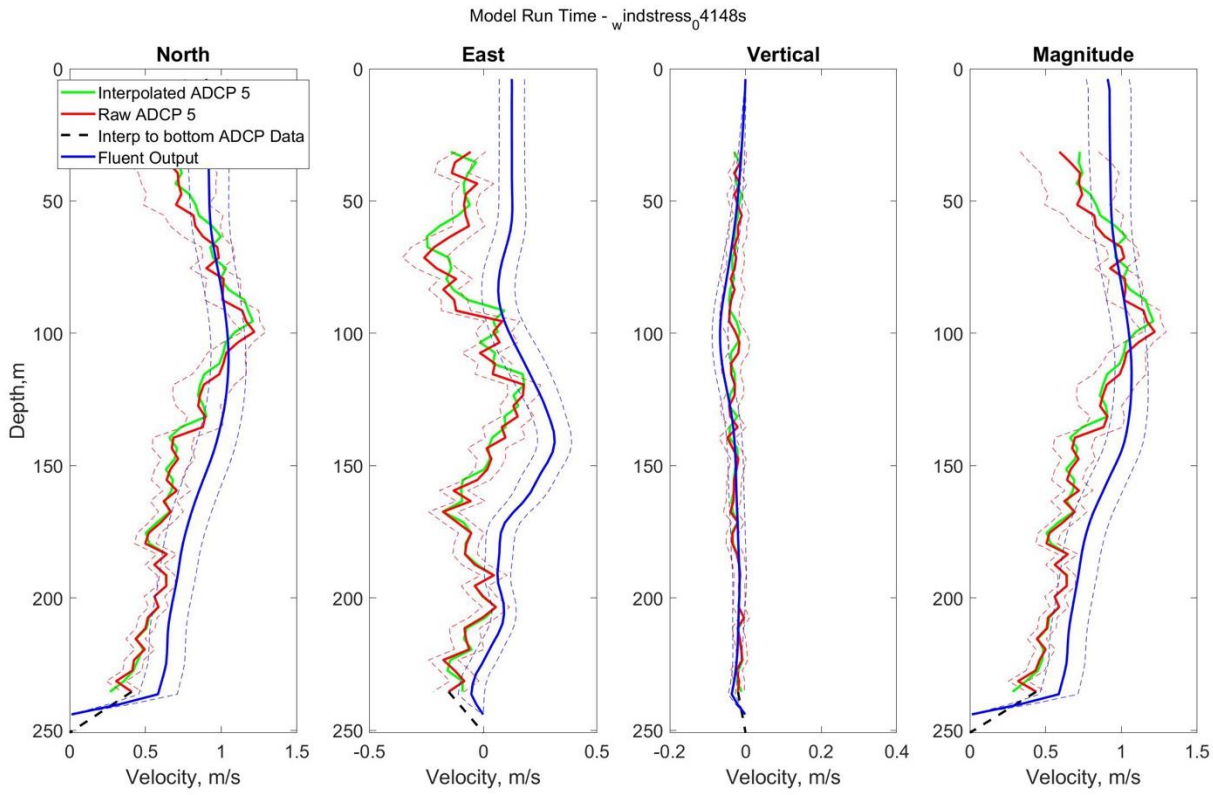

Figure 78. Comparison of North (left), East (second), vertical (third) velocity, and velocity magnitude (right) components between the ADCP field data and model output at 4148 seconds of flow time.

According to the results of the comparison shown in Figure 79, the model compares well with the ADCP data from the field experiment. The model output varies from the field data below a depth of ~100 m, specifically in the North velocity component and velocity magnitude, which is due to very strong variability of the velocity field in the western boundary current. In fact, the overlapping model and field data standard deviations (dashed lines in Fig. 79) show that the model and data are, in general, consistent within the limited area. The model has good predictive skills in the challenging environment of a strong western boundary current and is potentially able to cover the range of ocean features from small-scales to sub-mesoscales.

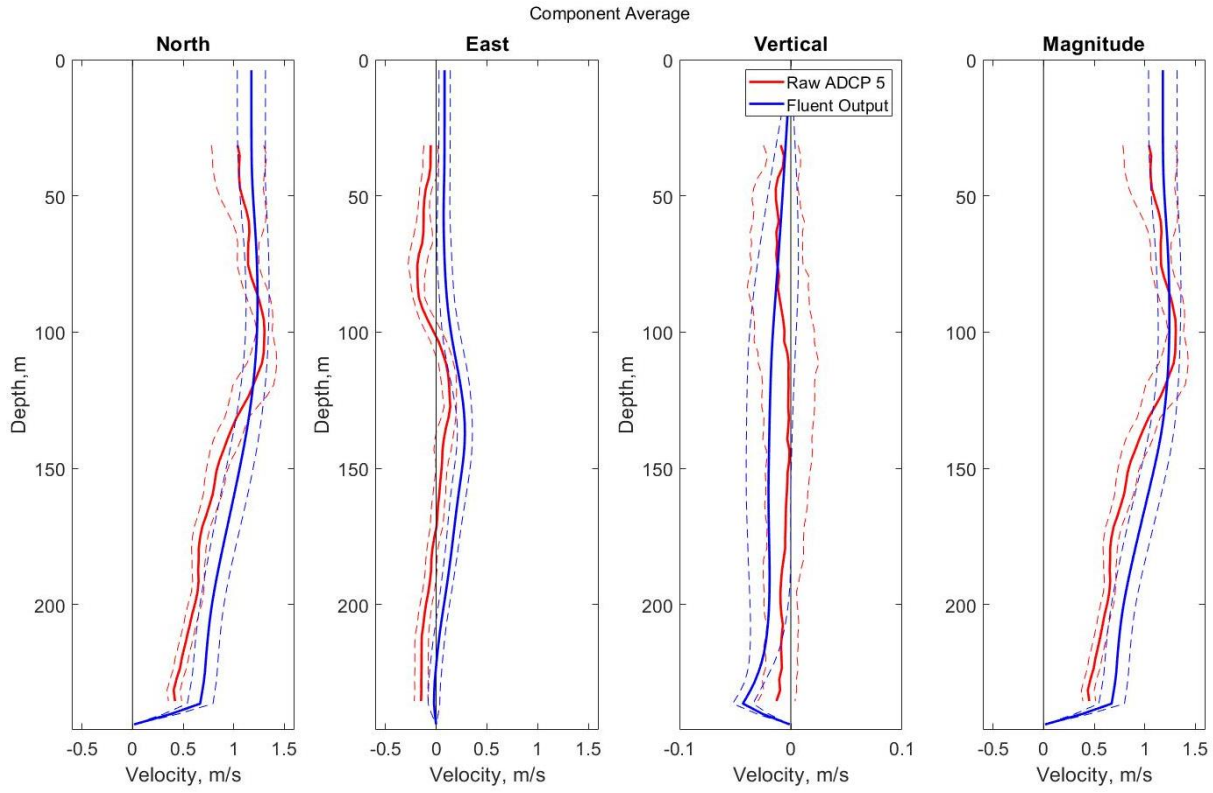

Figure 79. Comparison of North (left), East (second), vertical (third) velocity, and velocity magnitude (right) components between the ADCP field data and model output.

Runs of the model using temperature from the CTD were completed and are not shown as model refinement is still required. When initializing the model with temperature data and setting density as a function of temperature, backflow at the outlet caused distortion within the model domain due to tidal motions and internal waves.

Model run with air layer

To account for tidal variations and internal waves, a free-surface was incorporated into our model, which allowed for more realistic modeling of currents. The setup of the model, using the domain shown in Figure 75, included the same setup as the model without an air layer (Fig. 74), except with an additional phase (air) in our Volume of Fluid model, which was used for the VOF-to-DPM tropical cyclone models. The setup can be seen in Figure 80, showing a north velocity contour in the center of the domain, the water volume shown in blue, and the seafloor in grey.

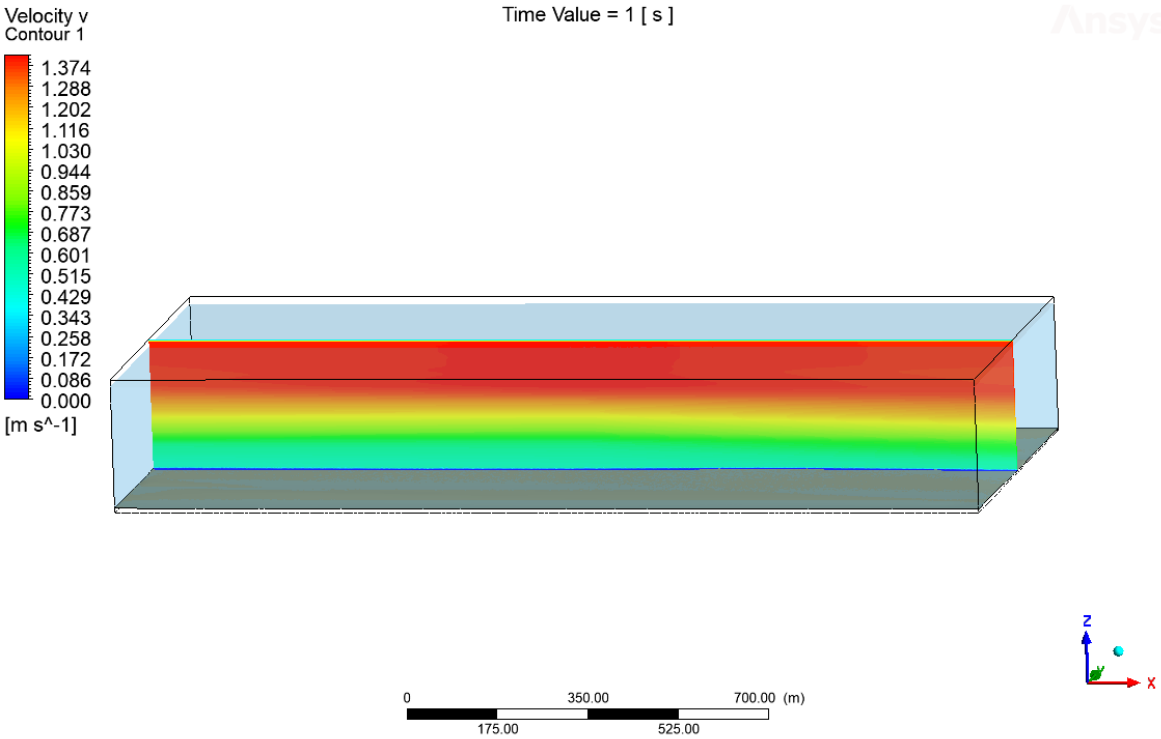

Figure 80. Model initialization with ADCP data and the water layer shown in blue.

As the model ran, it was qualitatively difficult to ensure that the volume of water was changing within the model, as the tidal fluctuations were very small in comparison to the model domain size. To verify, the average volume of water in the domain was calculated and plotted throughout the model run (Fig. 81). We can clearly see the tidal variation as the model progresses and the ADCP velocities are continuously updated within the model.

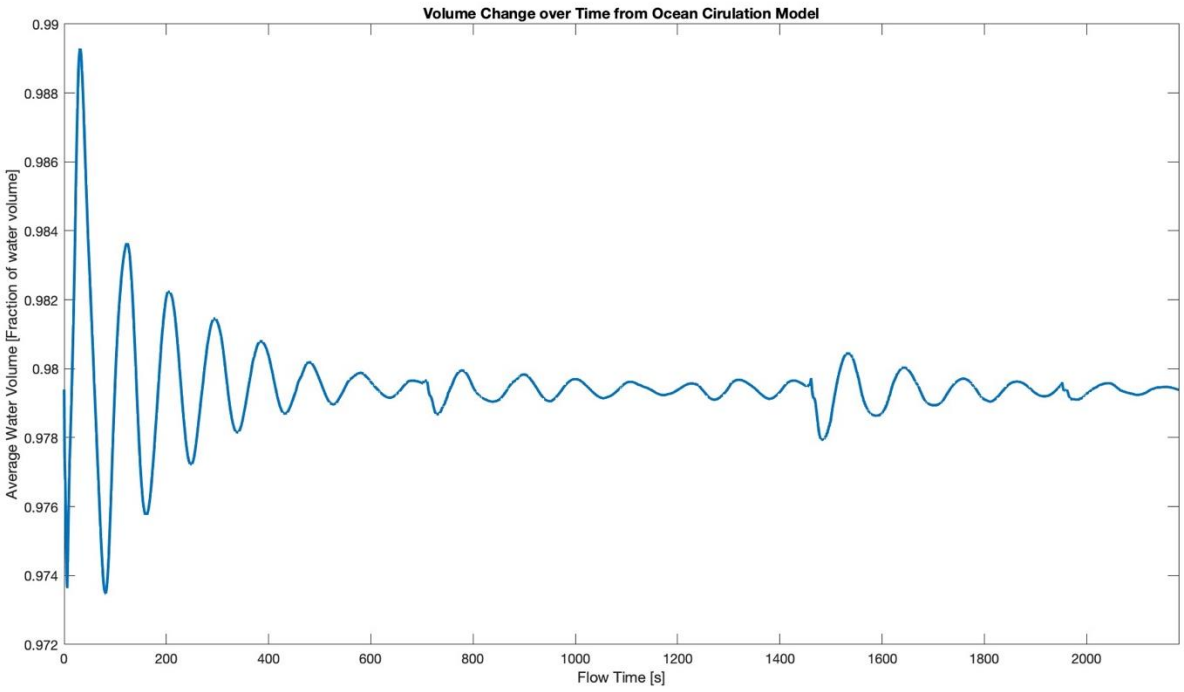

Figure 81. The variation in water volume with tidal fluctuations as the model runs.

In the VOF-to-DPM tropical cyclone models, ANSYS Fluent's dynamic mesh adaption was key to the success of the model. To further enhance the ocean circulation model, this technique was also applied but using different variables. The mesh adaption was set to focus on areas of interest, which for this model were the shear stress within the fluid domain and the wall shear stress near the wall boundaries (seafloor). Figure 82 shows a contour of a plane within the domain with the mesh grid (white) overlaid on it. This shows that the mesh was refining in areas of higher shear stress within the fluid. Figure 83 shows a contour of wall stress near the seafloor boundary in the model with the mesh grid (white), showing refinement where wall stress was higher.

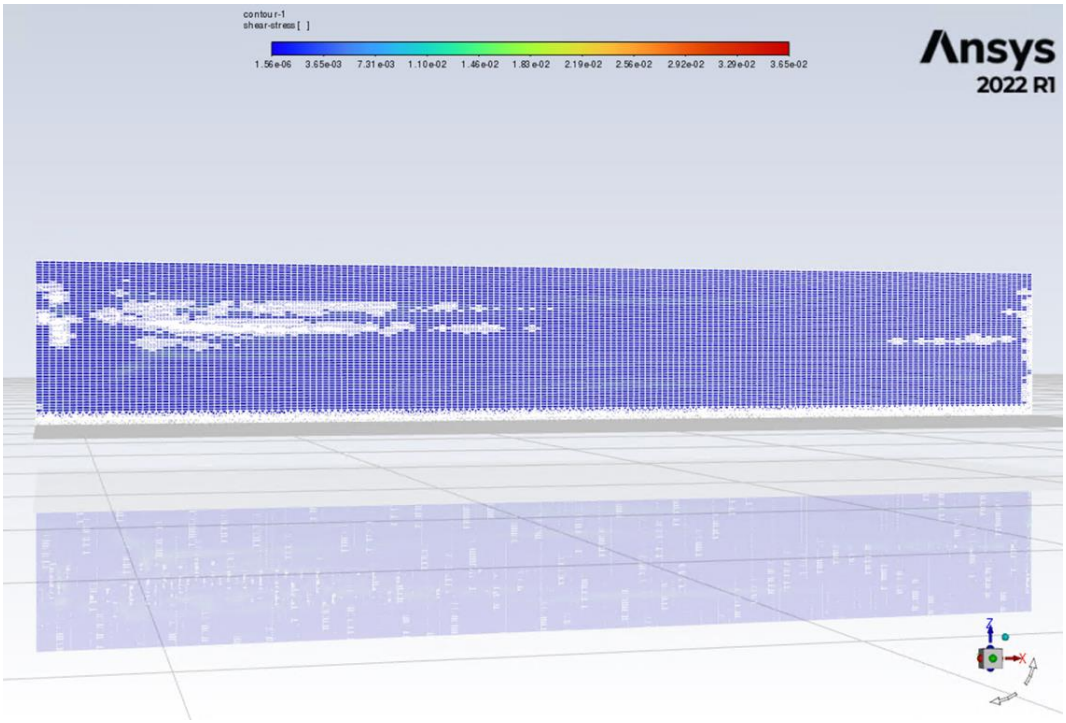

Figure 82. Mesh adaption according to shear stress within the fluid.

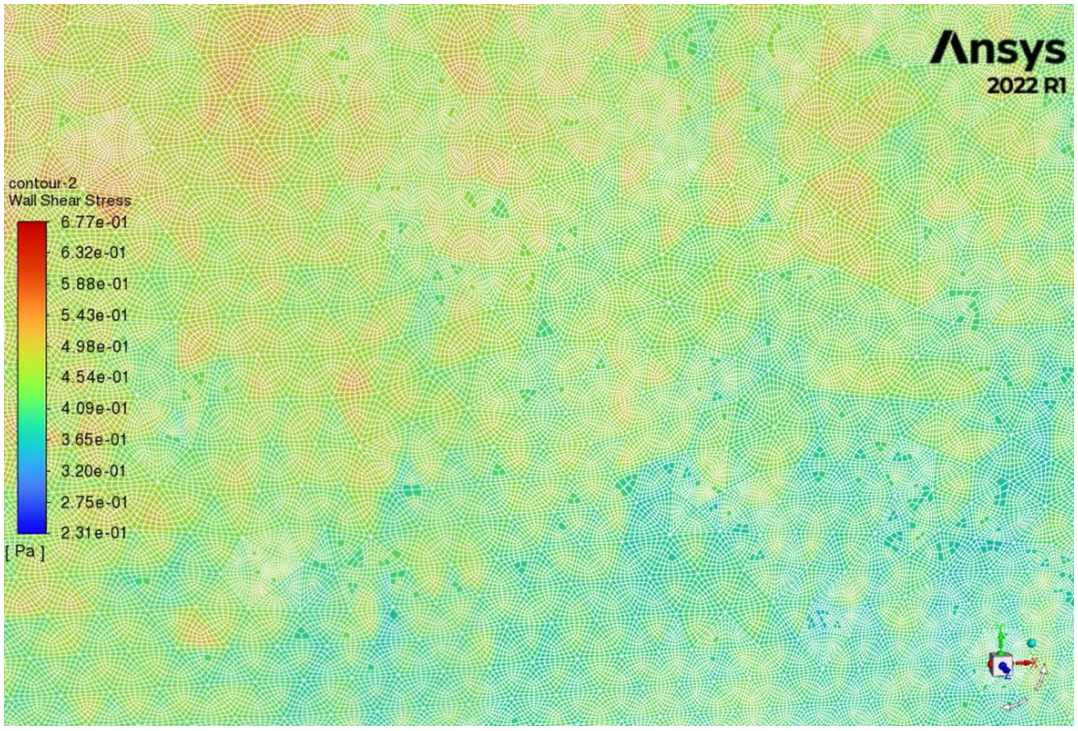

Figure 83. A visual of mesh adaption, set to adapt to wall shear, on the seafloor of the model.

To verify that implementing mesh adaption in this model was effective to the simulation results, the subgrid-scale viscosity was analyzed after running the model for an hour of flow time. The subgrid-scale modeling represents small-scale processes that take place below length scales resolved in the normal computational mesh (see more details in Section 3). Enhancing the mesh resolution using dynamic mesh adaption can assist in resolving fine-scale processes with the available computational power, and therefore yield better results for small to mesoscale processes. The subgrid turbulent viscosity is shown in the center of the domain in Figure 84. Subgrid simply means what is being modeled below the models mesh resolution. Since the mesh adapts to smaller cell sizes when implemented, subgrid scale viscosity may be less when mesh adaption is included in the model, as seen in Figure 84a and b. While there is less subgrid scale resolution, that is because the previous subgrid turbulence is now accounted for directly rather than simulated as subgrid, leading to more fine resolution results, as shown in the example of the vertical velocity in the model (Fig. 84c and d). Wall shear near the seafloor of the domain was also increased using mesh adaption, as shown in Figure 85, which yields finer resolution results in the boundary layer near the seafloor of this model.

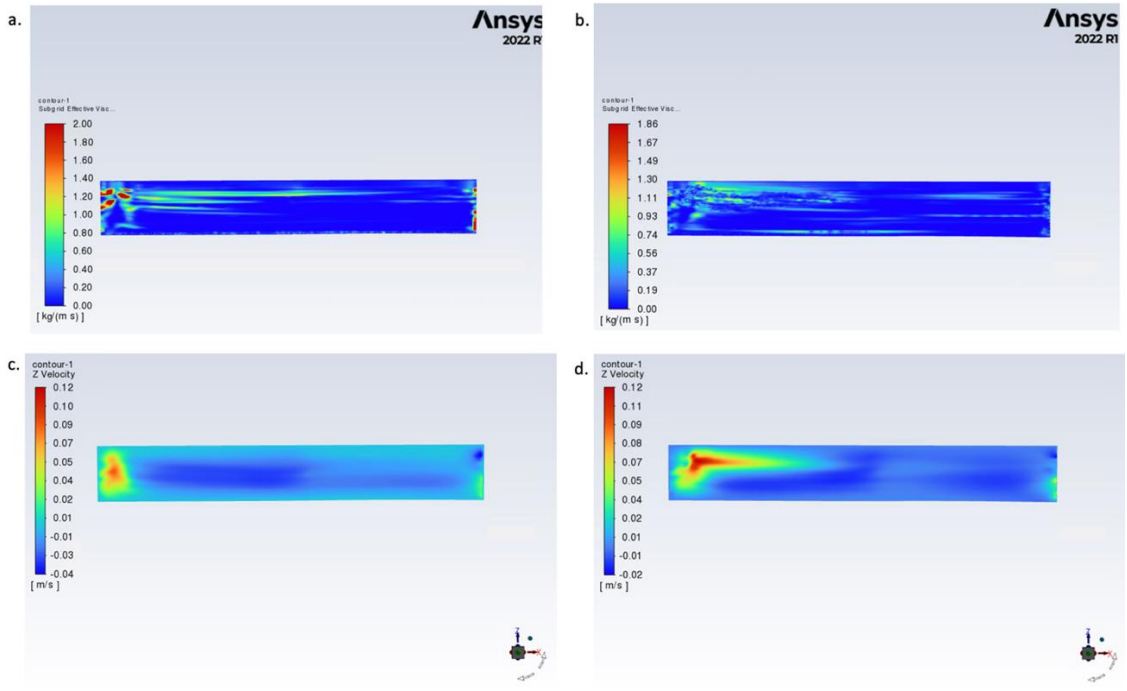

Figure 84. Subgrid turbulent viscosity vertically in the center of the domain after 3050 seconds of flow time (a) without and (b) with mesh adaption implemented into the model. Vertical velocity on the same plane (c) with and (d) without mesh adaption.

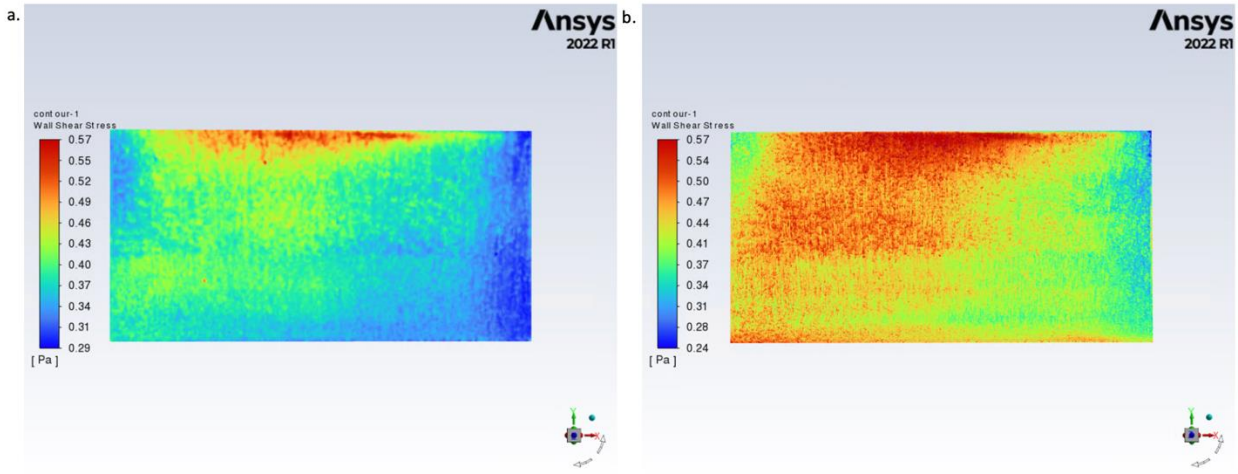

Figure 85. Wall shear just above the seafloor after 3050 seconds of flow time (a) without and (b) with mesh adaption implemented into the model.

In application to tropical cyclone dynamics, there is difficulties in understanding conditions within the upper ocean before, during, and after storm passage to areas, especially those difficult to characterize such as a western boundary current like the Gulf Stream. A model such as the one described here can assist in understanding and characterizing ocean characteristics and dynamics that may attribute to tropical cyclone intensity and formation. Once stratification is implemented into the model, realistic sea surface and upper ocean temperatures and salinity will be simulated, which are both important to understand for tropical cyclone rapid intensification. Importantly, implementing tropical cyclone winds into a larger air layer in this model could assist in understanding the impact of storms on the upper ocean mixing and circulation. Tropical cyclones increase kinetic energy into waves and currents at the surface, leading to mixing and turbulence in the upper ocean (Liu et al. 2008). Heat uptake by the ocean can also be affected by tropical cyclones and may impact the global ocean transport of heat. After the storm passes, the response in the upper ocean will decay over days to weeks through dispersion and wave propagation (Gill, 1984; Park et al., 2009; Chen et al., 2014). Tropical cyclones do not only affect the upper ocean, as their effects can reach the layers near the seafloor, altering sediment transport and turbidity (Larcombe & Carter, 2004; Galewsky et al., 2006; Liu et al., 2012; Hearn & Holloway, 1990; Drost et al., 2017). Implementing a regional model in a western boundary current to understand

impacts of tropical cyclones on small to mesoscale circulation and stratification could be useful to understand potential effects on the ocean regionally and globally.

8.2.a. Internal wave soliton breaking on the South Florida shelf

An additional model, based on the Dean (2018) internal wave model, was run to characterize internal waves in the same area as the model in Section 8.2. The internal wave soliton model is qualitatively consistent with observations on the Southeast Florida shelf. The domain in Figure 86 is 3000 m long, 800 m wide, 100 m deep on the west shallow end, and 250 m deep on the east deep end (offshore). There was a continuous slope representing the continental slope on the Southeast Florida shelf.

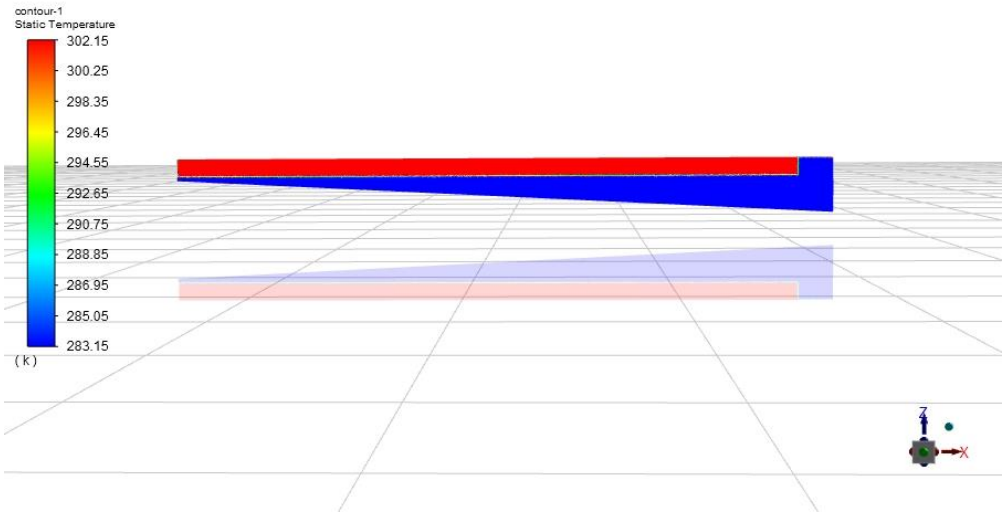

Figure 86. Initial temperature / density anomaly is created to generate an internal wave soliton.

The model was run for a total flow time of 72 minutes, after which the internal wave soliton had broken on the continental slope. Contours of the wave's turbulent viscosity are shown in Figure 87 (at 1420 s flow time) and Figure 88 (2882 s flow time).

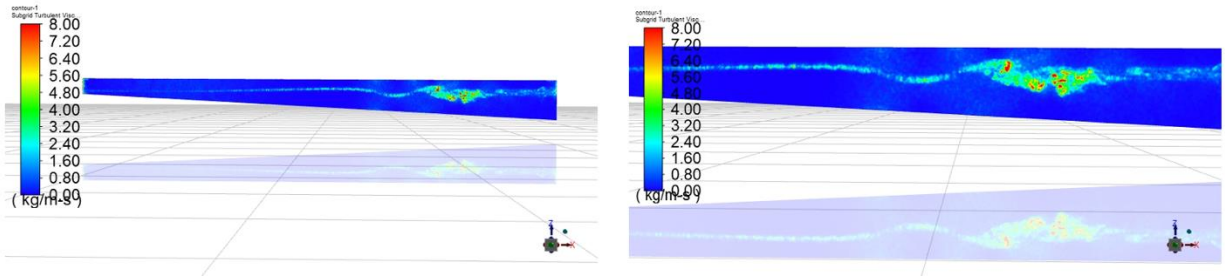

Figure 87. An internal wave's turbulent viscosity in 3000 m long domain at 1420 seconds of flow time.

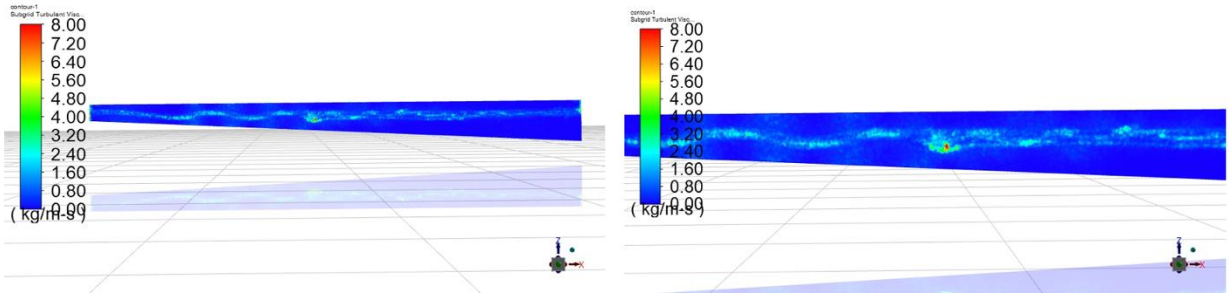

Figure 88. An internal wave's turbulent viscosity in 3000 m long domain at 2882 seconds of flow time.

The wave's temperature and velocity are shown in Figure 89 at flow times of 24, 48, and 72 minutes as the wave crashed onto the continental shelf. An iso-surface of 295 K is also displayed, which shows the microstructure of the wave front.

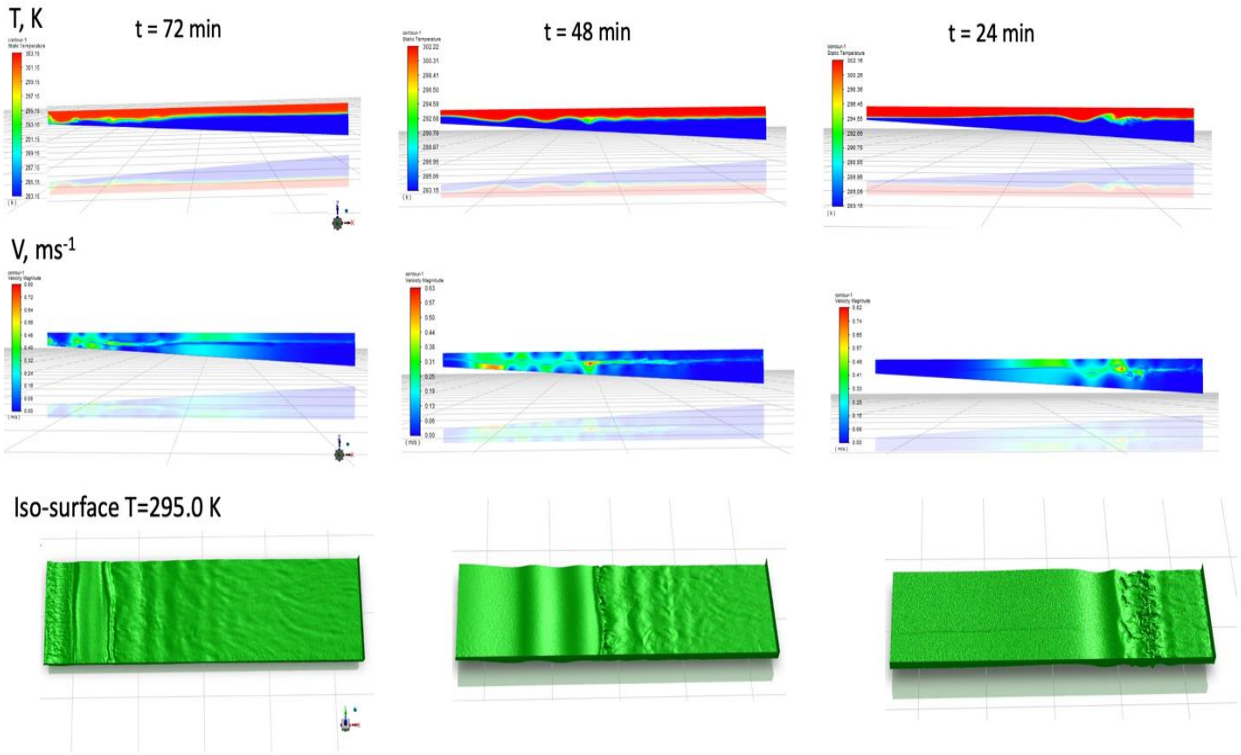

Figure 89. Internal wave soliton modeling of a slope representing the Southeast Florida shelf.

This model further enhances the larger ocean circulation model and allows us to characterize ocean processes using CFD software.

9. Conclusions

Aiming to enhance forecasting accuracy, this dissertation assesses the complex processes and interactions in the ocean water column and at the air-sea interface under tropical cyclone conditions using a combination of CFD model results validated with laboratory experiments and field observations. Based on the results of Vanderplow (2020), surfactants increase the overall abundance of spray particles under tropical cyclone winds. In this work, a sea spray generation function (SSGF) was calculated from the computational fluid dynamics model that allows for realistic, real-time, spray droplet formation and tracking. With increasing tropical cyclone winds, the SSGF increased, and when surfactants were present the SSGF was higher in Category 1, 2, and 3 conditions. After Category 3 tropical cyclone conditions, there was little to no difference between the SSGF for surfactant and nonsurfactant cases, suggesting a lack of dependence on

surface tension at such high winds. These results align with Emanuel (2003), Krall et al. (2019), Jähne (2019), and visual observations, which agree that under extreme wind conditions, there is a change in regime at the air-sea interface. This finding reinforces the need for an enhanced understanding and parameterization of the underlying physics in existing forecast models to improve the accuracy of tropical cyclone intensity predictions.

The existing tropical cyclone spray model results can also yield implications for heat, momentum, and gas fluxes at the air-sea interface. While the proposed modeling of heat and momentum fluxes proved difficult during the span of this dissertation work, applying similar formulations for spray fluxes as in Barr et al. (2023) into the VOF-to-DPM and DPM-to-VOF model in future work would greatly enhance the overall research in the direction of fully understanding spray and spume fluxes, distributions, and the impact of surfactants in relation to tropical cyclone intensity. Additionally, implementing the modeled SSGF into larger forecasting models could also provide insight into heat and momentum fluxes under various tropical cyclone conditions. Previous work by Krall et al. (2019) and Jähne (2019) found that above 33 m s^{-1} a new gas transfer regime is established, which we also see in our numerical modeling. In the consideration of surfactant effects on gas transfer under extremely high winds in this dissertation work, the effect of surfactants on air-sea gas transfer is still unclear. The presence of surfactants increases air-sea gas exchange velocity proportional to the volume flux of sea spray. Based on the considerations of Andreas et al. (2017), the interfacial time scale of spray droplets is very small and has little effect on gas transfer. Surfactants may increase the internal mixing time scale for spray droplets, which would result in a reduction of the gas transfer velocity. Taking these factors into consideration, the total effect of surfactants on spray-mediated gas transfer remains uncertain.

Additionally in this work, a nonhydrostatic modeling approach for three-dimensional simulation of ocean circulation in a strong western boundary current in the range from small-scales to sub-mesoscales was developed, which has been verified with field data from the Straits of Florida. A model such as the one described here can assist in understanding and characterizing ocean characteristics and dynamics that may attribute to tropical cyclone intensity and formation, as well as could be applied to understand impacts of the storm on the upper ocean.

In conclusion, this body of work significantly advances our understanding of the complex dynamics at below ant at the air-sea interface during tropical cyclones, offering pathways for

refining forecasting models to improve intensity forecasting and better prepare coastal communities.

10. Future Considerations

While this work has improved understanding of poorly understood, complex, phenomena related to tropical cyclone intensity, there are significant ways the work can be improved in future research:

1. Increasing the domain of the VOF-to-DPM spray generation model from the results shown here will further refine these findings and yield more realistic conditions and SSGFs.
2. Understanding the concentration and distribution of surfactants in the world ocean better will assist in more realistic modeling of the influence of surfactants and the application of satellite oceanography as a proxy for surfactants.
3. Implementing the secondary breakup model of spray droplets within the VOF-to-DPM will provide more accurate spray diameters, distributions, and SSGFs.
4. Continuing the implementation of the heat and momentum fluxes into the VOF-to-DPM spray model will provide critical results to understanding evaporative cooling and contributions of spray to sensible and latent heat fluxes into tropical cyclones that are difficult to study in the field and laboratory settings.
5. Additionally, implementing the DPM-to-VOF model will allow for successful modeling of re-entrant spray, which contribute significantly to the spray enthalpy flux.
6. Using the species transfer model within ANSYS Fluent to simulate gas transfer of various gasses in combination with the VOF-to-DPM model and better understand surfactant impacts on air-sea gas exchange under high winds.
7. Understanding the effects of rain on tropical cyclone intensity and the complex interaction with spray, surfactants, and fluxes is a critical component in this research and should be addressed in future work.
8. Follow Todd et al. (2018) and use Slocum G3 gliders in the Gulf Stream before/during/after the passage of tropical cyclones to get characterization of small to

mesoscale circulation and flow. The physical oceanography laboratory also has oceanographic data that could prove useful before/during/after storm passage.

11. Acknowledgements

I am forever grateful for my friends and family that have gotten me through the most challenging endeavor of my life thus far, and to my dog, Miso, with whom I have truly an unspeakable and unexplainable bond and has been my largest source of emotional support during my worst moments. My colleagues and friends Megan and Alfredo have made me laugh in my darkest times, supported me in the lab and outside of it, and pushed me to succeed even when I thought I couldn't.

Thank you to Dr. Alexander Soloviev, my major advisor, for his assistance and mentorship during my PhD, as well as the opportunities he provided that allowed me to complete this research and present the results at national and international conferences and workshops. Thank you as well to my committee members, Dr. Brian Haus, Dr. Isaac Ginis, and Dr. Richard Dodge, for their continued support my project and the time they all committed to reviewing my research and providing comprehensive exams. I am extremely grateful for the ideas and discussion from Dr. Kerry Emanuel and Dr. Roger Lukas, who were pioneers in the importance of microphysics and of the two-phase environment at the air-sea interface. I am also grateful to John Kluge and Dr. Cayla Dean for their contributions to this dissertation work and assistance in the lab. I am appreciative of the entire Physical Oceanography Laboratory team, Johanna Evans at SFOMF, Jon Wood at Ocean Data Technologies, Inc., and the crews of the M/V Becker and M/V Go America, who I couldn't have done this without. This dissertation work was supported by the Gulf of Mexico Research Initiative (GoMRI) Award S120021: "Consortium for Advanced Research on Transport of Hydrocarbon in the Environment (CARTHE)", NOAA Award NA15OAR4310173, and ONR Awards N00014-18-1-2835, N00014-21-1-4007, N00014-22-1-2008, N00014-23-1-2270, and N0014-23-1-2746. Any opinions, findings and conclusions or recommendations expressed in this material are those of the author(s) and do not necessarily reflect the views of the U.S. Navy. The views expressed in this dissertation are those of the author and do not necessarily reflect the official policy or position of the Department of the Navy, Department of Defense, nor the U.S. Government.

12. Publications

Vanderplow, B., Soloviev, A.V., Dean, C.W. et al. (2020). Potential effect of bio-surfactants on sea spray generation in tropical cyclone conditions. *Sci. Rep*. 10, 19057. https://doi.org/10.1038/s41598-020-76226-8.

Vanderplow, B., Soloviev, A.V., & Sami, M. (2023). Sea spray generation under tropical cyclone conditions in the presence of surfactants and implications for air-sea gas exchange. *Cross-linking lab and field measurements and numerical modeling to identify and quantify the mechanisms of air-sea gas transfer*. In review.

Vanderplow, B., Kluge, J.A., Soloviev, A.V., et al. (2023). Measurement and modeling of small-scale to mesoscale features in a western boundary current. Submitted to *Ocean Modeling*.

Vanderplow, B., Soloviev, A.V. (2024). A modeled sea spray generation function under high winds. In preparation.

13. References

Alpers, W., & Espedal, H. A. (2004). Oils and surfactants. In C.R. Jackson & J.R. Apel (Eds.), *Synthetic aperture radar marine user's manual* (pp. 263–276). National Oceanic and Atmospheric Adminiatration. https://repository.library.noaa.gov/view/noaa/1118.

Andreas, E.L. (1992). Sea spray and the turbulent air-sea heat fluxes. *Journal of Geophysical Research, 9*(C7), 11429-11441. https://doi.org/10.1029/92JC00876.

Andreas, E.L. (1989). *Thermal and size evolution of sea spray droplets*. Cold Regions Research and Engineering Laboratory. https://apps.dtic.mil/sti/pdfs/ADA210484.pdf.

Andreas, E. L. (1998). A new sea spray generation function for wind speeds up to 32 ms^{-1}. *Journal of Physical Oceanography, 28*(11), 2175-2184. https://doi.org/10.1175/1520-0485(1998)028<2175:ANSSGF>2.0.CO;2.

Andreas, E. L. (2002). A review of the sea spray generation function for the open ocean. *Advances in Fluid Mechanics, 33*, 1-46.

Andreas, E. L. (2004). Spray stress revisited. *Journal of Physical Oceanography, 34*(6), 1429-1440. https://doi.org/10.1175/1520-0485(2004)034<1429:SSR>2.0.CO;2.

Andreas, E. L., & Emanuel, K. A. (2001). Effects of sea spray on tropical cyclone intensity. *Journal of the Atmospheric Sciences, 58*(24), 3741-3751. https://doi.org/10.1175/1520-0469(2001)058<3741:EOSSOT>2.0.CO;2.

Andreas, E. L., & Mahrt, L. (2016). On the prospects for observing spray-mediated air–sea transfer in wind–water tunnels. *Journal of the Atmospheric Sciences, 73*(1), 185-198. https://doi.org/10.1175/JAS-D-15-0083.1.

Andreas, E., Vlahos, P., & Monahan, E. (2017). Spray-mediated air-sea gas exchange: The governing time scales. *Journal of Marine Science, 5*, 60. https://doi.org/10.3390/jmse5040060.

ANSYS Fluent Theory Guide 2022R1. (2022). ANSYS, Inc. https://ansyshelp.ansys.com/account/secured?returnurl=/Views/Secured/corp/v221/en/flu_tg/flu_tg.html%23flu_tg.

Asher, W. E., Karle, L., Higgings, B., Farley, P., Sherwood, C., Gardiner, W., Wanninkhof, R., Chen, H., Lantry, T., Steckley, M., Monohan, E., Wan, Q., & Smith, P. (1995). Measurement of gas transfer, whitecap coverage, and brightness temperature in a surf pool: An overview of WABEX-93. In B. Jähne & E. Monahan (Eds.), *Air-water gas transfer, selected papers, 3rd international symposium on air-water gas transfer* (pp. 205–216). AEON Verlag & Studio. https://www.osti.gov/servlets/purl/97107.

Asher, W. E., Karle, L. M., Higgins, B. J., Farley, P. J., Monahan, E. C., & Leifer, I. S. (1996). The influence of bubble plumes on air seawater gas transfer velocities, *Journal of Geophysical Research, 101*, 12027– 12041. https://doi.org/10.1029/96JC00121.

Bai, Y. (2019). *Visible Infrared Imaging Radiometer Suite (VIIRS).*" National Oceanic and Atmospheric Administration. https://ncc.nesdis.noaa.gov/VIIRS/.

Bao, J.W., Fairall, C. W., & Michelson, S. A. (2017). *Evaluation and improvement of spray-modified air-sea enthalpy and momentum flux parameterizations for operational hurricane prediction*. NOAA Earth System Research Laboratory. https://www.researchgate.net/profile/Chris-Fairall/publication/252649159_Evaluation_and_Improvement_of_Spray-Modified_Air-Sea_Enthalpy_and_Momentum_Flux_Parameterizations_for_Operational_Hurricane_Prediction/links/0c9605374ce76439a8000000/Evaluation-and-Improvement-of-Spray-Modified-Air-Sea-Enthalpy-and-Momentum-Flux-Parameterizations-for-Operational-Hurricane-Prediction.pdf.

Bao, J. W., Fairall, C. W., Michelson, S. A., & Bianco, L. (2011). Parameterizations of sea-spray impact on the air–sea momentum and heat fluxes. *Monthly Weather Review, 139*(12), 3781-3797. https://doi.org/10.1175/MWR-D-11-00007.1.

Bao, J.W., Wilczak, J. M., Choi, J.K., & Kantha, L. H. (2000). Numerical simulations of air–sea interaction under high wind conditions using a coupled model: A study of hurricane development. *Monthly Weather Review, 128*, 2190–2210. https://doi.org/10.1175/1520-0493(2000)128<2190:NSOASI>2.0.CO;2.

Banner, M. L., & Phillips, O. M. (1974). On the incipient breaking of small-scale waves. *Journal of Fluid Mechanics, 65*, 647– 656. doi:10.1017/S0022112074001583.

Barnes, G. M. (2006). Thermodynamic structure of a hurricane's lower cloud and subcloud layers. *27th Conference on hurricanes and tropical meteorology*. American Meteorological Society. https://ams.confex.com/ams/27Hurricanes/techprogram/paper_107927.htm.

Barr, B. W., Chen, S. S., & Fairall, C. W. (2023). Sea-state-dependent sea spray and air–sea heat fluxes in tropical cyclones: A new parameterization for fully coupled atmosphere–wave–ocean models. *Journal of the Atmospheric Sciences, 80*(4), 933-960. https://doi.org/10.1175/JAS-D-22-0126.1.

Bell, M. M., Montgomery, M. T., & Emanuel, K. A. (2012). Air-sea enthalpy and momentum exchange at major hurricane wind speeds observed during CBLAST. *Journal of the Atmospheric Sciences, 69*(11), 3197-3222. https://doi.org/10.1175/JAS-D-11-0276.1.

Bhatia, K. T., Vecchi, G. A., Knutson, T. R., Murakami, H., Kossin, J., Dixon, K. W., & Whitlock, C. E. (2019). Recent increases in tropical cyclone intensification rates. *Nature Communications, 10*(1), 1-9. https://doi.org/10.1038/s41467-019-08471-z.

Bianco, L., Bao, J.W., Fairall, C. W., & Michelson, S. A. (2011). Impact of sea spray on the surface boundary layer. *Boundary Layer Meteorology*, 140. https://doi.org/10.1007/s10546-011-9617-1.

Black, P. G., D'Asaro, E. A., Drennan, W. M., French, J. R., Niiler, P. P., Sanford, T. B. & Zhang, J. A. (2007). Air–sea exchange in hurricanes: Synthesis of observations from the coupled boundary layer air–sea transfer experiment. *Bulletin of the American Meteorological Society*, *88*(3), 357-374. https://doi.org/10.1175/BAMS-88-3-357.

Blanchard, D. C. (1963). The electrification of the atmosphere by particles from bubbles in the sea. *Progress in Oceanography, 1*, 73-202. https://doi.org/10.1016/0079-6611(63)90004-1.

Bock, E. J., Hara, T., Frew, N.M., & McGillis, W.R. (1999). Relationship between air-sea gas transfer and short wind waves. *Journal of Geophysical Research*, *104*(25), 821–25,831. https://doi.org/10.1029/1999JC900200.

Cangialosi, J. P. (2023). *National Hurricane Center forecast verification report 2022 hurricane season*. National Hurricane Center. https://www.nhc.noaa.gov/verification/pdfs/Verification_2022.pdf.

Cartmill, J. W., & Su, M. Y. (1993). Bubble size distribution under saltwater and freshwater breaking waves. *Dynamics of Atmospheres and Oceans*, *20*(1-2), 25–31. https://doi.org/10.1016/0377-0265(93)90046-A.

Chen, G., Xue, H., Wang, D., & Xie, Q. (2013). Observed near-inertial kinetic energy in the northwestern South China Sea. *Journal of Geophysical Research: Oceans*, *118*(10), 4965-4977. ttps://doi.org/10.1002/jgrc.20371.

Chen, H., Zhang, D. L., Carton, J., & Atlas, R. (2011). On the rapid intensification of Hurricane Wilma (2005). Part I: Model prediction and structural changes. *Weather and Forecasting*, *26*(6), 885-901. https://doi.org/10.1175/WAF-D-11-00001.1.

Cipriano, R. J., Monahan, E. C., Bowyer, P. A., & Woolf, D. K. (1987). Marine condensation nucleus generation inferred from whitecap simulation tank results. *Journal of Geophysical Research: Oceans*, *92*(C6), 6569-6576. https://doi.org/10.1029/JC092iC06p06569.

Davis, C., Wang, W., Cavallo, S., Done, J., Dudhia, J., Fredrick, S., & Torn, R. (2011). High-resolution hurricane forecasts. *Computing in Science and Engineering*, *13*(1), 22-30. DOI:10.1109/MCSE.2010.74.

Dean, C. W. (2018). *Turbulent and Electromagnetic Signature of Small-and Fine-scale Biological and Oceanographic Processes*. [Doctoral Dissertation, Nova Southeastern University]. NSUWorks. https://nsuworks.nova.edu/occ_stuetd/492/.

DeMaria, M., Sampson, C. R., Knaff, J. A., & Musgrave, K. D. (2014). Is tropical cyclone intensity guidance improving? *Bulletin of the American Meteorological Society, 95*, 387–398. https://doi.org/10.1175/BAMS-D-12-00240.1.

Donelan, M. A. (2018). On the decrease of the oceanic drag coefficient in high winds. *Journal of Geophysical Research: Oceans*, *123*(2), 1485-1501. https://doi.org/10.1002/2017JC013394.

Donelan, M. A., Haus, B. K., Reul, N., Plant, W. J., Stianssnie, M., Graber, H. C., Brown, O. B., & Saltzman, E. S. (2004). On the limiting aerodynamic roughness of the ocean in very strong winds. *Geophysical Research Letters*, *31*, L18306. https://doi.org/10.1029/2004GL019460.

Drennan, W. M., Zhang, J. A., French, J. R., McCormick, C., & Black, P. G. (2007). Turbulent fluxes in the hurricane boundary layer. Part II: Latent heat flux. *Journal of the Atmospheric Sciences*, *64*(4), 1103-1115. https://doi.org/10.1175/JAS3889.1.

Drost, E. J., Lowe, R. J., Ivey, G. N., Jones, N. L., & Péquignet, C. A. (2017). The effects of tropical cyclone characteristics on the surface wave fields in Australia's North West region. *Continental Shelf Research, 139*, 35-53. https://doi.org/10.1016/j.csr.2017.03.006.

Edson, J.B., & Fairall, C.W. (1994). Spray droplet modeling. I: Lagrangian model simulation of the turbulent transport of evaporating droplets. *Journal of Geophysical Research, 99*, 25295-25311. https://doi.org/10.1029/94JC01883.

Elliott, S., Burrows, S. M., Deal, C., Liu, X., Long, M., Ogunro, O., & Wingenter, O. (2014). Prospects for simulating macromolecular surfactant chemistry at the ocean–atmosphere boundary. *Environmental Research Letters*, *9*(6), 064012. DOI:10.1088/1748-9326/9/6/064012.

Emanuel, K. A., (1986). An air-sea interaction theory for tropical cyclones. Part I. *Journal of the Atmospheric Sciences, 42*, 1062-1071. https://doi.org/10.1175/1520-0469(1986)043<0585:AASITF>2.0.CO;2.

Emanuel, K. A., (1995). Sensitivity of tropical cyclones to surface exchange coefficients and a revised steady-state model incorporating eye dynamics. *Journal of the Atmospheric Sciences, 52*, 3969-3976. https://doi.org/10.1175/1520-0469(1995)052<3969:SOTCTS>2.0.CO;2.

Emanuel, K. A., (2003), A similarity hypothesis for air–sea exchange at extreme wind speeds. *Journal of the Atmospheric Sciences*, *60*(11), 1420-1428. https://doi.org/10.1175/1520-0469(2003)060<1420:ASHFAE>2.0.CO;2.

Emanuel, K., & Zhang, F. (2016). On the predictability and error sources of tropical cyclone intensity forecasts. *Journal of the Atmospheric Sciences, 73*(9), 3739-3747. https://doi.org/10.1175/JAS-D-16-0100.1.

Ezer, T. (2018a). The increased risk of flooding in Hampton roads: On the roles of sea level rise, storm surges, hurricanes, and the Gulf Stream. *Marine Technology Society Journal, 52*(2), 34-44. https://doi.org/10.4031/MTSJ.52.2.6.

Ezer, T. (2018b). On the interaction between a hurricane, the Gulf Stream and coastal sea level. *Ocean Dynamics, 68*(10), 1259-1272. https://doi.org/10.1007/s10236-018-1193-1.

Ezer, T. (2019). Numerical modeling of the impact of hurricanes on ocean dynamics: sensitivity of the Gulf Stream response to storm's track. *Ocean Dynamics, 69*(9), 1053-1066. https://doi.org/10.1007/s10236-019-01289-9.

Ezer, T., Atkinson, L. P., & Tuleya, R. (2017). Observations and operational model simulations reveal the impact of Hurricane Matthew (2016) on the Gulf Stream and coastal sea level. *Dynamics of Atmospheres and Oceans, 80*, 124-138. https://doi.org/10.1016/j.dynatmoce.2017.10.006.

Fairall, C. W., Banner, M. L., Peirson, W. L., Asher, W., & Morison, R. P. (2009). Investigation of the physical scaling of sea spray spume droplet production. *Journal of Geophysical Research, 114*, C10001. https://doi.org/10.1029/2008JC004918.

Fairall, C. W., Edson, J. B., & Miller, M. A. (1990). Heat fluxes, whitecaps, and sea spray. In G. Geernaert & W. Plant (Eds.), *Surface Waves and Fluxes: Current Theory and Remote Sensing* (pp. 173–208) D. Reidel Publishing Company. https://link.springer.com/chapter/10.1007/978-94-009-2069-9_6.

Fairall, C.W., Kepert, J.D., & Holland, G.H. (1994). The effect of sea spray on surface energy transports over the ocean. *Global Atmosphere and Ocean System, 2*, 121-142. https://www.researchgate.net/publication/249994334_The_effect_of_sea_spray_on_surface_energy_transports_over_the_ocean.

Fairall, C. W., Pezoa, S., Moran, K., & Wolfe, D. (2014). An observation of sea-spray microphysics by airborne Doppler radar. *Geophysical Research Letters, 41*(10), 3658-3665. https://doi.org/10.1002/2014GL060062.

French, J. R., Drennan, W.M., Zhang, J.A., & Black, P.G. (2007). Turbulent fluxes in the hurricane boundary layer. Part I: Momentum flux. *Journal of the Atmospheric Sciences, 64*, 1089–1102. https://doi.org/10.1175/JAS3887.1.

Frew, N. M. (1997). The role of organic films in air-sea gas exchange. In P.S. Liss & R.A. Duce (Eds.) *The Sea Surface and Global Change* (pp. 121-172). Cambridge Univ. Press. https://doi.org/10.1017/CBO9780511525025.006.

Friedman, K. S., & Li, X. (2000). Monitoring hurricanes over the ocean with wide swath SAR. *John Hopkins APL Technical Digest*, *21*(1), 80-85. https://secwww.jhuapl.edu/techdigest/content/techdigest/pdf/V21-N01/21-01-Fried.pdf.

Fudeyasu, H., Ito, K., & Miyamoto, Y. (2018). Characteristics of tropical cyclone rapid intensification over the Western North Pacific. *Journal of Climate*, *31*(21), 8917-8930. https://doi.org/10.1175/JCLI-D-17-0653.1.

Gade, M., & Alpers, W. (1999) Using ERS-2 SAR for routine observation of marine pollution in European coastal waters. *Science of the Total Environment*, *237–238*, 441–448. https://doi.org/10.1016/S0048-9697(99)00156-4.

Galewsky, J., Stark, C. P., Dadson, S., Wu, C. C., Sobel, A. H., & Horng, M. J. (2006). Tropical cyclone triggering of sediment discharge in Taiwan. *Journal of Geophysical Research: Earth Surface*, *111*(F3). https://doi.org/10.1029/2005JF000428.

Gall, J. S., Frank, W. M., & Kwon, Y. (2008). Effects of sea spray on tropical cyclones simulated under idealized conditions. *Monthly Weather Review*, *136*(5), 1686-1705. https://doi.org/10.1175/2007MWR2183.1.

Garg, N., Ng, E.Y.K., & Narasimalu, S. (2018). The effects of sea spray and atmosphere–wave coupling on air–sea exchange during a tropical cyclone. *Atmospheric Chemistry and Physics, 18*, 6001–6021, https://doi.org/10.5194/acp-18-6001-2018.

Gill, A. E. (1984). On the behavior of internal waves in the wakes of storms. *Journal of physical oceanography*, *14*(7), 1129-1151. https://doi.org/10.1175/1520-0485(1984)014<1129:OTBOIW>2.0.CO;2.

Gopalakrishnan, S. G., Goldenberg, S., Quirino, T., Zhang, X., Marks Jr, F., Yeh, K. S., & Tallapragada, V. (2012). Toward improving high-resolution numerical hurricane forecasting: Influence of model horizontal grid resolution, initialization, and physics. *Weather Forecast.*, *27*(3), 647-666. https://doi.org/10.1175/WAF-D-11-00055.1.

Graham, S. (2019). *Aqua Earth-observing satellite mission*. National Aeronautics and Space Administration. https://aqua.nasa.gov/.

Grodsky, S. *et al.* (2012). Haline hurricane wake in the Amazon/Orinoco plume: AQUARIUS/SACD and SMOS observations. *Geophysical Research Letters, 39*. https://doi.org/10.1029/2012GL053335.

Gutiérrez-Loza, L., Nilsson, E., Wallin, M. B., Sahlée, E., & Rutgersson, A. (2022). On physical mechanisms enhancing air–sea CO2 exchange. *Biogeosciences*, *19*(24), 5645-5665. https://doi.org/10.5194/bg-19-5645-2022.

Haines, M. A., & Johnson, B. D. (1995). Injected bubble populations in seawater and fresh water measured by a photographic method. *Journal of Geophysical Research, 100*, 7057–7068. https://doi.org/10.1029/94JC03226.

Harb, C., & Foroutan, H. (2019). A systematic analysis of the salinity effect on air bubbles evolution: Laboratory experiments in a breaking wave analog. *Journal of Geophysical Research: Oceans*, *124*(11), 7355-7374. https://doi.org/10.1029/2019JC015337.

Haus, B. K., Jeong, D., Donelan, M. A., Zhang, J. A., & Savelyev, I. (2010). Relative rates of sea-air heat transfer and frictional drag in very high winds. *Geophysical Research Letters*, *37*(7). https://doi.org/10.1029/2009GL042206.

Hearn, C. J., & Holloway, P. E. (1990). A three-dimensional barotropic model of the response of the Australian North West Shelf to tropical cyclones. *Journal of Physical Oceanography*, *20*(1), 60-80. https://doi.org/10.1175/1520-0485(1990)020<0060:ATDBMO>2.0.CO;2.

Hoepffner, J., Blumenthal, R., Zaleski, S. (2011). Self-similar wave produced by local perturbation of the Kelvin-Helmholtz shear-layer instability. *Physical Review Letters*, *106*, 104502-1–104502-4. DOI:10.1103/PhysRevLett.106.104502.

Holland, G. J., (1997). The maximum potential intensity of tropical cyclones. *Journal of Atmospheric Science*, *54*, 2519–2541. https://doi.org/10.1175/1520-0469(1997)054<2519:TMPIOT>2.0.CO;2.

Holthuijsen, L. H., Powell, M. D., & Pietrzak, J. D. (2012). Wind and waves in extreme hurricanes. *Journal of Geophysical Research: Oceans*, *117*(C9). https://doi.org/10.1029/2012JC007983.

Iida, N., Toba, Y. & Chaen, M. (1992). A new expression for the production rate of sea water droplets on the sea surface. *Journal of Oceanography*, *48*, 439–460. https://doi.org/10.1007/BF02234020.

Iwano, K., Takagaki, N., Kurose, R., & Komori, S. (2013). Mass transfer velocity across the breaking air-water interface at extremely high wind speeds, *Tellus B: Chemical and Physical Meteorology*, *65*, 21341. https://doi.org/10.3402/tellusb.v65i0.21341.

Jähne, B. (2009). Air–sea gas exchange. In *Elements of Physical Oceanography: A Derivative of the Encyclopedia of Ocean Sciences* (pp. 160-169). Elevier.

Jähne, B. (2019). Air-Sea Gas Exchange. In J.K. Cochran, H.J. Bokuniewicz, & P.L. Yager (Eds.) *Encyclopedia of Ocean Sciences* (pp. 1-13). Academic Press.

Jarosz, E., Mitchell, D. A., Wang, D. W., & Teague, W. J. (2007). Bottom-up determination of air-sea momentum exchange under a major tropical cyclone. *Science, 315*(5819), 1707-1709. DOI:10.1126/science.1136466.

Jeong, D., Haus, B.K., &. Donelan, M.A. (2012). Enthalpy transfer across the air-water interface in high winds including spray. *Journal of the Atmospheric Sciences, 69*, 2733–2748. https://doi.org/10.1175/JAS-D-11-0260.1.

Jessup, A. T., Zappa, C. J., & Yeh, H. (1997). Defining and quantifying microscale wave breaking with infrared imagery. *Journal of Geophysical Research: Oceans*, *102*(C10), 23145-23153. https://doi.org/10.1029/97JC01449.

Jiang, C., Liu, X., Yao, Y. & Deng, B. (2019). Numerical investigation of solitary wave interaction with a row of vertical slotted piles on a sloping beach. *International Journal of Naval Architecture and Ocean Engineering*, *11*(1), 530-541. https://doi.org/10.1016/j.ijnaoe.2018.09.007.

Jiang, H., & Ramirez, E. M. (2013). Necessary conditions for tropical cyclone rapid intensification as derived from 11 years of TRMM data. *Journal of Climate, 26*(17), 6459-6470. https://doi.org/10.1175/JCLI-D-12-00432.1.

Kao, H-Y., & Lagerloef, G.S.E. (2020). SMAP sea surface salinity validation and the observations of the plume of hurricane Dorian. *Ocean Sciences Meeting*.

Katsaros, K. B., Vachon, P. W., Liu, W. T., & Black, P. G. (2002). Microwave remote sensing of tropical cyclones from space. *Journal of Oceanography, 58*(1), 137-151. https://doi.org/10.1023/A:1015884903180.

Kaplan, J., DeMaria, M., & J. A. Knaff, J. A. (2010). A revised tropical cyclone rapid intensification index for the Atlantic and Eastern North Pacific basins. *Weather Forecast, 25*, 220–241. https://doi.org/10.1175/2009WAF2222280.1.

Kepert, J. D. (1996). Comments on ‘‘The temperature of evaporating sea spray droplets.’’ *Journal of the Atmospheric Sciences*, *53*, 1634–1641. https://www.researchgate.net/profile/Jeffrey-Kepert/publication/249608498_Comments_on_The_Temperature_of_Evaporating_Sea_Spray_Droplets/links/55ed1b0e08aeb6516268d04d/Comments-on-The-Temperature-of-Evaporating-Sea-Spray-Droplets.pdf.

Kepert, J., Fairall, C., & Bao, J. W. (1999). Modelling the interaction between the atmospheric boundary layer and evaporating sea spray droplets. In G.L. Geernaert (Eds.) *Air-Sea Exchange: Physics, Chemistry and Dynamics* (Vol. 20, pp. 363-409). Springer. https://doi.org/10.1007/978-94-015-9291-8_14. https://doi.org/10.1007/978-94-015-9291-8_14.

Kitaigorodskii, S.A., Kuznetsov, O.A., & Panin, G.N. (1973). Coefficients of drag, sensible heat, and evaporation in the atmosphere over the surface of the sea. *Izvestiya Academy of Sciences USSR, Atmospheric and Oceanic Physics*, *9*, 644-647.

Koga, M. (1981). Direct production of droplets from breaking wind-waves—its observation by a multi-colored overlapping exposure technique. *Tellus, 33*, 552–563. https://doi.org/10.1111/j.2153-3490.1981.tb01781.x.

Komori, S. *et al.* (2018). Laboratory measurements of heat transfer and drag coefficients at extremely high wind speeds. *Journal of Physical Oceanography, 48*, 959–974. https://doi.org/10.1175/JPO-D-17-0243.1.

Kossin, J.S., Olander, T. L., & Knapp, K. R. (2013). Trend analysis with a new global record of tropical cyclone intensity. *Journal of Climate, 26*, 9960-9976. https://doi.org/10.1175/JCLI-D-13-00262.1.

Kourafalou, V. H., Androulidakis, Y. S., Halliwell Jr, G. R., Kang, H., Mehari, M. M., Le Hénaff, M., & Lumpkin, R. (2016). North Atlantic Ocean OSSE system development: Nature Run evaluation and application to hurricane interaction with the Gulf Stream. *Progress in Oceanography, 148*, 1-25. https://doi.org/10.1016/j.pocean.2016.09.001.

Krall, K. E. & Jähne, B. (2014). First laboratory study of air–sea gas exchange at hurricane wind speeds, *Ocean Science Journal, 10*, 257–265. https://doi.org/10.5194/os-10-257-2014.

Krall, K. E., Smith, A. W., Takagaki, N., & Jähne, B. (2019). Air–sea gas exchange at wind speeds up to 85 m s− 1. *Ocean Science Journal, 15*(6), 1783-1799. https://doi.org/10.5194/os-15-1783-2019.

Kudryavtsev, V. N. (2006). On the effect of sea drops on the atmospheric boundary layer. *Journal of Geophysical Research: Oceans*, *111*(C7). https://doi.org/10.1029/2005JC002970.

Kurata, N., Vella, K., Hamilton, B., Shivji, M., Soloviev, A., Silvia, M., Tartar, A., & Perrie, W. (2016). Surfactant-associated bacteria in the near-surface layer of the ocean. *Scientific Reports, 6*, 19123. https://doi.org/10.1038/srep19123.

Larcombe, P., & Carter, R. M. (2004). Cyclone pumping, sediment partitioning and the development of the Great Barrier Reef shelf system: a review. *Quaternary Science Reviews*, *23*(1-2), 107-135. https://doi.org/10.1016/j.quascirev.2003.10.003.

Law, C. S., Smith, M. J., Harvey, M. J., Bell, T. G., Cravigan, L. T., Elliott, F. C., & Walker, C. F. (2017). Overview and preliminary results of the Surface Ocean Aerosol Production (SOAP) campaign. *Atmospheric Chemistry and Physics*, *17*(22), 13645-13667. https://doi.org/10.5194/acp-17-13645-2017.

Lee, W., Kim, S. H., Chu, P. S., Moon, I. J., & Soloviev, A. V. (2019). An index to better estimate tropical cyclone intensity change in the Western North Pacific. *Geophysical Research Letters, 46*(15), 8960-8968. https://doi.org/10.1029/2019GL083273.

Leifer, I., & De Leeuw, G. (2002). Bubble measurements in breaking-wave generated bubble plumes during the LUMINY wind-wave experiment. *Washington DC American Geophysical Union Geophysical Monograph Series*, *127*, 303-309. DOI:10.1029/GM127p0303.

Lighthill, J., G. Holland, W. Gray, C. Landsea, G. Craig, J. Evans, Y. Kurihara, & Guard, C. (1994). Global climate change and tropical cyclones. *Bulletin of the American Meteorological Society*, *75*, 2147–2157. https://www.jstor.org/stable/26231689.

Lin, I. I., Black, P., Price, J. F., Yang, C. Y., Chen, S. S., Lien, C. C., & D'Asaro, E. A. (2013). An ocean coupling potential intensity index for tropical cyclones. *Geophysical Research Letters*, *40*(9), 1878-1882. https://doi.org/10.1002/grl.50091.

Liu, L. L., Wang, W., & Huang, R. X. (2008). The mechanical energy input to the ocean induced by tropical cyclones. *Journal of Physical Oceanography*, *38*(6), 1253-1266. https://doi.org/10.1175/2007JPO3786.1.

Liu, S. S., Sun, L., Wu, Q., & Yang, Y. J. (2017). The responses of cyclonic and anticyclonic eddies to typhoon forcing: The vertical temperature-salinity structure changes associated with the horizontal convergence/divergence. *Journal of Geophysical Research: Oceans*, *122*(6), 4974-4989. https://doi.org/10.1002/2017JC012814.

Liu, X., & Wei, J. (2015). Understanding surface and subsurface temperature changes induced by tropical cyclones in the Kuroshio. *Ocean Dynamics*, *65*, 1017-1027. https://doi.org/10.1007/s10236-015-0851-9.

Lu, J., Lim. H., Liew, S.C., Bao, M., & Kwoh, L.K. (1999). Statistics in Southeast Asian waters compiled from ERS synthetic aperture radar imagery. *Earth Observation Quarterly*, *621*, 13–17. https://scholarbank.nus.edu.sg/handle/10635/112838.

Lu, J., Kwoh, L.K., Lim, H., Liew, S.C., & Bao, M. (2000). Mapping oil pollution from space. *Backscatter*, *11*, 23–26.

Lukas, R., & Lindstrom, E. (1991). The mixed layer of the western equatorial Pacific Ocean. *Journal of Geophysical Research: Oceans*, *96*(S01), 3343-3357. https://doi.org/10.1029/90JC01951.

Ma, H., A. V. Babanin, and F. Qiao (2020). Field observations of sea spray under tropical cyclone Olwyn. *Ocean Dynamics*, *70*, 1439– 1448. https://doi.org/10.1007/s10236-020-01408-x.

Maccherone, B. (2018). *MODIS*. National Aeronautics and Space Administration. https://modis.gsfc.nasa.gov/about/.

Maiß, M. (1986). *Modelluntersuchung zum Einfluss von Blasen auf den gasaustausch zwischen atmosphäre und meer* [Doctoral dissertation, Heidelberg Univerity]. Zenodo. https://doi.org/10.5281/zenodo.15415.

Malkus, J. S., & Riehl, H. (1960). On the dynamics and energy transformations in steady-state hurricanes. *Tellus*, *12*(1), 1-20. https://doi.org/10.1111/j.2153-3490.1960.tb01279.x.

Marks, F.D. (2003). Hurricanes. In J. Holton, J. Pyle, & J. Curry (Eds.) *Encyclopedia of Atmospheric Sciences*, (pp. 942-966). Elsevier Science Ltd.

Mårtensson, E. M., Nilsson, E. D., de Leeuw, G., Cohen, L. H., & Hansson, H. C. (2003). Laboratory simulations and parameterization of the primary marine aerosol production. *Journal of Geophysical Research: Atmospheres*, *108*, 4297. https://doi.org/10.1029/2002JD002263.

Masters, J. (2020). *The most reliable hurricane models, according to their 2019 performance.* Yale Climate Connections, Yale University. https://yaleclimateconnections.org/2020/08/the-most-reliable-hurricane-models-according-to-their-2019-performance/.

May, N. W., Axson, J. L., Watson, A., Pratt, K. A., & Ault, A. P. (2016). Lake spray aerosol generation: a method for producing representative particles from freshwater wave breaking. *Atmospheric Measurement Techniques*, *9*(9), 4311-4325. https://doi.org/10.5194/amt-9-4311-2016.

McNeil, C. & D'Asaro, E. (2007). Parameterization of air sea gas fluxes at extreme wind speeds, *Journal of Marine Systems*, *66*, 110–121. https://doi.org/10.1016/j.jmarsys.2006.05.013.

Mehta, S., Ortiz-Suslow, D. G., Smith, A. W., & Haus, B. K. (2019). A laboratory investigation of spume generation in high winds for fresh and seawater. *Journal of Geophysical Research: Atmospheres*, *124*(21), 11297-11312. https://doi.org/10.1029/2019JD030928.

Merrill, R. T. (1988). Environmental influences on hurricane intensification. *Journal of the Atmospheric Sciences*, *45*, 1678–1687. https://doi.org/10.1175/1520-0469(1988)045<1678:EIOHI>2.0.CO;2.

Migliaccio, M., Nunziata, F., & Gambardella, A. (2009). On the copolarised phase difference for oil spill observation. *International Journal of Remote Sensing*, *30*(6), 1587-1602. https://doi.org/10.1080/01431160802520741.

Miles, J. W. (1959). On the generation of surface waves by shear flows. Part 3. Kelvin-Helmholtz instability. *Journal of Fluid Mechanics*, *6*, 583– 598. doi:10.1017/S0022112059000842.

Miller, B. I. (1958). On the maximum intensity of hurricanes. *Journal of Meteorology*, *15*, 184-195. https://doi.org/10.1175/1520-0469(1958)015<0184:OTMIOH>2.0.CO;2.

Mischler, W. (2014). *Systematic measurements of bubble induced gas exchange for trace gases with low solubilities* [Doctoral Dissertation, Heidelberg University]. Heidelberg University Library. DOI:10.11588/heidok.00017720.

Monahan, E. C. (1969). Fresh water whitecaps. *Journal of the Atmospheric Sciences*, *26*(5), 1026–1029. https://doi.org/10.1175/1520-0469(1969)026<1026:FWW>2.0.CO;2.

Monahan, E.C., Fairall, C.W., Davidson, K.L., & Boyle, P.J. (1983). Observed inter-relations between 10 m winds, ocean whitecaps and marine aerosols. *Quarterly Journal of the Royal Meteorological Society*, *109*, 379-392. https://doi.org/10.1002/qj.49710946010.

Monahan, E. C., & Zietlow, C. R. (1969). Laboratory comparisons of fresh-water and salt-water whitecaps. *Journal of Geophysical Research*, *74*, 6961–6966. https://doi.org/10.1029/JC074i028p06961.

Moon, I. J., Ginis, I., Hara, T., & Thomas, B. (2007). A physics-based parameterization of air–sea momentum flux at high wind speeds and its impact on hurricane intensity predictions. *Monthly Weather Review*, *135*(8), 2869-2878. https://doi.org/10.1175/MWR3432.1.

Mueller, J. A., & Veron, F. (2009). A sea state-dependent spume generation function. *Journal of Physical Oceanography*, *39*, 2363–2372. https://doi.org/10.1175/2009JPO4113.1.

Mueller, J. A., & Veron, F. (2014). Impact of sea spray on air–sea fluxes. Part II: Feedback effects. *Journal of Physical Oceanography*, *44*, 2835–2853. https://doi.org/10.1175/JPO-D-13-0246.1.

Murphy, D. M., Anderson, J. R., Quinn, P. K., McInnes, L. M., Brechtel, F. J., Kreidenweis, S. M., & Buseck, P. R. (1998). Influence of sea-salt on aerosol radiative properties in the Southern Ocean marine boundary layer. *Nature*, *392*(6671), 62-65. https://doi.org/10.1038/32138.

Oey, L. Y., Ezer, T., Wang, D. P., Fan, S. J., & Yin, X. Q. (2006). Loop current warming by Hurricane Wilma. *Geophysical Research Letters*, *33*(8). https://doi.org/10.1029/2006GL025873.

Ooyama, K. (1969). Numerical simulation of the life cycle of tropical cyclones. *Journal of the Atmospheric Sciences*, *26*(1), 3-40. https://doi.org/10.1175/1520-0469(1969)026<0003:NSOTLC>2.0.CO;2.

Ortiz-Suslow, D. G., Haus, B. K., Mehta, S., & Laxague, N. J. (2016). Sea spray generation in very high winds. *Journal of the Atmospheric Sciences*, *73*(10), 3975-3995. https://doi.org/10.1175/JAS-D-15-0249.1.

Ovadnevaite, J., Manders, A., De Leeuw, G., Ceburnis, D., Monahan, C., Partanen, A. I., & O'Dowd, C. D. (2014). A sea spray aerosol flux parameterization encapsulating wave state. *Atmospheric Chemistry and Physics*, *14*(4), 1837-1852. https://doi.org/10.5194/acp-14-1837-2014.

Park, J., Jang, J., Yoon, Y. J., Kang, S., Kang, H., Park, K., & Lee, B. Y. (2022). When river water meets seawater: Insights into primary marine aerosol production. *Science of the Total Environment*, *807*, 150866. https://doi.org/10.1016/j.scitotenv.2021.150866.

Park, J. J., Kim, K., & Schmitt, R. W. (2009). Global distribution of the decay timescale of mixed layer inertial motions observed by satellite-tracked drifters. *Journal of Geophysical Research: Oceans*, *114*(C11). https://doi.org/10.1029/2008JC005216.

Patro, R., Leifer, I., & Bowyer, P. (2002). Better bubble process modeling: Improved bubble hydrodynamics parameterization. In M.A. Donelan, W.M. Drennan, E.S. Saltzman, & R. Wanninkhof (Eds.) *Gas Transfer at Water Surfaces* (Vol. 127, pp. 315-320) American Geophysical Union Geophysical Monograph Series. 10.1029/GM127p0315. DOI:10.1029/GM127p0315.

Perrie, W., Andreas, E. L., Zhang, W., Li, W., Gyakum, J., & McTaggart-Cowan, R. (2005). Sea spray impacts on intensifying midlatitude cyclones. *Journal of the Atmospheric Sciences*, *62*, 1867–1883. https://doi.org/10.1175/JAS3436.1.

Peng, T., & Richter, D. (2019). Sea spray and its feedback effects: Assessing bulk algorithms of air–sea heat fluxes via direct numerical simulations. *Journal of Physical Oceanography*, *49*(6), 1403-1421. https://doi.org/10.1175/JPO-D-18-0193.1.

Pöschl, U., & Shiraiwa, M. (2015). Multiphase chemistry at the atmosphere–biosphere interface influencing climate and public health in the anthropocene. *Chemical Reviews*, *115*(10), 4440-4475. https://doi.org/10.1021/cr500487s.

Powell, M. D., Vickery, P. J., & Reinhold, T. A. (2003). Reduced drag coefficient for high wind speeds in tropical cyclones. *Nature*, *422*(6929), 279-283. https://doi.org/10.1038/nature01481.

Price, J. F. (1981). Upper ocean response to a hurricane, *Journal of Physical Oceanography*, *11*, 153–175. https://doi.org/10.1175/1520-0485(1981)011<0153:UORTAH>2.0.CO;2.

Pruppacher, H., & Klett, J. (1978). *Microphysics of clouds and precipitation*. D. Reidel Publishing Company. https://doi.org/10.1007/978-94-009-9905-3.

Pruppacher, H.R. & Klett, J.D. (2010). *Microphysics of Clouds and Precipitation* (2nd ed.). Springer: Dordrecht. https://doi.org/10.1007/978-0-306-48100-0.

Qasem, N. A., Generous, M. M., Qureshi, B. A., & Zubair, S. M. (2021). A comprehensive review of saline water correlations and data: Part II—thermophysical properties. *Arabian*

Journal for Science and Engineering, *46*, 1941-1979. https://doi.org/10.1007/s13369-020-05020-5.

Rappaport, E. N., Franklin, J. L., Avila, L. A., Baig, S. R., Beven, J. L., Blake, E. S., & Landsea, C. W. (2009). Advances and challenges at the National Hurricane Center. *Weather and Forecasting*, *24*(2), 395-419. https://doi.org/10.1175/2008WAF2222128.1.

Richter, D. H., & Stern, D.P. (2014). Evidence of spray-mediated air-sea enthalpy flux within tropical cyclones. *Geophysical Research Letters*, *41*, 2997–3003. https://doi.org/10.1002/2014GL059746.

Richter, D., & Sullivan, P. (2014) The sea spray contribution to sensible heat flux, *Journal of the Atmospheric Sciences*, *71*, 640–654. https://doi.org/10.1175/JAS-D-13-0204.1.

Richter, D. H., Wainwright, C., Stern, D. P., Bryan, G. H., & Chavas, D. (2021). Potential low bias in high-wind drag coefficient inferred from dropsonde data in hurricanes. *Journal of the Atmospheric Sciences*, *78*(7), 2339-2352. https://doi.org/10.1175/JAS-D-20-0390.1.

Riehl, H. (1954). *Tropical meteorology*. McGraw-Hill.

Sanabia, E. R., & Jayne, S. R. (2020). Ocean observations under two major hurricanes: Evolution of the response across the storm wakes. *AGU Advances, 1*(3), e2019AV000161. https://doi.org/10.1029/2019AV000161.

Schade, L. R., & Emanuel, K. A. (1999). The ocean's effect on the intensity of tropical cyclones: Results from a simple coupled atmosphere–ocean model. *Journal of the Atmospheric Sciences*, *56*(4), 642-651. https://doi.org/10.1175/1520-0469(1999)056<0642:TOSEOT>2.0.CO;2.

Scott, J. C. (1975). The role of salt in whitecap persistence. *Deep Sea Research and Oceanographic Abstracts*, *22*(10), 653–657. https://doi.org/10.1016/0011-7471(75)90002-9.

Scott, R. W. and Huff, F. A. (1996). Impacts of the great lakes on regional climate conditions. *Journal of Great Lakes Research*, *22*, 845–863. https://doi.org/10.1016/S0380-1330(96)71006-7.

Shapiro, L. J., & Willoughby, H (1982). The response of balanced hurricanes to local sources of heat and momentum. *Journal of the Atmospheric Sciences*, *39*, 378–394. https://doi.org/10.1175/1520-0469(1982)039<0378:TROBHT>2.0.CO;2.

Shay, L. K., Goni, G. J., & Black, P. G. (2000). Effects of a warm oceanic feature on Hurricane Opal. *Monthly Weather Review, 128*(5), 1366-1383. https://doi.org/10.1175/1520-0493(2000)128<1366:EOAWOF>2.0.CO;2.

Shay, L. K., & Brewster, J. K. (2010). Oceanic heat content variability in the eastern Pacific Ocean for hurricane intensity forecasting. *Monthly Weather Review*, *138*(6), 2110-2131. https://doi.org/10.1175/2010MWR3189.1.

Shpund, J., Pinsky, M., & Khain, A. (2011). Microphysical structure of the marine boundary layer under strong wind and spray formation as seen from simulations using a 2D explicit microphysical model. Part II: The role of sea spray. *Journal of the Atmospheric Sciences*, *69*, 3501-3514. https://doi.org/10.1175/2011JAS3652.1.

Shpund, J., Khain, A., & Rosenfeld, D. (2019). Effects of sea spray on the dynamics and microphysics of an idealized tropical cyclone. *Journal of the Atmospheric Sciences*, *76*(8), 2213-2234. https://doi.org/10.1175/JAS-D-18-0270.1.

Shpund, J., Zhang, J. A., Pinsky, M., & Khain, A. (2012). Microphysical structure of the marine boundary layer under strong wind and spray formation as seen from simulations using a 2D explicit microphysical model. Part II: The role of sea spray. *Journal of the Atmospheric Sciences*, *69*(12), 3501-3514. https://doi.org/10.1175/JAS-D-11-0281.1.

Siddiqui, M. K., & Loewen, M. R. (2007). Characteristics of the wind drift layer and microscale breaking waves. *Journal of Fluid Mechanics*, *573*, 417-456. doi:10.1017/S0022112006003892.

Siddiqui, M. K., Loewen, M. R., Richardson, C., Asher, W. E., & Jessup, A. T. (2001). Simultaneous particle image velocimetry and infrared imagery of microscale breaking waves. *Physics of Fluids*, *13*(7), 1891-1903. https://doi.org/10.1063/1.1375144.

Simpson, R. H. (1974). The Hurricane Disaster Potential Scale. *Weatherwise*, *27*(169) 169-186. https://doi.org/10.1080/00431672.1974.9931702.

Sitkowski, M., & G. M. Barnes (2009). Low-level thermodynamic, kinematic and reflectivity fields of Hurricane Guillermo (1997) during rapid intensification. *Monthly Weather Review*, *137*, 645–663. https://doi.org/10.1175/2008MWR2531.1.

Slade, J. H., VanReken, T. M., Mwaniki, G. R., Bertman, S., Stirm, B., and Shepson, P. B. (2010). Aerosol production from the surface of the Great Lakes, *Geophysical Research Letters*, *37*, L18807. https://doi.org/10.1029/2010GL043852.

Smith, R. K. (1981). The cyclostrophic adjustment of vortices with application to tropical cyclone modification. *Journal of the Atmospheric Sciences*, *38*, 2020–2030. https://doi.org/10.1175/1520-0469(1981)038<2021:TCAOVW>2.0.CO;2.

Smith, R. K., & Montgomery, M. T. (2011). Observations of the convective environment in developing and non-developing tropical disturbances. *Quarterly Journal of the Royal Meteorological Society*, *137*, 1-20. DOI:10.1002/qj.000.

Smith, R. K., & Montgomery, M. T. (2016). Understanding hurricanes. *Weather, 71*(9), 219-223. https://met.nps.edu/~mtmontgo/papers/Pub_146.pdf.

Soloviev, A. V., Lukas, R., Donelan, M. A., Haus, B. K., & Ginis, I. (2017). Is the state of the air-sea interface a factor in rapid intensification and rapid decline of tropical cyclones? *Journal of Geophysical Research: Oceans, 122*(12), 10174-10183. https://doi.org/10.1002/2017JC013435.

Soloviev, A. V. & Lukas R. (2010). Effects of bubbles and sea spray on air–sea exchange in hurricane conditions. *Boundary-Layer Meteorology, 136*, 365-376. https://doi.org/10.1007/s10546-010-9505-0.

Soloviev, A., & Lukas, R. (2014). *The near-surface layer of the ocean: Structure, dynamics, and applications* (Vol. 48). Springer Science & Business Media. https://doi.org/10.1007/978-94-007-7621-0.

Soloviev, A.V., Vanderplow, B., Haus, B.K., Lukas, R., & Ginis, I. (2020). Sea spray and tropical cyclone intensity and intensification: Modeling and laboratory experiment. *JpGU - AGU Joint Meeting*.

Soloviev, A. V., Lukas, R., Donelan, M. A., Haus, Brian K., & Ginis, I. (2014). The air-sea interface and surface stress under tropical cyclones. *Scientific Reports, 4*, 5306. https://doi.org/10.1038/srep05306.

Soloviev, A., Matt, S., Gilman, M., Hühnerfuss, H., Haus, B., Jeong, D., Savelyev, I., & Donelan, M. (2011). Modification of turbulence at the air-sea interface due to the presence of surfactants and implications for gas exchange. Part I: laboratory experiment. In *Gas transfer at water surfaces* (pp. 285-296). Kyoto University Press. https://nsuworks.nova.edu/occ_facbooks/57/.

Spiel, D.E. (1997). More on the births of jet drops from bubbles bursting on seawater surfaces. *Journal of Geophysical Research, 102*(C3), 5815-5821. https://doi.org/10.1029/96JC03582

Spiel, D.E. (1998). On the birth of film drops from bubbles bursting on seawater surfaces. *Journal of Geophysical Research, 103*(C11), 24907-24918. https://doi.org/10.1029/98JC02233.

Sroka, S., & Emanuel, K. (2021). A review of parameterizations for enthalpy and momentum fluxes from sea spray in tropical cyclones. *Journal of Physical Oceanography*, *51*(10), 3053-3069. https://doi.org/10.1175/JPO-D-21-0023.1.

Staniec, A., Vlahos, P. & Monahan, E.C. (2021). The role of sea spray in atmosphere–ocean gas exchange. *Nature Geoscience*, *14*, 593–598. https://doi.org/10.1038/s41561-021-00796-z.

Stewart, R. (2002). *Introduction to physical oceanography*. Texas A&M University. https://hdl.handle.net/1969.1/160216.

Takagaki, N., Komori, S., Suzuki, N., Iwano, K., Kuramoto, T., Shimada, S., & Takahashi, K. (2012). Strong correlation between the drag coefficient and the shape of the wind sea spectrum over a broad range of wind speeds. *Geophysical Research Letters, 39*(23). https://doi.org/10.1029/2012GL053988.

Thorpe, S.A. (1986). Bubble clouds: A review of their detection by sonar, of realistic models, and of how may be determined. In E.C. Monahan & G. MacNiocaill (Eds.) *Whitecaps and Their Role in Air-Sea Exchange Processes* (pp. 57-68). D. Reidel Publishing Company. https://doi.org/10.1007/978-94-009-4668-2_6.

Todd, R. E., Asher, T. G., Heiderich, J., Bane, J. M., & Luettich, R. A. (2018). Transient response of the Gulf Stream to multiple hurricanes in 2017. *Geophysical Research Letters*, *45*(19), 10-509. https://doi.org/10.1029/2018GL079180.

Toffoli, A., Babanin, A., Donelan, M. Haus, B.K. & Jeong, D. (2011). Estimating sea spray volume with a laser altimeter. *Journal of Atmospheric and Oceanic Technology, 28*, 1177–1183. https://doi.org/10.1175/2011JTECHO827.1

Tory, K. J., Montgomery, M. T., & Davidson, N. E. (2006). Prediction and diagnosis of tropical cyclone formation in an NWP system. Part I: The critical role of vortex enhancement in deep convection. *Journal of the Atmospheric Sciences*, *63*(12), 3077-3090. https://doi.org/10.1175/JAS3764.1

Troitskaya, Y., Kandaurov, A., Ermakova, O., Kozlov, D., Sergeev, D., & Zilitinkevich, S. (2017). Bag-breakup fragmentation as the dominant mechanism of sea-spray production in high winds. *Scientific Reports*, *7*, 1614. https://doi.org/10.1038/s41598-017-01673-9.

Troitskaya, Y., Kandaurov, A., Ermakova, O., Kozlov, D., Sergeev, D., & Zilitinkevich, S. (2018a). The “bag breakup” spume droplet generation mechanism at high winds. Part I: Spray generation function. *Journal of Physical Oceanography*, *48*(9), 2167-2188. https://doi.org/10.1175/JPO-D-17-0104.1.

Troitskaya, Y., Druzhinin, O., Kozlov, D., & Zilitinkevich, S. (2018b). The “bag breakup” spume droplet generation mechanism at high winds. Part II: Contribution to momentum and enthalpy transfer. *Journal of Physical Oceanography*, *48*(9), 2189-2207. https://doi.org/10.1175/JPO-D-17-0105.1.

Troitskaya, Y., Sergeev, D., Kandaurov, A., Vdovin, M., & Zilitinkevich, S. (2019). The effect of foam on waves and the aerodynamic roughness of the water surface at high winds. *Journal of Physical Oceanography, 49*(4), 959-981. https://doi.org/10.1175/JPO-D-18-0168.1

Troitskaya, Y., Sergeev, D., Vdovin, M., Kandaurov, A., Ermakova, O., & Takagaki, N. (2020). A laboratory study of the effect of surface waves on heat and momentum transfer at high wind speeds. *Journal of Geophysical Research: Oceans, 125*(7), e2020JC016276. https://doi.org/10.1029/2020JC016276.

Tyree, C. A., Hellion, V. M., Alexandrova, O. A., & Allen, J. O. (2007). Foam droplets generated from natural and artificial seawaters. *Journal of Geophysical Research: Atmospheres, 112*. https://doi.org/10.1029/2006JD007729.

Uang, C.L. (1999). Impacts of sea spray and oceanic response on the development of tropical cyclones. Preprints, *23rd conference on hurricanes and tropical meteorology*. American Meteorological Society, 30–31.

Uning, R., Latif, M. T., Yu, K. L., Cheng, S. Y., Ahamad, F., Khan, M. F., & Suratman, S. (2018). Surfactants in the sea surface microlayer, underlying water, and atmospheric particles of tropical coastal ecosystems. *Water, Air, & Soil Pollution*, *229*, 1-11. https://doi.org/10.1007/s11270-018-3961-4.

Vaida, V. (2016). Atmospheric radical chemistry revisited. *Science*, *353*(6300), 650-650. DOI:10.1126/science.aah4111.

Vanderplow, B. (2020). *Effects of Surfactants on the Generation of Sea Spray During Tropical Cyclones.* [Masters thesis, Nova Southeastern University]. NSU Works. https://nsuworks.nova.edu/hcas_etd_all/12.

Vanderplow, B., Soloviev, A. V., Dean, C. W., Haus, B. K., Lukas, R., Sami, M., & Ginis, I. (2020). Potential effect of bio-surfactants on sea spray generation in tropical cyclone conditions. *Scientific Reports*, *10*(1), 1-10. https://doi.org/10.1038/s41598-020-76226-8.

Velotto, D., Nunziata, F., Migliaccio, M., & Lehner, S. (2013). Dual-polarimetric TerraSAR-X SAR data for target at sea observation. *IEEE Transactions on Geoscience and Remote Sensing*, *10*(5), 1114-1118. DOI:10.1109/LGRS.2012.2231048

Veron, F. (2015). Ocean spray. *Annual Review of Fluid Mechanics*, *47*, 507–538. https://doi.org/10.1146/annurev-fluid-010814-014651.

Veron, F., Hopkins, C., Harrison, E. L., & Mueller, J. A. (2012). Sea spray spume droplet production in high wind speeds. *Geophysical Research Letters*, *39*, L16602. https://doi.org/10.1029/2012GL052603.

Wada, A., Kanada, S., & H. Yamada, H. (2018). Effect of air-sea environmental conditions and interfacial processes on extremely intense Typhoon Haiyan (2013). *Journal of Geophysical Research: Atmospheres*, *123*(10), 379–10 405. https://doi.org/10.1029/2017JD028139.

Wahl, T., Skøelv, Å., Pedersen, J. P., Seljelv, L. G., Andersen, J. H., Follum, O. A., & Hamnes, H. (1996). Radar satellites: A new tool for pollution monitoring in coastal waters. *Coastal Management, 24*(1), 61-71. DOI:10.1080/08920759609362281.

Walker, N. D., Leben, R. R., & Balasubramanian, S. (2005). Hurricane-forced upwelling and chlorophyll a enhancement within cold-core cyclones in the Gulf of Mexico. *Geophysical Research Letters, 32*, L18610. https://doi.org/10.1029/2005GL023716.

Wang, X., Deane, G. B., Moore, K. A., Ryder, O. S., Stokes, M. D., Beall, C. M., Collins, D.B., Santander, M.V., Burrows, S.M. & Prather, K. A. (2017). The role of jet and film drops in controlling the mixing state of submicron sea spray aerosol particles. *Proceedings of the National Academy of Sciences*, *114*(27), 6978-6983. https://doi.org/10.1073/pnas.1702420114.

Wang, Y., Kepert, J. D., & Holland, G. J. (1999). The impact of sea spray evaporation on tropical cyclone intensification. *23rd conference on hurricanes and tropical meteorology*. American Meteorological Society, 26–29.

Wanninkhof, R., Asher, W. E., Ho, D. T., Sweeney, C., & McGillis, W. R. (2009). Advances in quantifying air-sea gas exchange and environmental forcing. *Annual Review of Marine Science, 1*, 213-244. DOI:10.1146/annurev.marine.010908.163742.

Webb, P. (2021). *Introduction to oceanography*. Roger Williams University. https://rwu.pressbooks.pub/webboceanography/.

Woodcock, A. H. (1978). Marine fog droplets and salt nuclei—Part I. *Journal of Atmospheric Sciences, 35*(4), 657-664. DOI:10.1175/1520-0469(1978)035<0657:MFDASN>2.0.CO;2

Wu, C. R., Chang, Y. L., Oey, L. Y., Chang, C. W. J., & Hsin, Y. C. (2008). Air-sea interaction between tropical cyclone Nari and Kuroshio. *Geophysical Research Letters, 35*(12). DOI:10.1029/2008GL033942.

Wu, J. (1973). Spray in the atmospheric surface layer: Laboratory study. *Journal of Geophysical Research, 78*, 511–519. https://doi.org/10.1029/JC078i003p00511.

Wu, J. (1981). Evidence of sea spray produced by bursting bubbles. *Science, 212*, 324–326. DOI:10.1126/science.212.4492.324.

Wurl, O., Wurl, E., Miller, L., Johnson, K., & Vagle, S. (2011). Formation and global distribution of sea surface microlayers. *Biogeosciences, 8*(1), 121-135. https://doi.org/10.5194/bg-8-121-2011.

Yau, M. K., Liu, Y., Zhang, D. L., & Chen, Y. (2004). A multiscale numerical study of Hurricane Andrew (1992). Part VI: Small-scale inner-core structures and wind streaks. *Monthly Weather Review, 132*(6), 1410-1433. DOI:10.1175/1520-0493(2004)132<1410:AMNSOH>2.0.CO;2.

Zábori, J., Matisāns, M., Krejci, R., Nilsson, E. D., & Ström, J. (2012). Artificial primary marine aerosol production: A laboratory study with varying water temperature, salinity, and succinic acid concentration. *Atmospheric Chemistry and Physics, 12*, 10709–10724. https://doi.org/10.5194/acp-12-10709-2012.

Zhang, J. A., Black, P. G., French, J. R., & Drennan, W. M. (2008). First direct measurements of enthalpy flux in the hurricane boundary layer: The CBLAST results. *Geophysical Research Letter*s, *35*, L14813. doi:10.1029/2008GL034374.

Zhang, B., & Perrie, W. (2012). Cross-polarized synthetic aperture radar: A new potential measurement technique for hurricanes. *Bulletin of the American Meteorological Society, 93*(4), 531-541. https://doi.org/10.1175/BAMS-D-11-00001.1.

Zhang, H., He, H., Zhang, W. Z., & Tian, D. (2021). Upper ocean response to tropical cyclones: A review. *Geoscience Letters, 8*, 1-12. https://doi.org/10.1186/s40562-020-00170-8.

Zhao, D., Toba, Y., Sugioka, K. I., & Komori, S. (2006). New sea spray generation function for spume droplets. *Journal of Geophysical Research, Oceans, 111*(C2). DOI:10.1029/2005JC002960.

Zinke, J., Nilsson, E. D., Zieger, P., & Salter, M. E. (2022). The effect of seawater salinity and seawater temperature on sea salt aerosol production. *Journal of Geophysical Research, Atmospheres, 127*(16), e2021JD036005. https://doi.org/10.1029/2021JD036005.